QUANTIFYING THE EFFECT OF STRESSORS ON CARBON DIOXIDE UPTAKE BY VEGETATION COMMUNITIES IN THE BRUCE PENINSULA

LORD-EMMANUEL ACHIDAGO

A THESIS SUBMITTED TO THE FACULTY OF GRADUATE STUDIES

IN PARTIAL FULFILLMENT OF REQUIREMENTS FOR THE DEGREE OF MASTER OF SCIENCE

GRADUATE PROGRAM IN GEOGRAPHY

FACULTY OF ENVIRONMENTAL AND URBAN CHANGE

YORK UNIVERSITY

TORONTO, ONTARIO, CANADA

NOVEMBER 2023

Abstract

Climate change, with its resulting warming effect on Earth, is changing terrestrial ecosystems and their ability to regulate the ever-increasing atmospheric concentration of CO_2. The ability to forecast the response of ecosystems to climate change remains a crucial research area. It is projected that many terrestrial ecosystems will be unable to compensate for current anthropogenic emissions of CO_2 (Berger et al., 2001). Little is known about how the vegetation in the Bruce Peninsula will respond to climate change and how effective each plant community is in fixing atmospheric CO_2. The Bruce Peninsula is a United Nations Educational, Scientific and Cultural Organization (UNESCO) world biosphere reserve with some of the oldest Eastern white cedar (*Thuja occidentalis*) trees, up to 935 years old, in Eastern North America (Kelly et al., 1994). It is also an area where Eastern White Cedar dominates vast tracts of forest and therefore is an important location to take a snapshot of the general situation of temperate vegetation ecosystems. I examine how climate change and land-use change could affect CO_2 uptake by measuring trends in climate and vegetation growth and how CO_2 uptake has been affected by environmental stressors over the past 20 years. By quantifying the mean photosynthesis of coniferous and deciduous forests and cropland over that period of time, I estimate the relative capacity of the different vegetative cover types to sequester CO_2. To accomplish this, I obtained twenty years of Gross Primary Productivity (GPP) data from the Moderate Imaging Spectroradiometer (MODIS) and the Global Orbiting Carbon Observatory-2 (OCO-2) Sunlight Induced Fluorescence (GOSIF) datasets from which I selected nine target study sites exhibiting the highest proportions by cover of coniferous and deciduous forests and cropland in the Bruce Peninsula. I compare this information seasonally with the area's climate data from the ERA-5 climate model to evaluate GPP responses from both models to climate drivers. The results reveal that there were no significant trends in GPP from either model. In general, MODIS GPP was more responsive to environmental stressors than GOSIF GPP, particularly in the spring. On average, deciduous forests were the most productive, but coniferous forests contributed more to CO_2 uptake than Cropland and Deciduous forests.

Dedication

This work is dedicated to my late father, Bernard Achidago, for leading the family into uncharted territory, and to my mother, Elizabeth Achidago, for her tenacity and extraordinary heart.

Acknowledgments

“Give thanks to the LORD, for he is good. His love endures forever” — Ps 136:1

I want to sincerely thank Dr. Richard Lawrence Bello for believing in me and mentoring me and for all of his support and advice along the journey

Thank you, Dr. Tarmo K. Remmel, for your advice, revisions, and suggestions. I also appreciate your persistence in upholding the highest standards. The advice and ideas from Dr. Baoxin Hu were also extremely beneficial

I am grateful to Drs. Olalekan Balogun and Adeyemi Olusola, from whom I have learned so much. I also like to thank Dr. Samuel Ogunjo, Philip Lynch, and Silas Achidago for their assistance with data processing

I also want to express gratitude to my family – Elizabeth, Bertha, Lucas, Belinda, Benedicta, Silas, and Bernice – who form my support system and greatest source of encouragement

My colleagues also made the journey very much worth it! Rachael Abulu, Ria Ducusin, Kathleen Bao, Vivien Bediako, Barbara Kerr, Ami-Ali Ebrahimirad, Prateeksha Pathak Victoria Caroll and Tejumade Ojo

Thanks to Professor Mensah, Margaret Mensah, Trisha Fuller-Davidson, Patrick Mojdehi and Ouma Jaipaul-Gill for their immense support

I am grateful to all of my friends who were there to laugh with me and listen to me unload my frustrations

Finally, I would like to thank the Faculty of Environmental and Urban Change (EUC) for funding my research

Table of Contents

List of Figures

List of Tables

List of Acronyms

APAR	Absorbed Photosynthetically Active Radiation
EC	Eddy Covariance
ECMWF	European Centre for Medium-Range Weather Forecasts
EVI	Enhanced Vegetation
FPAR	Fraction of Photosynthetically Active Radiation
GOME-2	Global Ozone Monitoring Experiment-2
GOSAT	Greenhouse Gases Observing Satellite
GOSIF	Global Orbiting Carbon Observatory-2 Sunlight Induced Fluorescence
GPP	Gross Primary Productivity
LUE	Light Use Efficiency
MODIS	Moderate Image Spectroradiometer
NEE	Net Ecosystem Exchange
NDVI	Normalized Difference Vegetation Index
NPP	Net Primary Productivity
PAR	Photosynthetically Active Radiation
PPFD	Photosynthetic Photon Flux Density
SCIAMACHY	SCanning Imaging Absorption SpectroMeter for Atmospheric CHartographY
SIF	Sunlight-induced Fluorescence
UNESCO	United Nations Educational, Scientific and Cultural Organization
VI	Vegetation Index

1 Introduction

The balance between emissions and uptake of greenhouse gases by terrestrial and oceanic sinks affects their contributions to atmospheric concentrations of greenhouse gases, particularly carbon dioxide (CO_2) and methane (CH_4). On a global scale, the sources of carbon dioxide emissions surpass the capacity of carbon dioxide sinks (Berger et al., 2021). An especially problematic greenhouse gas source is the anthropogenic emission of CO_2 from the combustion of fossil fuels. The terrestrial and oceanic sinks have demonstrated their capacity to sequester about 60% of the annual CO_2 emissions generated by human activities over the course of the past six decades (IPCC, 2022). The persistent rise in atmospheric CO_2 concentrations can be primarily attributed to the combustion of fossil fuels within the natural surroundings (IPCC, 2022), leading to continuous accumulation of carbon in the atmosphere and resulting in an escalating surplus, thereby intensifying global warming and causing notable alterations in worldwide climate patterns. The Mauna Loa observatory, which has the longest direct continuous record of mean CO_2 concentrations in the atmosphere recorded over 400 ppm for the first time at the In May 2013 (Le Quéré et al., 2015). By September 2023, the value mean atmospheric concentration of CO_2 increased to 418.51 ppm (Global Monitoring Laboratory - Carbon Cycle Greenhouse Gases, n.d.)

The rate of increase in the Earth's surface temperature since 1970 has surpassed that of any other 50-year interval within the past 2,000 years. The observed increase in temperature can be attributed to greenhouse gases, primarily CO_2 and CH_4 (IPCC, 2022). According to the Intergovernmental Panel on Climate Change (IPCC, 2022), there was a 0.99°C increase in the global surface temperature from 2001 to 2020 compared to the period between 1850 and 1900. The hottest day (17.18°C) ever recorded globally was July 4, 2023, surpassing the all-time record that was set the day before, highlighting the urgency of global warming (Birkel, 2023). The severity and pattern of the changing climate are experienced differently in different parts of the world.

Canada has experienced a more rapid increase in temperature compared to the global average, particularly in its northern regions (the Arctic) where the warming has been most pronounced. Also, according to Parker (2017), the most recent three decades have been identified as the warmest recorded period within the past 1,400 years. These warming trajectories and rapid rates of change highlight a notable change in environmental conditions.

Climate change is largely caused by a rise in the atmospheric concentration of greenhouse gases (particularly CO_2); it is, therefore, important to maintain ecosystems that serve as strong carbon dioxide sinks, given that terrestrial ecosystems have been found to sequester roughly 25% of anthropogenic CO_2 emissions on a global scale (Friedlingstein et al., 2019). As much as terrestrial ecosystems are large carbon sinks, it is important to note that significant temporal and spatial variations exist in how vegetation sequesters CO_2, influenced mainly by the climatic conditions of a given region (Jian et al., 2022). Each terrestrial plant habitat, with a unique distribution of plant types, exhibits varying capacities for the absorption of CO_2 from the atmosphere. While certain vegetative cover types exhibit year-round growth, others are constrained to specific seasons. These are some of the variations in terms of seasonality and environmental conditions that affect the capacity of these plant ecosystems to absorb carbon dioxide from the atmosphere.

1.1 Research rationale

The Bruce Peninsula is renowned as a biodiversity hotspot characterized by abundant flora and fauna and a thriving ecosystem (Liipere, 2014). The biodiversity of this UNESCO biosphere reserve site is well known; however, a review of the literature up to the present returned no evidence of published information on its carbon dynamics, how the vegetation in this site will continue to respond to the changing climate, and what that means for CO_2 uptake. This research is exploratory and employs data from two different GPP models, the GOSIF (Li & Xiao, 2019) and MOD17A2HGF (Running & Zhao, 2021), to extract seasonal and annual patterns and assess sensitivities across a 20-year span within three distinct vegetation cover categories: cropland, coniferous forest, and deciduous forest. The research questions under consideration are:

i. Does GPP differ significantly among the three vegetation cover types seasonally or annually, and what are the implications of land cover changes for CO_2 uptake as a result?

ii. Are there any 20-year seasonal trends in GPP and environmental variables that could be attributed to climate change?

iii. Does GPP respond to interannual variations in the environmental variables?

iv. Are our answers to the above three questions dependent on the model employed?

1.2 Significance of research

This study holds significance due to the absence of prior research that has examined the carbon dynamics of the Bruce Peninsula. Additionally, this research employs different models to study carbon dynamics and takes a seasonal analysis approach. This research holds particular significance within the scientific community as it pertains to the exploration of the response of ecosystems to the altering environmental conditions induced by global warming as experienced in the Bruce Peninsula. Additionally, it examines the consistency between models employed to monitor vegetation growth and CO_2 uptake.

2 Theoretical background

This section introduces a theoretical framework to comprehensively understand GPP, including its measurement and estimation methodologies. It discusses the significance of GPP and its contribution to carbon dynamics within terrestrial ecosystems. This concept functions as the fundamental groundwork for understanding the subsequent portions of this thesis.

GPP is the total amount of CO_2 converted to carbohydrates (fixed) by terrestrial plants through photosynthesis. It is the largest carbon flux on Earth and drives ecosystem processes (Gebremichael & Barros, 2006; Amiro et al., 2010; Li & Xiao, 2019; Qiu et al., 2020). GPP is also the most variable component of the global terrestrial carbon cycle and can mitigate or amplify climate system perturbations (Verma et al., 2017) because it is the major driver of land carbon sequestration (Le Quéré et al., 2015). Consequently, even slight fluctuations in GPP can lead to substantial changes in the proportion of anthropogenic CO_2 present in the atmosphere (Raupach et al., 2008).

As a result, spatially and temporally accurate estimation of GPP has important implications for understanding carbon cycling, ecosystem functions, and feedback to the climate (Le Quéré et al., 2015; Schimel et al., 2015; Qiu et al., 2020). The feedback relationship (interdependence) between climate and the carbon cycle is robust owing to the essential role of CO_2 in the process of photosynthesis by plants. As plants engage in photosynthesis, atmospheric CO_2 levels decrease, thereby mitigating the impact of global warming (Hu et al., 2019), which is subject to various influencing factors, such as land cover characteristics and seasonal weather variations.

Land cover would likely have an influence on both the magnitude and seasonality of GPP, which is limited to plants as a result of their distinctive capacity to undergo photosynthesis. Therefore, the land cover types examined in this study are particularly related to vegetative cover. In their study, (Nuarsa et al., 2018) suggested that inquiries concerning the carbon cycle ought to examine the impact of land cover type on GPP because of the large variability in GPP explained by land cover type. Moreover, the authors illustrate the effectiveness of restoration and management approaches in mitigating substantial declines in GPP. For instance, despite the concurrent decrease in forest land area, as a result of management and restoration practices at one of their sites, the drop in productivity was not significant.

The principal factors that influence photosynthesis are a) photosynthetic photon flux density (PPFD), b) temperature, c) foliage water potential d) vapor pressure deficit (VPD), e) CO_2 concentration, and f) foliage nitrogen (Bonan, 2016) – Figure 1. Therefore, variations in the weather over time and with location that influence these factors will have a direct influence on photosynthesis.

On a leaf level, the response of jack pine trees (*Pinus banksiana*) is shown to the listed environmental controls (Figure 1). The amount of light can be determined with PPFD, represented by Figure 1a. Sufficient sunlight is needed to produce reduced nicotinamide adenine dinucleotide phosphate (NADPH) and Adenosine triphosphate (ATP) to initiate the photosynthesis process. As the sun rises, net photosynthesis starts rising until it hits about 800 $\mu molm^{-2}s^{-1}$ (light saturation level), where it peaks, and any extra PFFD will not improve the rate of net photosynthesis. Temperature is also very important in determining the rate of photosynthesis, as a temperature upward of -5 °C is required for biochemical reactions to occur. Figure 1b shows how the net photosynthesis begins to rise until 15-25°C where it peaks and then begins to drop after about 25°C. That indicates that these leaves have an optimum temperature of about 15-25°C in which plants perform their biochemical reaction even though photosynthesis can occur over a wider range of temperatures. Foliage water potential (LWP) is the next considered variable that controls photosynthesis. Figure 1c illustrates that it gets increasingly harder to draw water from cells as they get drier with weak negative water potential. NPP remains constant as LWP drops from about 0 to -1 MPa and then decreases linearly after -1 MPa VPD, which is the difference between the amount of moisture in the air and the amount of moisture the air can hold at saturation. Low VPD can cause decay in plants by forming a layer of water around the plant's leaves, while high VPD can cause water stress and the closing of stomates. This effect is more pronounced at higher temperatures are shown in the two separate parts pf the plot (Figure 1d). Higher CO_2 in the air increases photosynthetic rates in jack pine (Figure 1e). Also, from Figure 1f, increased nitrogen potential increases the rate of photosynthesis as nitrogen is an important component in the regeneration of ribulose-1,5-bisphosphate carboxylase/oxygenase (rubisco), which is an enzyme in plant chloroplasts that is involved in the fixation of atmospheric CO_2 during photosynthesis. It is essential to understand that the relationship between environmental controls and productivity becomes more complex as the number of plant categories and climate zones increases (Bonan, 2016).

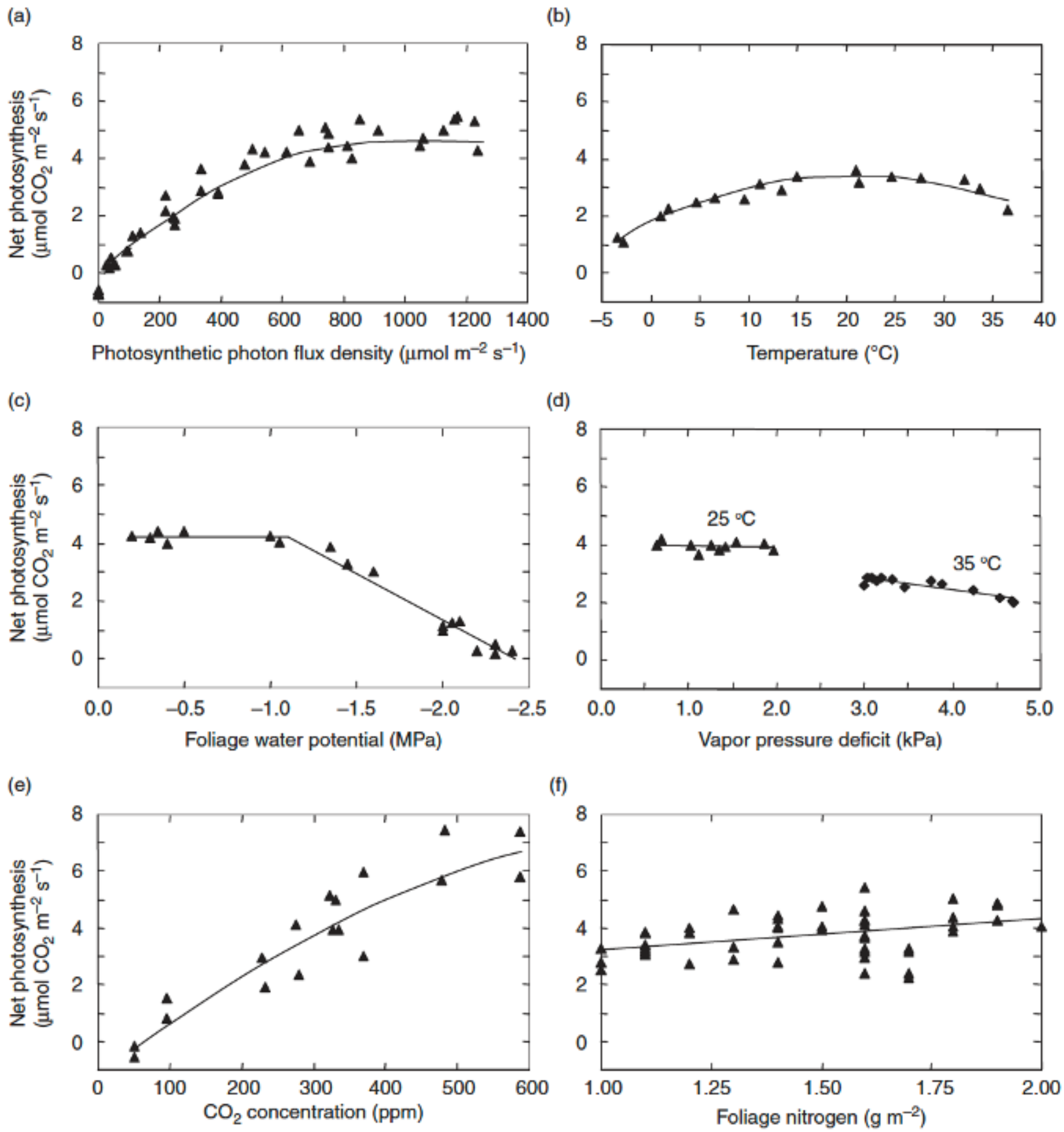

Figure 1. The environmental factors that affect NPP for jack pine trees (Bonan, 2019).

2.1 Measurement of GPP

There are numerous techniques for calculating GPP, including direct measurements conducted on land and indirect assessments made possible by remote sensing via aerial platforms or satellites. The choice of measurement techniques is contingent on the study's specific objectives (including spatial scale), technological capabilities, and available resources, and each strategy has distinct benefits and drawbacks. Over the past two decades, the methodologies used to quantify GPP have undergone significant improvements and innovations, including the use of gas chambers with infrared analyzers, flux towers utilizing eddy covariance techniques, and the analysis of remotely sensed data acquired from airborne imaging devices, primarily satellites, which are then input to models (Berry & Frankenberg, 2012; Mohammed et al., 2019). The following sections present a comprehensive overview of these three frequently employed techniques.

2.1.1 Gas chamber and infrared gas analyzer

Gas chamber measurements typically entail the containment of a limited expanse of surface vegetation (at the plant level) within a transparent chamber, within which photosynthesis and respiration occur simultaneously. When the air in the chamber is isolated from the surrounding atmosphere (in a closed chamber), the rate of change in gas concentrations is observed by measuring its infrared light transmission at wavelengths corresponding to that gas's absorption bands, and this information is recorded over a specified time period (Long, 2003). Net photosynthesis can be estimated by quantifying the flux (rate of exchange of CO_2 and/or oxygen (O_2) per unit area) between the vegetation and the surrounding atmosphere within the chamber in the presence of light and comparing this with a paired reading in the dark, during which only respiration is occurring. The difference between the two fluxes is the photosynthetic rate. It is particularly useful for facilitating the investigation of processes at a smaller scale, such as individual foliage or plants growing on the ground within confined experimental locations. Nevertheless, the quantification of gas chamber measurements is characterized by the requirement of significant labor, extensive time consumption, frequent confinement to studies of limited scale, and potential inadequacy in capturing differences in GPP across different locations (Bonan, 2016).

2.1.2 Flux towers and eddy covariance (EC) techniques

The eddy covariance (EC) technique is a micrometeorological technique employed to quantify the exchange of gases, such as CO_2, CH_4, and water vapor between the underlying surface and the atmosphere. The vertical fluxes of gases in EC systems are continuously monitored through the utilization of fast-response sensors (typically sonic anemometers), which operate based on the principle of turbulent diffusion. The technique involves measuring the velocity and gas concentration of each upward and downward turbulent eddy and computing the net transport of the gas passing through a plane typically located above the top of the plant canopy over a specified time interval. The measurements are constantly ongoing while the device operates however, the data is averaged at set time intervals, typically every 30 minutes since the sensors are very sensitive to little changes. This methodology facilitates the acquisition of uninterrupted measurements on a larger spatial scale (hundreds of squared meters to kilometers), thereby providing significant insights into the daily and yearly fluctuations in GPP from the assemblage of plants making up the habitat, including those growing at ground level. This approach offers a means to obtain real-time and uninterrupted assessments of GPP on a large-scale ecosystem level, effectively capturing the fluctuations in space and time (Baldocchi, 2003; Running et al., 2004).

The EC technique is widely regarded as the most precise approach for quantifying carbon fluxes, as supported by studies conducted by Baldocchi (2003) and Yang et al (2017). Consequently, the calibration and validation of GPP estimates from remote sensing typically involve the utilization of measurements obtained from flux tower sites (Sasai et al., 2007). Flux towers for EC measurements measure net photosynthesis or net ecosystem exchange (NEE) and, therefore, do not measure GPP directly. At the ecosystem level, an estimate of GPP can be obtained using eddy covariance data by Equation 1 that calculates the difference between net ecosystem exchange during the daytime and subtracting modeled total ecosystem respiration (ER) derived from the dependence of nocturnal flux measurements on the temperature (Frankenberg et al., 2011; Yang et al., 2017).

$$\mathrm{GPP} = ER - \mathrm{NEE} \tag{1}$$

The accuracy of the eddy covariance method is maximized under conditions of atmospheric instability, wherein the wind, temperature, humidity, and CO_2 levels are dominated by turbulent diffusion, as is the case during the daytime. Measurements are less accurate under calm conditions. Additionally, the method is most reliable when applied to areas with uniform vegetation and situated on flat terrain, with a sufficient distance upwind to minimize the effects of contamination from distinctly different habitats (Baldocchi, 2003).

The installation and maintenance of flux towers are required for this approach; however, there exists an inequitable and limited global distribution of these towers, and a substantial portion of flux tower data remains inaccessible to the general public (Qiu et al., 2020). Also, GPP measurement by EC is challenging since several variables affect the result. For instance, the compromise created by measurement resolution and spatial averaging owing to tower height may impact GPP readings; therefore, the quality of GPP readings acquired with EC technology varies (Qiu et al., 2020). The current networks of EC tower sites, such as FLUXNET and AmeriFlux, exhibit limited spatial coverage across various regions of Canada, which is primarily attributed to the substantial expenses associated with the establishment and maintenance of these towers (Lees et al., 2018). There is, however, no published flux tower data available for the Bruce Peninsula. These constraints have prompted the development of novel methodologies for estimating models through the utilization of Earth observation and modeling methodologies.

2.1.3 Models for GPP estimation

Models play a pivotal role in estimating global GPP, particularly in situations where direct measurements are impractical or have limited spatial and temporal coverage (Verma et al., 2017). Typically, GPP is estimated at the landscape and regional levels using models and algorithms that combine ground observations with remotely sensed data (Porcar-Castell et al., 2014). Ground measurements are mainly used to validate or calibrate model estimates or fill in the gaps that may exist in the measurement of remotely sensed data. According to Yang et al. (2015) and Li & Xiao (2019), there are three broad classifications of models: 1) process-based models, which are mathematical models that simulate the process of photosynthesis by incorporating physiological and biogeochemical processes 2) machine learning approaches that make use of eddy covariance data, remote sensing products, and climatic products provided in grids; and 3) models for production efficiency based on vegetation indices (VI), derived from satellite data, that indicate greenness. Other scholars have classified sunlight-induced fluorescence (SIF) as an additional category of models. Although some SIF models (e.g., GOME; Joiner et al., (2011) and OCO-2; Frankenberg et al., (2011) can function independently, they also possess certain applications within the other models mentioned. Hence, for parsimony, I opt to refrain from categorizing the SIF approach as a distinct model type.

Process-based models simulate the fundamental physiological and biophysical processes associated with photosynthesis and plant growth. These models are very detailed and integrate various factors, including light availability, temperature, water availability, and carbon allocation in various parts of the ecosystem, in order to estimate GPP. Process-based models require comprehensive input data regarding environmental conditions and plant characteristics, and they offer significant insights into the underlying mechanisms that govern GPP. The process-based modeling approach can be utilized to examine the reactions of GPP under various environmental conditions and ascertain factors that may restrict GPP increase. Some examples of process-based terrestrial ecosystem models are the McGill Wetland Model (MWM, St-Hilaire et al., 2010), Lund-Potsdam-Jena General Ecosystem Simulator (LPJ-GUESS, Chaudhary et al., 2017), and Canadian Land Surface Scheme Including Biogeochemical Cycles (CLASSIC, Melton et al., 2020) which have been used to investigate ecosystem responses to changing environmental conditions.

Process-based models, however, tend to exhibit complexity, are strongly dependent on parameterization, and heavily depend on the availability of precise input data. It is also a significant computational burden, and the task of conducting experiments to isolate crucial model processes is frequently challenging (Bonan, 2019; Xiao et al., 2019).

Data-driven models, such as those employing machine learning techniques, utilize statistical associations between GPP and environmental variables that are obtained from observational data and rely heavily on remotely sensed products (Qiu et al., 2020). The models typically undergo training using large datasets, allowing them to accurately capture complex nonlinear relationships between GPP and various environmental variables. As a result, these models offer the advantage of scalability and can estimate GPP across diverse spatial and temporal scales. These tools prove to be particularly valuable when estimating GPP on a large scale or when there are constraints on obtaining direct measurements. Many research projects have employed data-driven GPP models across different ecosystems, and they have shown good similarity to EC tower estimates (e.g., Yang et al., 2007; Schlund et al., 2020; Qiu et al., 2020)

However, the effectiveness of data-driven models relies on the dependability and comprehensiveness of the training data, and they may demonstrate reduced interpretability compared to process-based models.

The LUE models conceptualize GPP as the outcome of the absorbed photosynthetically active radiation (APAR) multiplied by the actual light use efficiency (Yang et al., 2007; Schlund et al., 2020). LUE is defined as the effectiveness of the photosystems in plants utilizing absorbed light energy for carbon fixation. There are two primary assumptions underlying this concept. First, it is assumed that GPP exhibits a linear relationship with absorbed APAR. Secondly, it is theorized that the actual LUE of a plant, denoted as ε_g, is reduced from its maximum theoretical value ε_0 due to various environmental factors, such as temperature or water stress. The LUE-based model can be mathematically represented in a general form as follows:

$$\mathrm{GPP} = \mathrm{APAR} \times \varepsilon_g \tag{2}$$

$$\text{APAR} = \text{PAR} \times \; FPAR \tag{3}$$

$$\varepsilon_g = \varepsilon_0 \times \; f(\text{T}, \text{SW}, \dots) \tag{4}$$

where PAR denotes photosynthetically active radiation, FPAR represents the proportion of PAR that is absorbed, and $f(\text{T}, \text{SW}, \dots)$ denotes the functional dependence on various environmental factors, including air temperature $f(T_a)$ and soil water $f(SW)$ (Pei et al., 2022). These GPP models typically rely on VIs, such as the Normalized Difference Vegetation Index (NDVI) and the Enhanced Vegetation Index (EVI) (Running et al., 2004; Xiao & Moody, 2004; Huang et al., 2019). In recent years, SIF readings have been used in models to obtain estimates of GPP by replacing *f*PAR in Equation 3 with SIF readings.

LUE models are the most widely used model-based methods for measuring GPP globally (Liao et al., 2023) and have relatively simple model structure with a minimal number of parameters, yet have been able to provide estimates of GPP that show good ($R^2 > 7.0$) statistical agreement with EC tower measurements (Xiao & Moody, 2004). Some examples of LUE models developed over the past three decades include the Carnegie-Ames-Stanford Approach model (CASA, (Potter et al., 1993), MODIS GPP algorithm (MOD17, (Running et al., 2004), Vegetation Photosynthesis Model (VPM, (Xiao, 2004), and Eddy Covariance-Light Use Efficiency model (EC-LUE, (Yuan et al., 2007). These satellite data-driven LUE models have been widely used to estimate carbon fluxes for many ecosystem types, such as forests and croplands.

The challenge with the LUE model is that it depends upon various *in situ* parameters. Consequently, each parameter's precision will impact the estimated GPP's accuracy. It is challenging to accurately estimate light use efficiency (ε) and APAR at large spatial extents because these parameters may vary with different biomes, physiological factors, and environmental conditions (Medlyn, 1998; Frankenberg et al., 2011).

SIF refers to the fluorescent emission exhibited by plants when exposed to sunlight. This phenomenon arises from the energy flux released by chlorophyll molecules within the plants, with wavelengths falling within the range of 600 to 800 nm (Maxwell & Johnson, 2000). Recent advances in remotely sensed sunlight-induced fluorescence (SIF) measurements, retrievals, and modeling have provided an alternative approach to determining the photosynthetic activity of terrestrial ecosystems. There is extensive evidence that SIF has the potential to estimate actual primary productivity because it is a direct by-product of photosynthesis, rather than the maximum photosynthetic capacity or greenness of the vegetation, which the VIs provides (Frankenberg et al., 2011; Porcar-Castell et al., 2014). These VIs cannot reveal short-term ecophysiological responses and may induce delayed responses in revealing stressors in the responses of vegetation (Glenn et al., 2008; Verma et al., 2017). For example, NDVI may demonstrate a delayed response to changes in the state of the vegetation state from ten days to two months (Zhang et al., 2016).

At a fundamental level, the fluorescence process involves capturing light energy by chlorophyll molecules in leaves, which is subsequently transferred to the reaction centers. This energy is then released through three distinct pathways: photochemistry, non-photochemical quenching, which involves the dissipation of heat, and a minor portion that is re-emitted as chlorophyll fluorescence (Maxwell & Johnson, 2000; Kalaji et al., 2017). SIF evolved from pulse-induced chlorophyll fluorescence, which has been used to understand plant photosynthesis for decades in laboratory, field, and plot-level studies (Maxwell & Johnson, 2000; Verma et al., 2017) and now, satellite measurements of chlorophyll fluorescence detected at the canopy and landscape levels can give insight into plant processes and photosynthesis (GPP) (Meroni et al., 2009; Frankenberg et al., 2011; Verma et al., 2017; Yang et al., 2017).

Research conducted in various terrestrial ecosystems, including forests, croplands, and savannas, has demonstrated that solar-induced fluorescence (SIF) has proven to be a valuable tool for enhancing the accuracy of estimates of GPP obtained through remote sensing techniques (Guanter et al., 2014; Perez-Priego et al., 2015; Walther et al., 2016). These studies have advocated the utilization of satellite-derived SIF in models due to its superior accuracy in estimating GPP compared to satellite-derived vegetation indices (VIs). This approach has been supported by the findings of Luus et al. (2017) and Li et al. (2018), who have demonstrated the greater effectiveness of SIF in capturing the impact of environmental stress on the GPP (Lee et al., 2013). Similarly, Yang et al. (2015) discovered a significant and robust association between SIF and GPP, with SIF exhibiting a closer correlation to GPP compared to vegetation indices (VIs) in temperate deciduous forests.

The main satellite platforms/instruments providing SIF observations to the scientific community include Greenhouse Gases Observing SATellite (GOSAT; Frankenberg et al., 2011, Joiner et al., 2011), Global Ozone Monitoring Experiment-2 (GOME 2; Joiner et al., 2013), SCanning Imaging Absorption SpectroMeter for Atmospheric CHartographY (SCIAMACHY; Köhler et al., 2015), and the Orbiting Carbon Observatory-2 (OCO-2; Frankenberg et al., 2014).

The technique of measurement of SIF from space entails using the principle of the infilling of the Fraunhofer lines. The Fraunhofer lines are dark lines in the solar spectrum that correspond to the absorption of light by atmospheric gases e.g., CO_2. The infilling of these lines takes place when the light is absorbed by chlorophyll molecules in plants and re-emitted as fluorescence (Frankenberg et al., 2011). Studies have shown that SIF from the GOSAT

(Frankenberg et al., 2012) and GOME-2 (Joiner et al., 2014) correlate well with GPP estimated by the data-driven algorithms such as MPI-BGC (Jung et al., 2011) and LUE type models such as MOD17A2 (Running et al., 2004). Because it provides a functional link with dynamic changes in photosynthetic carbon assimilation, SIF has also been integrated into land surface models such as the Soil Canopy Observation of Photosynthesis Energy Balance (SCOPE; Tol et al., 2014) and the Community Land Model (CLM; Lee et al., 2015).

Despite the immense potential of satellite-based SIF, there have been some concerns about their application in modeling ecosystem productivity (Xiao et al., 2019). It has been shown that the relationship between SIF and GPP at the leaf or canopy scale is complex and may become nonlinear or even reverse direction under certain physiological and environmental conditions (Porcar-Castell et al., 2014; Verma et al., 2017). This relationship is also known to be biome-dependent, which could be a problem because of the generally coarse spatial resolutions that SIF measurements offer (e.g., GOSAT and GOME-2 (GOME-2: 40 × 80 km; GOSAT: 10 km diameter) – (Frankenberg et al., 2011; Joiner et al., 2011; Guanter et al., 2012).

3 Methodology

3.1 Study site description

The Bruce Peninsula (Figure 2) has a land area of 956.5 km^2, and it separates Georgian Bay from the central basin of Lake Huron. It is in Southern Ontario (44°56’43" N, 81°16’36" W).

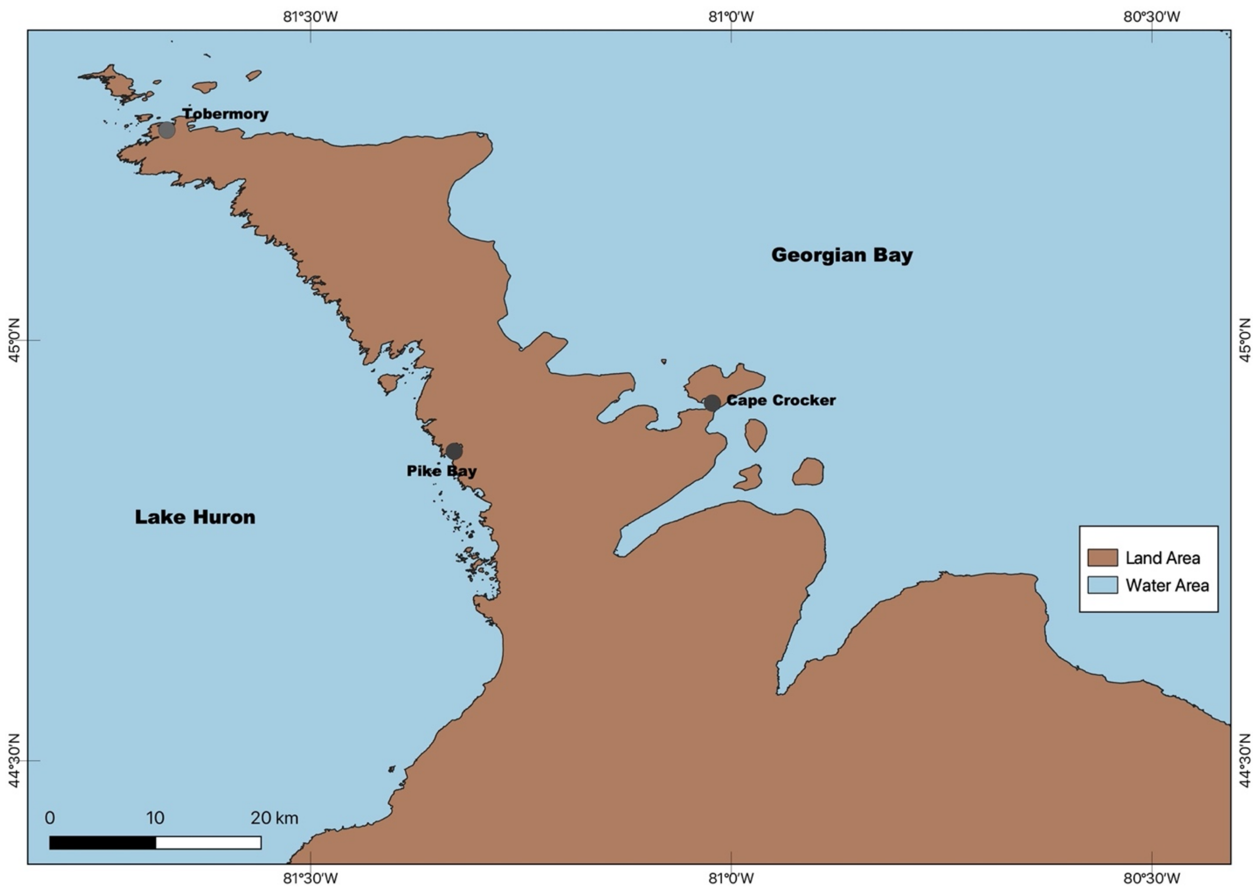

Figure 2. Map of study area showing the Bruce Peninsula.

The Bruce Peninsula is known as one of the Great Lakes biodiversity hotspots, with some rare plant and animal species, and has been known to have some of the most intact natural ecosystems in Canada (Liipere, 2014). Parts of the Peninsula have been recognized as a World Biosphere Reserve by the UNESCO. The area is dominated by the iconic cliffs of the Niagara

Escarpment, which combine with the influence of the Great Lakes to create unique ecological conditions (Liipere, 2014). The Bruce Peninsula consists of several ecosystems, including vast forests, open grasslands, and inland lakes. The forest classifications include deciduous, coniferous, and mixed forests. Also, the open fields include croplands, hayfields, and pastures (Liipere, 2014). The Bruce Peninsula generally does not have suitable soils for crop production between the stony/rocky land type, topography, and poor drainage; however, there are a few areas that are considered prime agricultural lands (Liipere, 2014).

Due to its location, the Bruce Peninsula has a maritime climate influenced by the Great Lakes and has a humid and temperate climate, having warm summers (mean 16°C) and cool winters (mean -6.7°C). The summer period is characterized by hot, humid air masses from the Pacific Ocean and the Gulf of Mexico. The winter season records an increase in Pacific air, which is replaced by Arctic currents as the season progresses (Liipere, 2014). Precipitation occurs year-round, with the peak between September and November. The large water bodies (Lake Huron and Georgian Bay) surrounding the Peninsula serve as a buffer from extreme macroclimatic conditions. The dominant land cover type is forest, and it represents 69% of the total land area. Of this percentage, 46% is coniferous, 14% is deciduous, and 8% is mixed forest. Agricultural land cover is the next most dominant land cover type with 16%. The other uses of the land (community-residential areas and roads) represent 2% of the total land area (Liipere, 2014).

The Bruce Peninsula holds the largest continuous forest in Southern Ontario, which stretches from Tobermory to Lion's Head to an area near Pike Bay and along the Niagara escarpment. The forest in the Bruce has undergone a lot of drastic changes since the first

European settlement from being an area of extensive lumber to a protected environmentally significant area (Liipere, 2014).

The most common trees in the forests are sugar maple (*Acer saccharum*), white cedar (*Thuja occidentalis*), white birch (*Betula papyrifera*), trembling aspen (*Populus tremuloides*), large-toothed aspen (*Populus grandidentata*), balsam fir (*Abies balsamea*), and white spruce (*Picea glauca*). The distribution of the trees is mainly determined by the soil type, soil moisture, soil depth, and fire history. The vegetation distribution in the Bruce Peninsula was significantly impacted by a substantial fire that burned most of the Bruce Peninsula in 1908, resulting in the subsequent regrowth of vegetation (Liipere, 2014). Consequently, the majority of the oldest trees in the Peninsula are approximately 115 years old.

3.2 Site selection and data processing

I extracted the GPP_{GOSIF} data values to points utilizing R (R Core Team, 2023) from the GeoTIFF files for my study region. To compare the two models, I additionally downloaded the corresponding GPP_{MODIS} file containing cells within the GPP_{GOSIF} boundaries. Since the GPP_{GOSIF} cells are larger, they were used as the study sites (Figure 3).

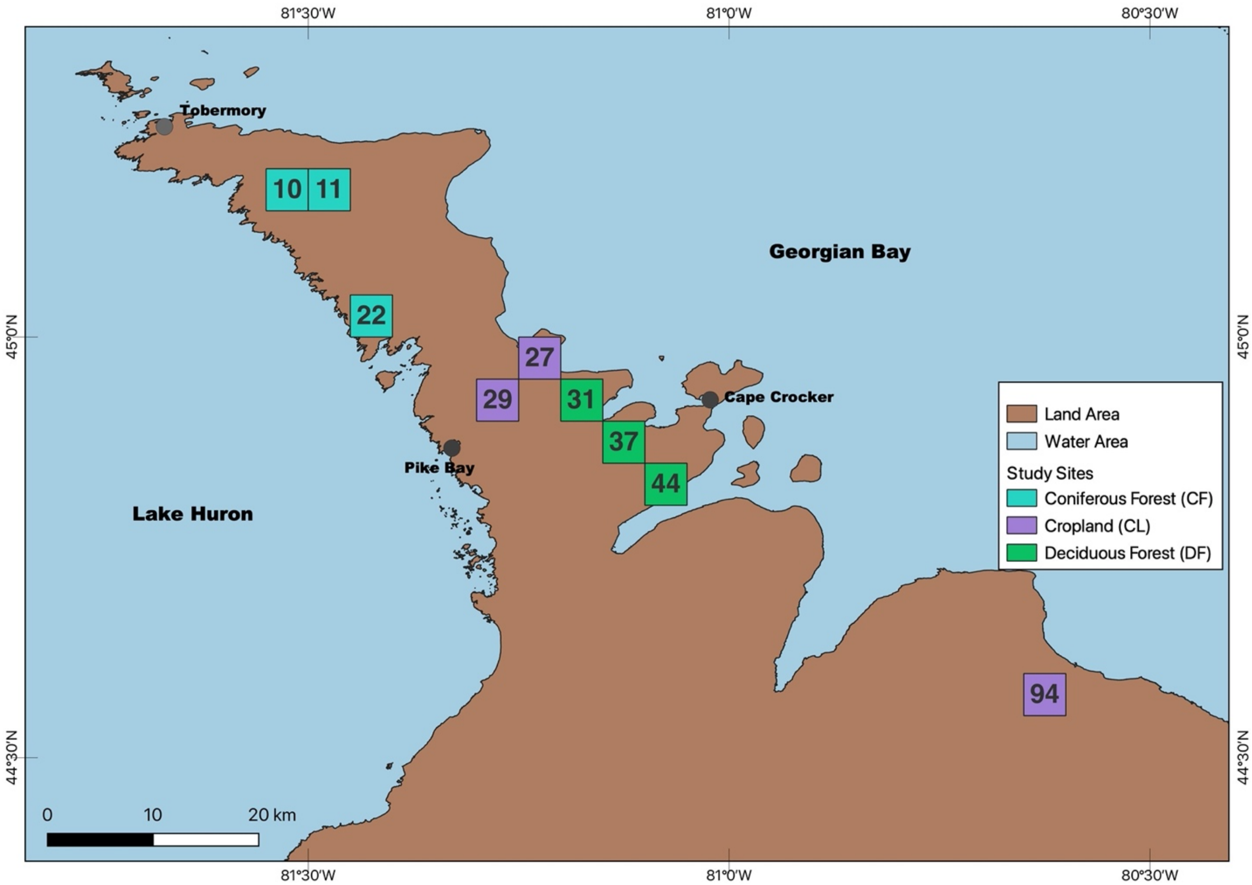

Figure 3. Map of the Bruce Peninsula showing the study sites.

Using the Canada Land Cover 2020 data (Latifovic et al., 2017; Latifovic, 2023) with a spatial resolution of 30 m in conjunction with the GPP_{GOSIF} pixels to generate a zonal histogram containing the land cover distribution of the land cover distribution in each cell constituted the remaining criteria for site selection (Table 1). I determined the relative percentages of each of the land cover types within each of the study sites, which aided me in determining the land cover selections for the sites.

Table 1. GPP_{MODIS} cells (*n*) averaged to produce comparable estimates of GPP_{GOSIF} (adapted as the study sites).

Site ID	**(*n*)**
CF 10	121
CF 11	121
CF 22	116
CL 27	121
CL 29	121
DF 31	108
DF 37	121
DF 44	77
CL 94	121

According to land cover data, the three most prevalent vegetation land cover categories on the study site, in terms of area, are deciduous forest, coniferous forest, and cropland. The objectives of this research necessitated the selection of as uniform as possible pixels representing each land cover type. To achieve this, three examples of each land cover type were selected based on the highest percentage of that land cover type in each cell (Table 2).

Table 2. Indicating study sites and the percentage of the land cover (LC) type present within the cells. CF is a coniferous forest, DF is a deciduous forest, and CL is cropland.

Site ID	**LC (%)**
CF 10	89
CF 11	82
CF 22	83
CL 27	81
CL 29	88
CL 94	79
DF 31	70
DF 37	70
DF 44	51

The study sites are so large in spatial extent (~5 km) that it will be impossible to identify and select three locations that are purely of a single land-cover type (*n* = 9). Due to the inevitable heterogeneity in composition, as measured by leaf area index (LAI), species composition, and above-ground biomass at the selected sites, three samples of each vegetation community were collected to provide averages of the prevalent conditions. The Bruce Peninsula's land mass covered approximately 100 GPP_{GOSIF} cells, and cells 10, 11, 22, 27, 29, 31,37, 44, and 94 in the study area were selected based on the above-described criteria under each of the three vegetation land cover types (Figure 3).

Within each of the nine designated GPP_{GOSIF} sites, a maximum of 121 cells, each with a spatial resolution of 500 m GPP_{MODIS} cells, were selected. Some sites displayed fewer than 121 cells due to the presence of unidentifiable land cover types. For example, there are numerous missing pixels on DF 44 because a significant portion of that site lies within Georgian Bay. In all 9 locations for each month of the study period, the mean GPP for the higher spatial resolution GPP_{MODIS} sites was compared to the corresponding values for the coarser spatial resolution GPP_{GOSIF} sites.

Regardless, under the premise that both models provide perfect estimates of GPP, the mean GPP of the 121 GPP_{MODIS} pixels falling within each of the nine SIF pixels should agree perfectly with the SIF estimate. Biases in the mean GPP_{MODIS} could be due to deficiencies in either or both models or could be due to the aforementioned variations in land cover type.

Using Julian dates, specific days of the year were used to distinguish among each season over the course of 20 years. Winter (December, January, and February), Spring (March, April, and May), Summer (June, July, and August), and Fall (October, November, and December) were the four seasons.

The ERA-5 dataset consists of pixels with a coarser spatial resolution (31 km) compared to the GPP_{GOSIF} dataset (~5 km). The ERA-5 pixels form the climate zones 1 to 5. In two instances, the climate contains more than one study location, and in three instances, a singular site (Table 3).

Table 3. Climate zones (CZ) adapted from ERA-5 pixels with the corresponding study sites included within each zone.

CZ	Sites
1	CF 10, CF11
2	CF 22
3	CL 27, CL29, DF31, DF37
4	DF 44
5	CL 94

3.3 Datasets

3.3.1 Climatic data

Climate model data was needed to i) assess the strength of any long-term trends in seasonal climate since 2000 and ii) quantify the response of modeled gross primary productivity to variations in growing conditions over the study period. The climate model data used was ERA-5, which is a dataset that provides global high-quality atmospheric reanalysis data for climate and weather research at a spatial resolution of approximately 31 km. It was created by the European Centre for Medium-Range Weather Forecasts (ECMWF) and spans from 1979 to the present. The ERA-5 data includes numerous variables, such as temperature, pressure, wind, humidity, precipitation, cloud cover, and radiation. These variables are accessible at various vertical levels and temporal resolutions, ranging from hourly to monthly. The data is generated using an advanced global atmospheric model that assimilates observations from satellites and ground measurements. The process of reanalysis ensures that the data are consistent and homogeneous, thereby providing a reliable and accurate representation of the global climate system. The data was accessed from the C3S climate data store Application Programming Interface (Hersbach et al., 2020). The ERA-5 data variables I acquired in this research were air temperature at 2 m (TEMP, °C), total precipitation (PREC, mm), volumetric soil water from 7-28 cm in depth (VSW, m^3m^{-3}), surface solar radiation downward (SSRD, Wm^{-2}) and dew point temperature (TD, °C) which will be needed for calculations of vapor pressure deficit (VPD, kPa).

VPD influences stomatal opening and, consequently, stomatal, leaf, and canopy conductance (Bonan, 2016). This parameter influences the ease with which carbon dioxide and water vapor can enter and exit the plant, respectively. VPD can be interpreted as the air's dryness, or the humidity required to saturate the air. The vapor pressure deficit (VPD) was calculated from the 2-m air temperature and dew point temperature from ERA-5 from:

$$\text{VPD} = e_{sT} - e_{sTd} \tag{5}$$

where saturation vapor pressure (Buck, 1981) as:

$$\mathrm{e}_s = 0.611 \exp\left((17.267 * \mathrm{T}) / (238.8 + \mathrm{T})\right) \qquad \text{[kPa; °C]} \tag{6}$$

$$\text{VPD} = 0.611 \exp((17.267 * \mathrm{T}) / (238.8 + \mathrm{T})) - 0.611 \exp((17.267 * \mathrm{T_d}) / (238.8 + \mathrm{T_d})) \tag{7}$$

The term e_{sT} is the air's saturation vapor pressure at its temperature T, and e represents the actual water vapor pressure of air. T_d or the dew point temperature, is the temperature at which the air must be cooled in order to become saturated (to attain 100% relative humidity) without adding or removing water.

3.3.2 GPP model data

The SIF-based GPP data was acquired from the GOSIF GPP archived model data (Li & Xiao, 2019), which has a spatial resolution of approximately 5.5 km at the equator and is available at multiple temporal resolutions (Li & Xiao., 2019). The 1-month temporal resolution data was used in this research because of the seasonal approach of the analysis**.** This dataset is mainly based on SIF data onboard the OCO-2 satellite. The GPP_{GOSIF} dataset is modeled from a data-driven model that integrates remotely sensed MODIS data with meteorological reanalysis data because the National Aeronautics and Space Administration (NASA) OCO-2 data is not available globally. Li & Xiao (2019) trained with extensive data to be able to produce representative non-linear GPP data from the input data, which is also gap-filled to provide estimates for unavailable data. Gap-filling is the process by which contaminated readings are replaced with interpolated values to calculate for GPP. The correlation between the GPP estimates and the global estimates from 91 flux towers data is extraordinarily high ($R^2 = 0.74$). Compared to the original satellite OCO-2 SIF estimates (launched in 2014), these data have a finer spatial and temporal resolution, continuous global coverage, and an extended measurement history (computed from 2000). This dataset has been used and validated by other researchers (Qiu et al., 2020; Zhang et al., 2021).

The GPP_{MODIS} product acquired for this research is the MOD17A2HGF version 6.1, which is derived from two NASA Earth Observing System (EOS) satellites: Tera and Aqua (ORNL DAAC, 2018; Running & Zhao, 2021b). The GPP_{MODIS} product is a 500 m spatial resolution, 8-day aggregate of GPP readings to model and measure GPP; the MOD17A2HGF algorithm combines remote sensing data, meteorological data, and biophysical models. The algorithm is founded on the LUE theory, which assumes that plant productivity is proportional to the FPAR absorbed by vegetation and that the efficiency of using this PAR to produce biomass remains constant over time. The MOD17A2HGF algorithm incorporates multiple sources of input data, including MODIS surface reflectance data, MERRA-2 meteorological data, and a MODIS Land Cover Classification (MCDLCHKM). To validate MOD17A2HGF estimates, ground-based measurements such as eddy covariance measurements, biomass captures, and other field data are utilized to evaluate the model's accuracy and enhance it over time. This dataset has been used and validated by other researchers (e.g., Wang et al., 2017; Park et al., 2019; Ferreira et al., 2021).

Only vegetated surfaces provide MOD17A2 product values; other surface types, such as water bodies, salt, tundra, rock, built-up areas, and unclassified regions, yield flagged outputs to be disregarded. Additionally, different detector and cloud cover conditions help evaluate if the model's output is suitable for usage. In order to compute GPP, polluted measurements are filled with LAI/FPAR values using the gap-filling method. The data used in this research is filtered, gap-filled, and has undergone quality control. The data administrators have been deemed usable based on their standards established (ORNL DAAC, 2018). Throughout this thesis, GOSIF GPP – which is a data-driven model, will be referred to as GPP_{GOSIF}, and the MODIS GPP – which is an LUE model, will be referred to as GPP_{MODIS}.

3.4 Statistical analyses

The Shapiro-Wilk test and Q-Q plots were used to determine the normality of the relationships, and nonparametric tests were used to determine the statistical significance of *p* values at a minimum alpha level of 95% ($p < 0.05$). In all cases, I report the *p*-value ranges: $p < 0.05$, $p < 0.01$, $p < 0.001$ denoted by *, **, and ***, respectively.

. From the standpoint of climate change, two aspects of environmental influence on GPP were investigated. These are variations in GPP over time and GPP response to climatic stresses.

Time series were plotted together with a Mann-Kendall (MK) approach using the 'Kendall' package in R (McLeod, 2011). Also, a Sen slope used through the 'zyp' package (Bronaugh et al., 2023) was also performed on the data to determine the direction of the slope in the trends. MK is a non-parametric tool that is used to detect monotonic trends in a time series. The tests were conducted in the R environment to ascertain whether GPP or any climatic variables exhibit a significant trend. The hypotheses for the trend analysis are as follows:

H_0: There is no significant trend in the time series data, as assessed using the Mann-Kendall test and Sen slope analysis.

H_1: There is a significant trend in the time series data, as determined by the results obtained from the Mann-Kendall test and Sen slope analysis.

The response analysis examined the Pearson's correlation coefficient (R) of GPP when correlated with each environmental variable to standardize the effect sizes (Baguley, 2009) and to assess which of the environmental variables constitutes the strongest effect on the modeled GPP. This was accomplished by calculating the probability that R is real using its p-value. The response analysis was conducted for all land cover types and across all seasons individually for both GPP models using both the least squares regression ('lm' function) and the Theil-Sen Regression approach from 'RobustLinearReg' package (Santiago, 2020) functions in the R Environment. The Theil-Sen regression approach is based on the median of all pair-wise combinations of the slopes of data points, making it less affected by outliers. I then extracted the coefficients corresponding to the best-fit line, followed by correlation analysis to obtain coefficients of determination and statistical significance using the 'cor.test' function in the R environment. Multivariate analysis is not employed because several of these variables are highly interrelated (e.g., insolation and VPD). The hypotheses for the correlation analysis are as follows:

H_0: There is no significant correlation between seasonal interannual variability in GPP and climate variability, as assessed using the Pearson correlation coefficient tests.

H_1: There is a significant correlation between seasonal interannual variability in GPP and climate variability, as assessed using the Pearson correlation coefficient tests.

On an annual (n = 20 years) and seasonal basis, trends over time were evaluated to determine if GPP trends were seasonal. The GPP responses to environmental variables were determined by first transforming the GPP data to anomalies from the long-term mean and then similarly transforming the climate data to anomalies from the long-term mean, as offered by Bello & Higuchi (2019).

$$\text{Anomaly} = \text{Present} - \text{Mean} \tag{8}$$

With these anomalies, the probability that the intercepts are significant may also have some physical significance, as it considers the change effect rather than the actual values, which can be evaluated by determining whether $p < 0.05$ for the intercepts.

In the model comparison, both models were regressed against each other to establish the relationship between them. Also, *t* tests and two-way Tukey Honestly Significance Difference (HSD) tests together with ANOVAs were performed to determine if there were significant differences in the mean GPP with cover type and season from both models. For the *t* tests, the hypothesis is as follows:

H_0: There is no significant difference between both GPP models, as assessed using *t* tests.

H_1: There is a significant difference between both GPP models, as assessed using *t* tests.

Also, for the ANOVA tests, the hypothesis is as follows:

H_0: There is no significant difference among land cover types, as assessed using ANOVA tests.

H_1: There is no significant difference among land cover types, as assessed using ANOVA tests.

4 Results

4.1 Land cover comparison

On a long-term annual basis, GPP for the 20 years was greatest for the deciduous forest (DF), followed by cropland (CL) and then coniferous forest (CF) as per the GPP_{GOSIF} model results (Table 4). GPP_{MODIS} also shows DF having the highest GPP, although CF was about 8% more productive than CL. The annual daily average GPP of the coniferous forest, croplands, and deciduous forests are 3.32 $gCm^{-2}d^{-1}$, 4.17 $gCm^{-2}d^{-1}$, and 4.84 $gCm^{-2}d^{-1}$ on average respectively according to GPP_{GOSIF}. Alternatively, according to GPP_{MODIS}, the annual productivity of coniferous forests is 4.03 $gCm^{-2}d^{-1}$, cropland is 3.74 $gCm^{-2}d^{-1}$, and deciduous forest is 4.21 $gCm^{-2}d^{-1}$.

Table 4. Twenty-year seasonal and annual mean GPP ± standard deviation for all nine sites and land cover types for both models. For the first year (2001), data in all cases start from the Spring, and GPP_{MODIS} is missing data for the spring of 2002. Units for GPP are in $gCm^{-2}d^{-1}$.

	WINTER		SPRING		SUMMER		FALL		ANNUAL	
	GPP_{GOSIF}	GPP_{MODIS}	GPP_{GOSIF}	GPP_{MODIS}	GPP_{GOSIF}	GPP_{MODIS}	GPP_{GOSIF}	GPP_{MODIS}	GPP_{GOSIF}	GPP_{MODIS}
CF	**0.97 ± 0.09**	**0.18 ± 0.09**	**2.63 ± 0.40**	**3.18 ± 0.79**	**6.73 ± 0.46**	**9.08 ± 0.44**	**2.86 ± 0.28**	**3.46 ± 0.32**	**3.32 ± 2.14**	**4.03 ± 3.30**
CF10	1.01 ± 0.07	0.21 ± 0.10	2.91 ± 0.28	3.25 ± 0.81	7.12 ± 0.40	9.18 ± 0.42	3.05 ± 0.25	3.52 ± 0.31	3.55 ± 2.26	4.09 ± 3.30
CF11	1.00 ± 0.05	0.20 ± 0.31	2.77 ± 0.25	3.22 ± 0.81	6.56 ± 0.35	9.27 ± 0.39	2.88 ± 0.22	3.49 ± 0.31	3.33 ± 2.04	4.10 ± 3.35
CF22	0.89 ± 0.08	0.14 ± 0.07	2.20 ± 0.22	3.09 ± 0.79	6.53 ± 0.37	8.78 ± 0.39	2.65 ± 0.20	3.37 ± 0.34	3.09 ± 2.12	3.90 ± 3.18
CL	**0.45 ± 0.07**	**0.09 ± 0.05**	**2.39 ± 0.83**	**2.51 ± 0.74**	**9.93 ± 0.95**	**9.00 ± 0.44**	**3.74 ± 0.83**	**3.13 ± 0.30**	**4.17 ± 3.36**	**3.74 ± 3.32**
CL27	0.49 ± 0.06	0.09 ± 0.05	1.66 ± 0.47	2.40 ± 0.75	9.14 ± 0.49	8.81 ± 0.38	2.79 ± 0.27	3.06 ± 0.32	3.56 ± 3.39	3.65 ± 3.27
CL29	0.46 ± 0.07	0.10 ± 0.05	2.88 ± 0.83	2.56 ± 0.75	9.76 ± 0.79	9.10 ± 0.45	4.55 ± 0.51	3.16 ± 0.30	4.46 ± 3.48	3.79 ± 3.37
CL94	0.41 ± 0.04	0.10 ± 0.05	2.62 ± 0.58	2.56 ± 0.75	10.88 ± 0.55	9.10 ± 0.45	3.88 ± 0.40	3.16 ± 0.30	4.50 ± 3.96	3.79 ± 3.37
DF	**0.52 ± 0.06**	**0.07 ± 0.04**	**2.52 ± 0.77**	**2.73 ± 0.80**	**12.16 ± 1.93**	**10.35 ± 0.47**	**3.96 ± 0.78**	**3.42 ± 0.35**	**4.84 ± 4.57**	**4.21 ± 3.85**
DF31	0.45 ± 0.03	0.07 ± 0.04	2.64 ± 0.75	2.86 ± 0.87	13.11 ± 0.69	10.76 ± 0.37	4.21 ± 0.47	3.59 ± 0.33	5.16 ± 4.87	4.39 ± 4.02
DF37	0.54 ± 0.04	0.07 ± 0.04	2.96 ± 0.71	2.71 ± 0.79	13.68 ± 0.90	10.35 ± 0.32	4.55 ± 0.56	3.39 ± 0.34	5.49 ± 5.04	4.20 ± 3.86
DF44	0.55 ± 0.06	0.07 ± 0.05	1.95 ± 0.48	2.64 ± 0.77	9.69 ± 0.68	9.95 ± 0.30	3.12 ± 0.40	3.28 ± 0.33	3.87 ± 3.56	4.05 ± 3.71
Total	**0.65 ± 0.24**	**0.12 ± 0.08**	**2.51 ± 0.69**	**2.81 ± 0.82**	**9.61 ± 2.56**	**9.48 ± 0.77**	**3.52 ± 0.82**	**3.34 ± 0.36**	**4.11 ± 3.64**	**3.99 ± 3.49**

GPP_{GOSIF}, results show CF had the highest productivity in the winter, about double that of the other land cover types. In the spring, the readings were identical for all the land cover types, and the disparities between the various land cover types were more pronounced in the summer. In comparison to CF, DF was higher and considerably greater ($p < 0.001$). Additionally, DF greatly outweighed CL ($p < 0.01$). CL and DF were about equal in the fall, while CF was the smallest observed value (Table 4, Figures 4 & 5)

GPP_{MODIS} indicates that all land cover categories had negligible values in the winter, but CF was the greatest. CF was the highest in the spring, then DF, and finally CL (CF and CL were significantly different at $p < 0.01$). Summertime saw the greatest levels of GPP for DF, which was about 22% larger than CF ($p < 0.001$), and then CL ($p < 0.001$). CL declined slightly in the fall, while CF and DF were similar (Table 4).

The GPP means of the land cover varied significantly in the ANOVA results from both models (Tables 5 and 6). The ANOVA results below indicate that there are significant differences between the different land cover types and the seasons for both GPP_{GOSIF} (Table 5) and GPP_{MODIS} (Table 6), respectively. For GPP_{GOSIF} land cover, F (2,6) = 10.340, $p < 0.001$; the seasons show F (3,6) = 209.334, $p < 0.001$. The GPP_{MODIS} land cover shows F (2,6) = 24.400, $p < 0.001$; the seasons also show F (3,6) = 5209.290, $p < 0.001$. It is, therefore meaningful to assess the two-way Tukey HSD test to determine the significant differences in the two-way relationships.

Table 5. ANOVA results for GPP_{GOSIF} against land cover (LC) and season. The degrees of freedom are represented by *i.* SS and MS refer to sum square and mean square respectively.

	i	**SS**	**MS**	***F***	***p***	
LC	2	13.40	6.69	10.340	5.8E-04	***
Season	3	406.20	135.41	209.334	2.0E-16	***
LC:Season	6	33.80	5.63	8.706	4.3E-05	***
Residuals	24	15.50	0.65			

Table 6. ANOVA results for GPP_{MODIS} against land cover (LC) and season. The degrees of freedom are represented by *i.* SS and MS refer to sum square and mean square, respectively.

	i	**SS**	**MS**	***F***	***p***	
LC	2	1.30	0.66	24.400	1.7E-06	***
Season	3	422.30	140.78	5209.290	2.0E-16	***
LC: Season	6	3.10	0.51	19.030	4.8E-08	***
Residuals	24	0.60	0.03			

The Tukey HSD results (Table 7) further indicated the two-way relationships between variables within each model and season. On a seasonal scale, for GPP_{GOSIF}, the only significant differences between land cover types occurred in the summertime between the coniferous forests (CF) and the two other land cover types (CF:CL – $p < 0.01$; CF:DF – $p < 0.001$). However, GPP_{MODIS} shows a significant difference between deciduous forests (DF) and the other land cover types in the summertime ($p < 0.001$) and one in the spring between CL and CF ($p < 0.01$) (Table 8).

Table 7. Two-way Tukey HSD test results for land cover means in each season for GPP_{GOSIF} from ANOVA results.

Comparison	diff	lwr	upr	*p*	
CL: WIN-CF: WIN	-0.5	-2.9	1.9	1.000	
DF: WIN-CF: WIN	-0.5	-2.8	1.9	1.000	
DF: WIN-CL: WIN	0.1	-2.3	2.4	1.000	
CL: SPR-CF: SPR	-0.2	-2.6	2.1	1.000	
DF: SPR-CF: SPR	-0.1	-2.5	2.3	1.000	
DF: SPR-CL: SPR	0.1	-2.2	2.5	1.000	
CL: SUM-CF: SUM	3.2	0.8	5.6	0.003	**
DF: SUM-CF: SUM	5.4	3.1	7.8	0.000	***
DF: SUM-CL: SUM	2.2	-0.1	4.6	0.077	
CL: FAL-CF: FAL	0.9	-1.5	3.2	0.964	
DF: FAL-CF: FAL	1.1	-1.3	3.5	0.863	
DF: FAL-CL: FAL	0.2	-2.1	2.6	1.000	

Table 8. Two-way Tukey HSD test results for land cover means in each season for GPP_{MODIS} from ANOVA results.

Comparison	**diff**	**lwr**	**upr**	***p***	
CL: WIN-CF: WIN	-0.1	-0.6	0.4	1.000	
DF: WIN-CF: WIN	-0.1	-0.6	0.4	0.999	
DF: WIN-CL: WIN	0.0	-0.5	0.5	1.000	
CL: SPR-CF: SPR	-0.7	-1.2	-0.2	0.002	**
DF: SPR-CF: SPR	-0.5	-0.9	0.0	0.085	
DF: SPR-CL: SPR	0.2	-0.3	0.7	0.845	
CL: SUM-CF: SUM	-0.1	-0.6	0.4	1.000	
DF: SUM-CF: SUM	1.3	0.8	1.8	0.000	***
DF: SUM-CL: SUM	1.4	0.9	1.8	0.000	***
CL: FAL-CF: FAL	-0.3	-0.8	0.2	0.394	
DF: FAL-CF: FAL	0.0	-0.5	0.4	1.000	
DF: FAL-CL: FAL	0.3	-0.2	0.8	0.574	

From the 20-year annual mean data bar plots, the median values were almost identical (Figure 4). But GPP_{GOSIF} DF had the largest inter-annual range of values seasonally, followed by CL and then CF. However, for GPP_{MODIS}, DF has the largest range of values, followed by CF and CL.

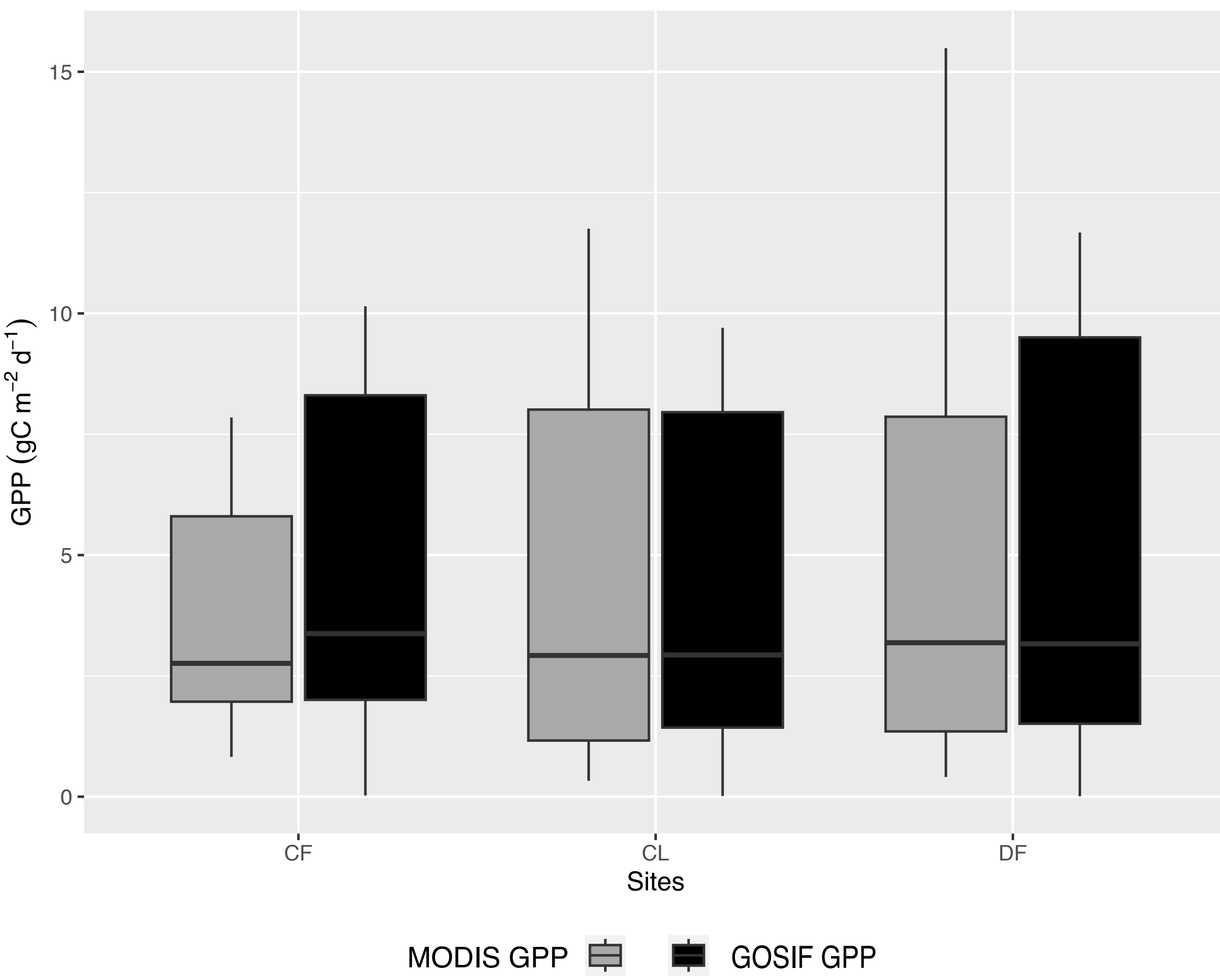

Figure 4. Box plot of 20-year annual average GPP for the three land cover types (averaging all three CF, CL, and DL sites, respectively). Horizontal bars represent median values. Horizontal bars represent the median value

Figure 5 highlights the differences in the measurements of GPP models according to land cover type and seasons. The winter is the only season when CF has the highest GPP value. The summer and fall demonstrate that DF records the highest productivity, while CL is the intermediary land cover type.

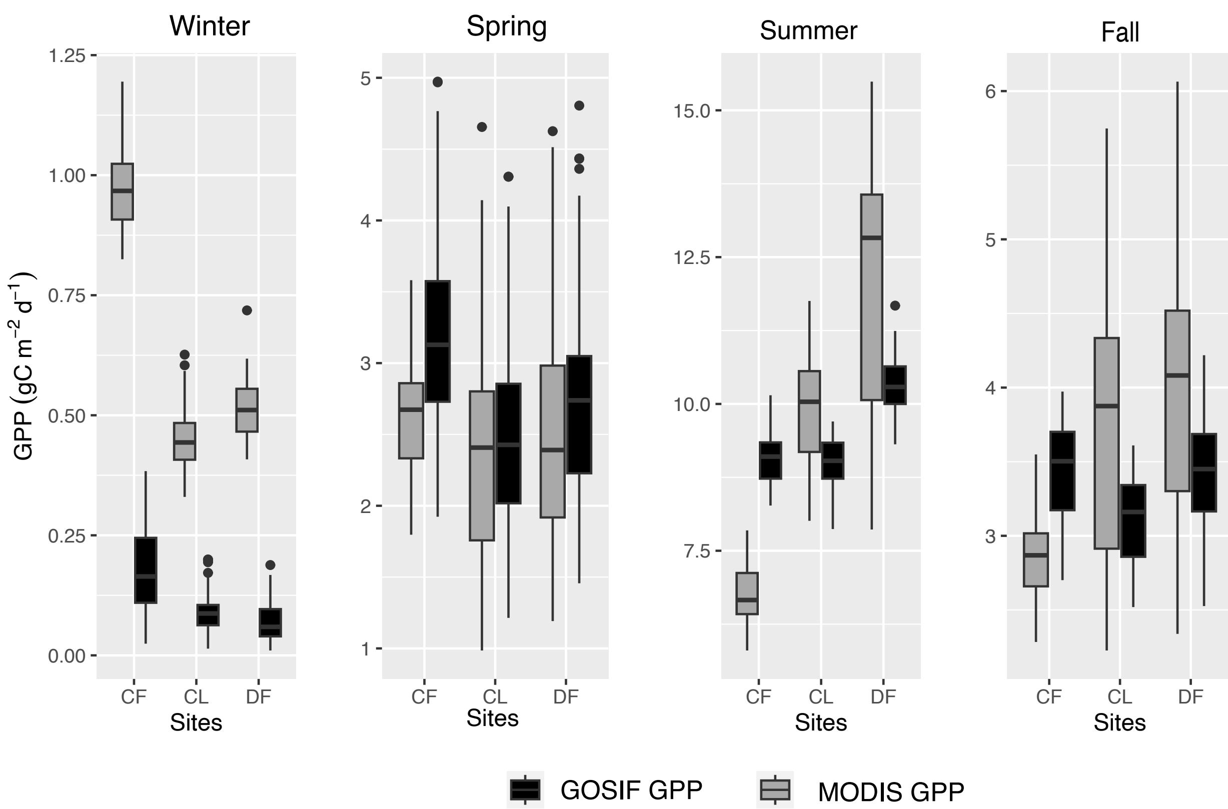

Figure 5. 20-year seasonal average GPP for the three land cover types.

The weighted GPP values (multiplied by the land cover proportions) show the contribution of each of the land cover types to the total GPP from the nine combined sites. (Table 9). GPP_{GOSIF} reveals that coniferous forests, croplands, and deciduous forests sequester 1.83 $gCm^{-2}d^{-1}$, 0.67 $gCm^{-2}d^{-1}$, and 0.67 $gCm^{-2}d^{-1,}$ respectively. GPP_{MODIS} reveals that coniferous forests, croplands, and deciduous forests sequester 2.22 $gCm^{-2}d^{-1}$, 0.60 $gCm^{-2}d^{-1}$, and 0.58 $gCm^{-2}d^{-1}$ respectively on average over the past two decades (Table 9).

Table 9. 20-year weighted annual GPP means from both models weighted according to land coverage proportion.

Land Cover Type	GPP_{GOSIF} Estimate (gCm^{-2}-d^{-1})	GPP_{MODIS} Estimate (gCm^{-2}-d^{-1})	Total Land Area Covered (Proportion)	GPP_{GOSIF} Weighted Value	GPP_{MODIS} Weighted Value
CF	3.32	4.03	0.55	**1.83**	**2.22**
CL	4.17	3.74	0.16	**0.67**	**0.60**
DF	4.84	4.21	0.14	**0.67**	**0.58**

4.2 Trends

4.2.1 Climatic variable trends

There were no significant trends in the five environmental variables on an annual basis. In summer, there were significant decreasing trends ($p < 0.05$) in temperature and vapor pressure deficit in zones 1, 2, and 3 (Figures 7 and 9, respectively). Winter solar radiation decreased in the same three zones (Figure 8). The alternate hypothesis was only accepted in the instances presented above in the significant trends. The null hypothesis was accepted in all other instances in relation to the MK tests for climatic trends. The entirety of the results for the MK trend and Sen slope tests are presented in Figures 6 to 10.

a)

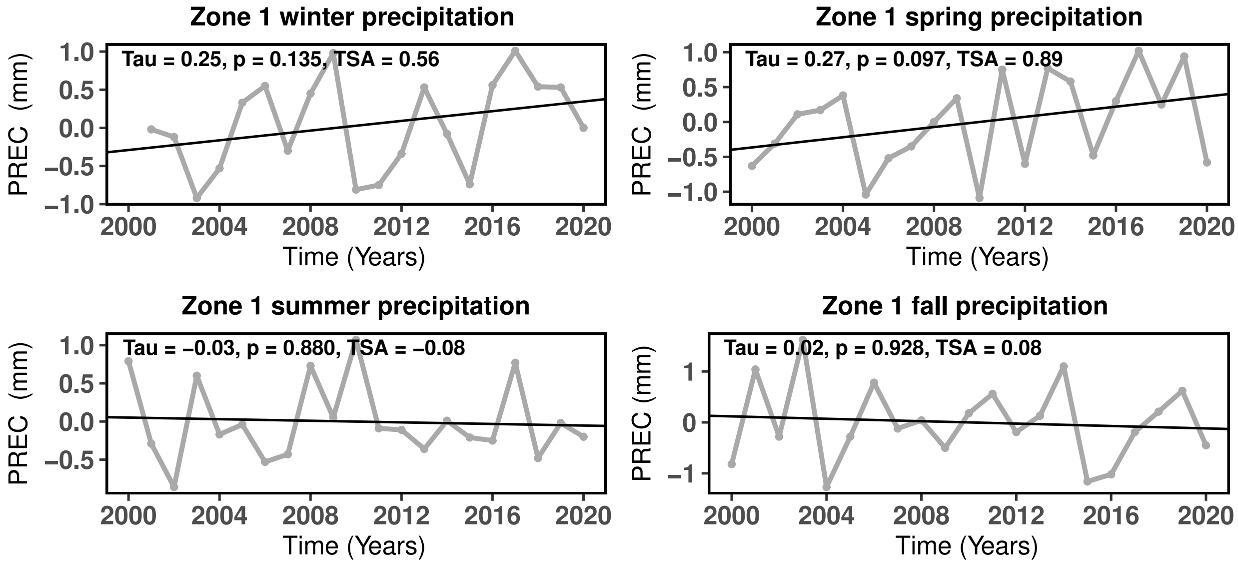
Zone 1 winter precipitation
Tau = 0.25, p = 0.135, TSA = 0.56
Zone 1 spring precipitation
Tau = 0.27, p = 0.097, TSA = 0.89
Zone 1 summer precipitation
Tau = −0.03, p = 0.880, TSA = −0.08
Zone 1 fall precipitation
Tau = 0.02, p = 0.928, TSA = 0.08
PREC (mm)
Time (Years)
2000
2004
2008
2012
2016
2020

b)

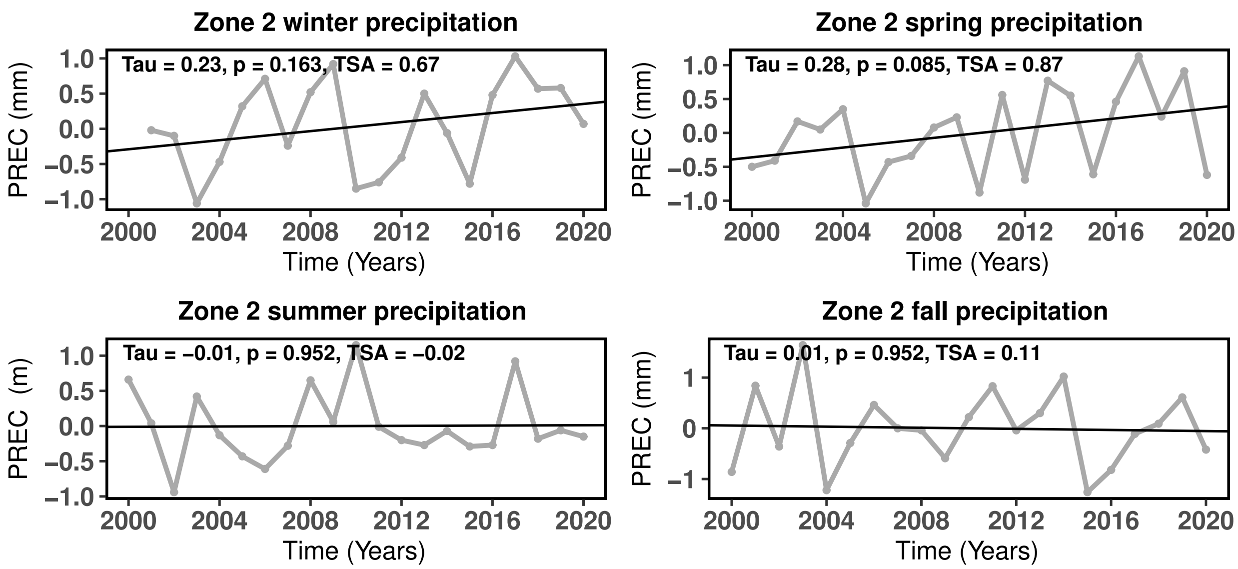
Zone 2 winter precipitation
Tau = 0.23, p = 0.163, TSA = 0.67
Zone 2 spring precipitation
Tau = 0.28, p = 0.085, TSA = 0.87
Zone 2 summer precipitation
Tau = −0.01, p = 0.952, TSA = −0.02
PREC (m)
Zone 2 fall precipitation
Tau = 0.01, p = 0.952, TSA = 0.11
PREC (mm)
Time (Years)
2000
2004
2008
2012
2016
2020

c)

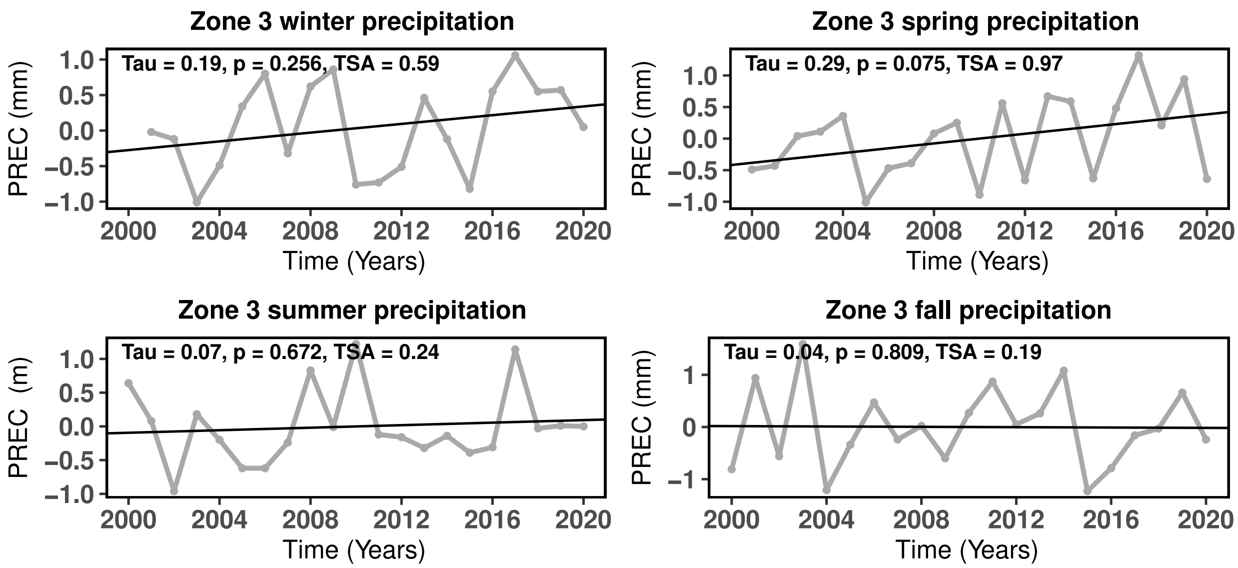
Zone 3 winter precipitation
Tau = 0.19, p = 0.256, TSA = 0.59
Zone 3 spring precipitation
Tau = 0.29, p = 0.075, TSA = 0.97
Zone 3 summer precipitation
Tau = 0.07, p = 0.672, TSA = 0.24
Zone 3 fall precipitation
Tau = 0.04, p = 0.809, TSA = 0.19
PREC (mm)
PREC (m)
Time (Years)

d)

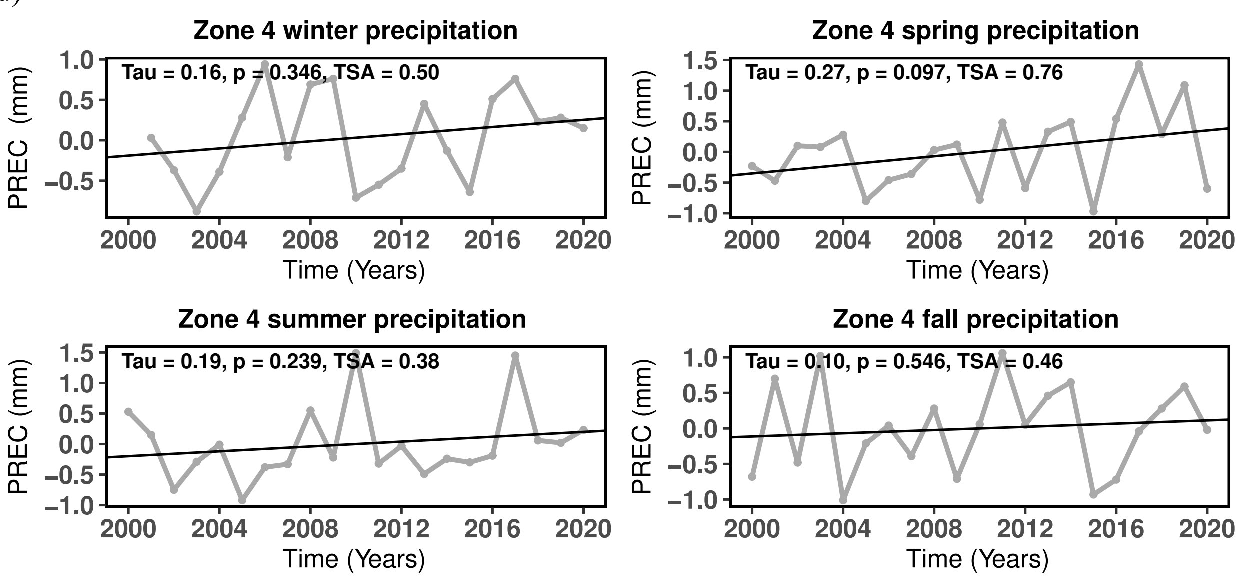
Zone 4 winter precipitation
Tau = 0.16, p = 0.346, TSA = 0.50
Zone 4 spring precipitation
Tau = 0.27, p = 0.097, TSA = 0.76
Zone 4 summer precipitation
Tau = 0.19, p = 0.239, TSA = 0.38
Zone 4 fall precipitation
Tau = 0.10, p = 0.546, TSA = 0.46
PREC (mm)
Time (Years)

e)

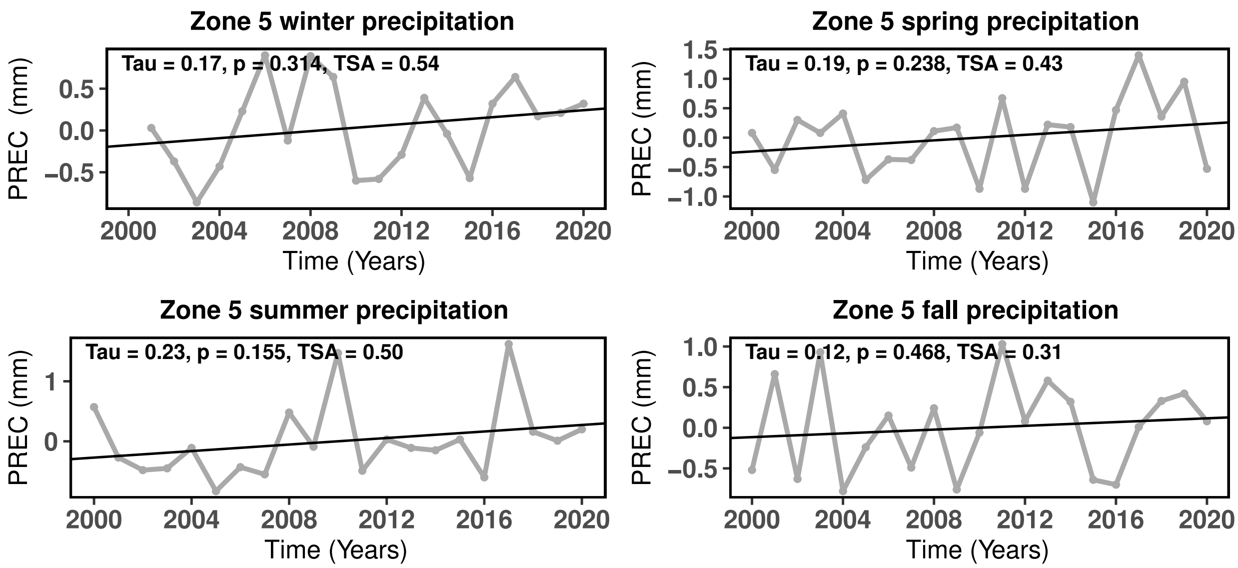

Figure 6. Trends in normalized seasonal precipitation (mm) at the five climatic zones.

a)

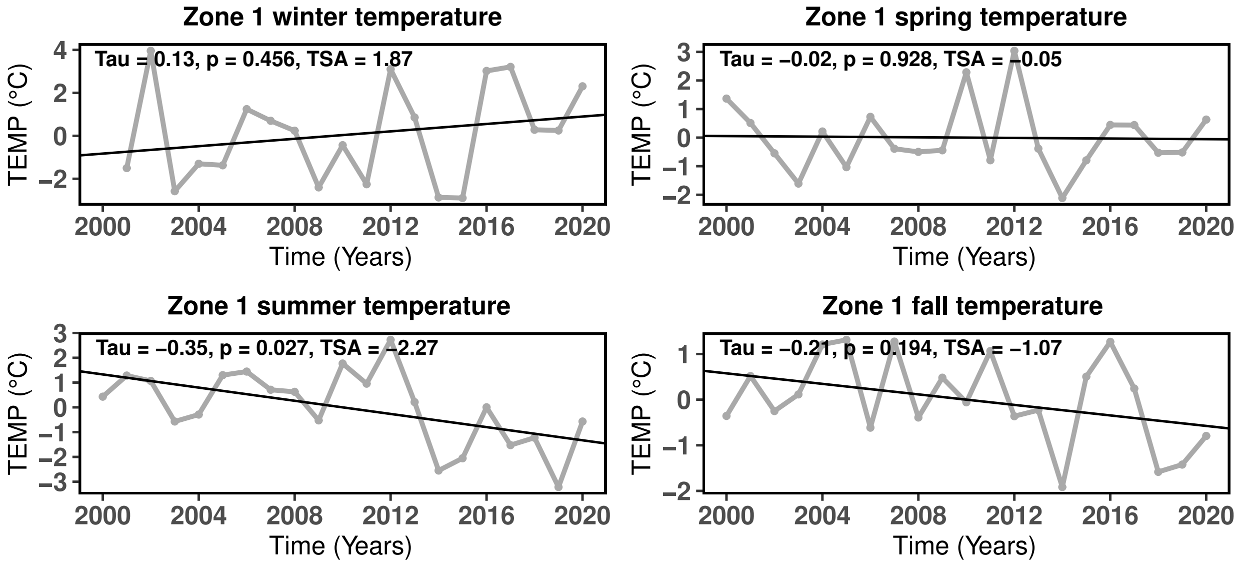
Zone 1 winter temperature
Tau = 0.13, p = 0.456, TSA = 1.87
Zone 1 spring temperature
Tau = −0.02, p = 0.928, TSA = −0.05
Zone 1 summer temperature
Tau = −0.35, p = 0.027, TSA = −2.27
Zone 1 fall temperature
Tau = −0.21, p = 0.194, TSA = −1.07
TEMP (°C)
Time (Years)

b)

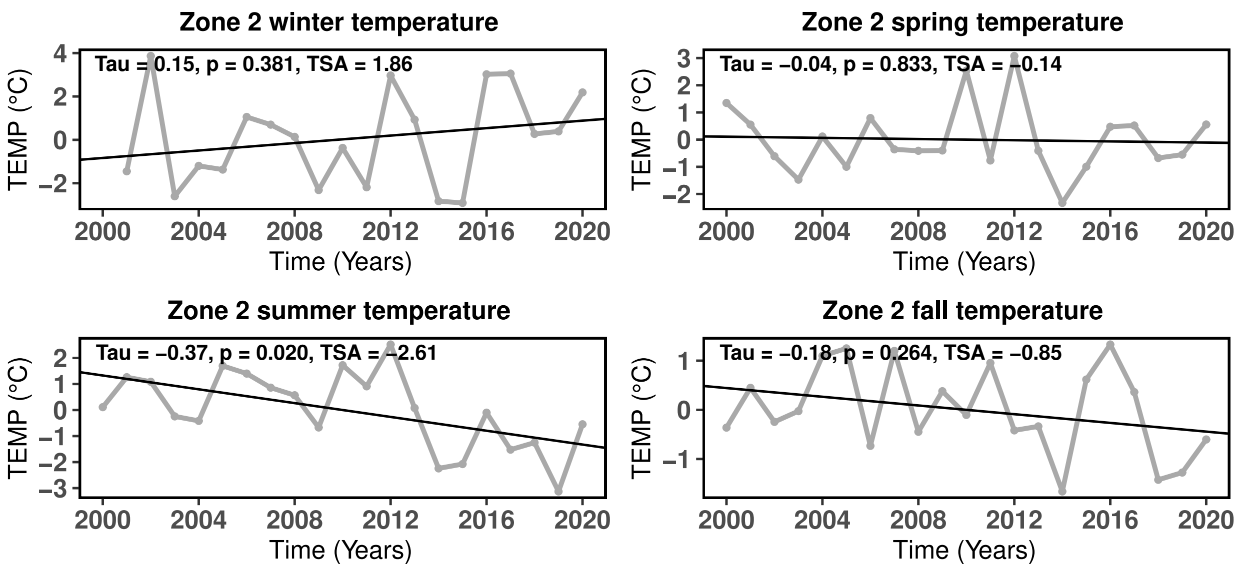
Zone 2 winter temperature
Tau = 0.15, p = 0.381, TSA = 1.86
Zone 2 spring temperature
Tau = −0.04, p = 0.833, TSA = −0.14
Zone 2 summer temperature
Tau = −0.37, p = 0.020, TSA = −2.61
Zone 2 fall temperature
Tau = −0.18, p = 0.264, TSA = −0.85
TEMP (°C)
Time (Years)

c)

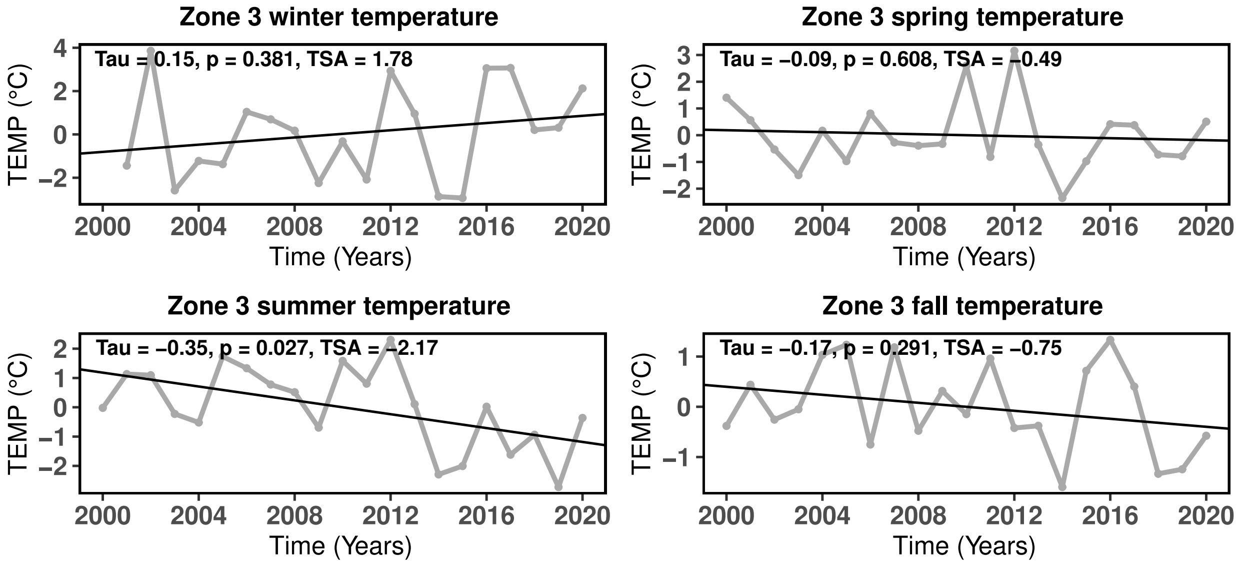
Zone 3 winter temperature
Tau = 0.15, p = 0.381, TSA = 1.78
Zone 3 spring temperature
Tau = −0.09, p = 0.608, TSA = −0.49
Zone 3 summer temperature
Tau = −0.35, p = 0.027, TSA = −2.17
Zone 3 fall temperature
Tau = −0.17, p = 0.291, TSA = −0.75
TEMP (°C)
Time (Years)
2000
2004
2008
2012
2016
2020

d)

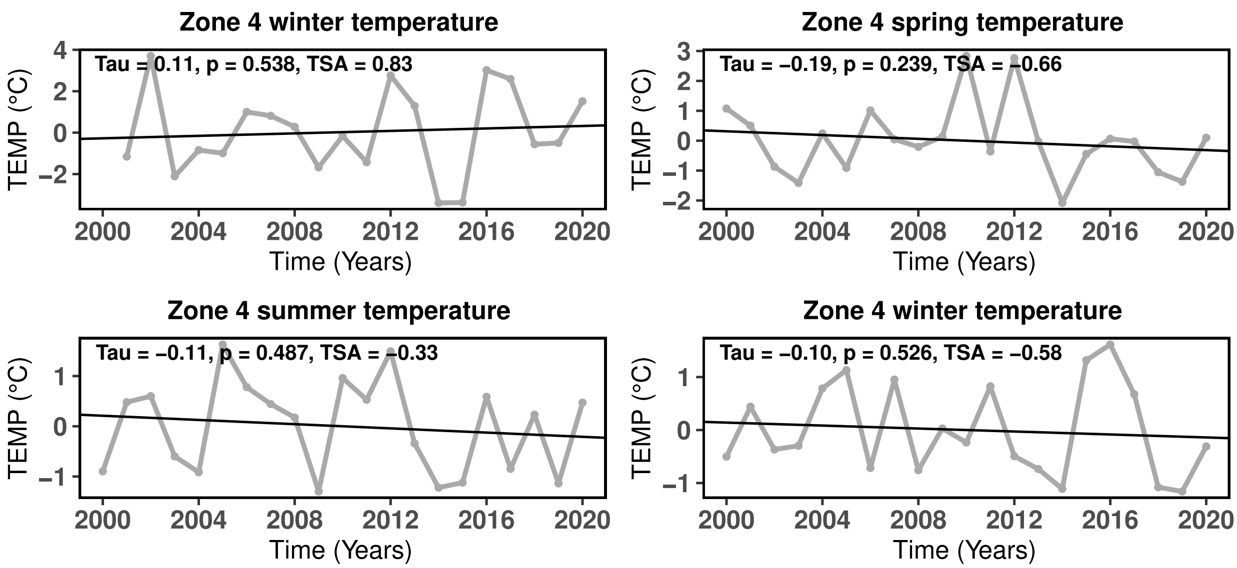
Zone 4 winter temperature
Tau = 0.11, p = 0.538, TSA = 0.83
Zone 4 spring temperature
Tau = −0.19, p = 0.239, TSA = −0.66
Zone 4 summer temperature
Tau = −0.11, p = 0.487, TSA = −0.33
Zone 4 winter temperature
Tau = −0.10, p = 0.526, TSA = −0.58
TEMP (°C)
Time (Years)
2000
2004
2008
2012
2016
2020

e)

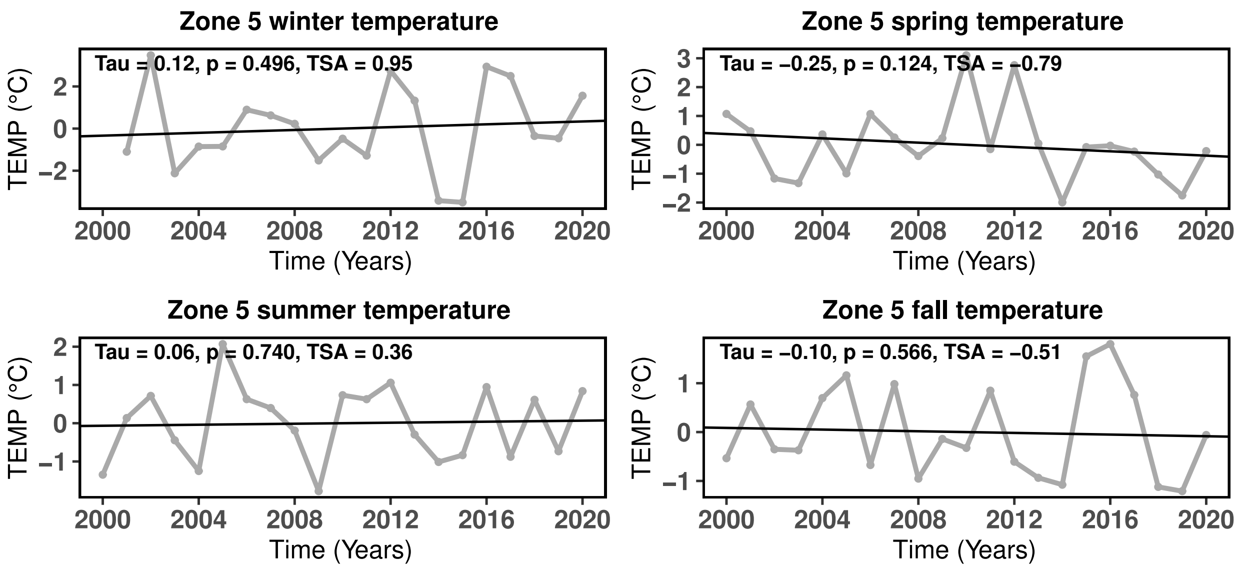

Figure 7. Trends in normalized seasonal air temperature (°C) at the five climatic zones.

a)

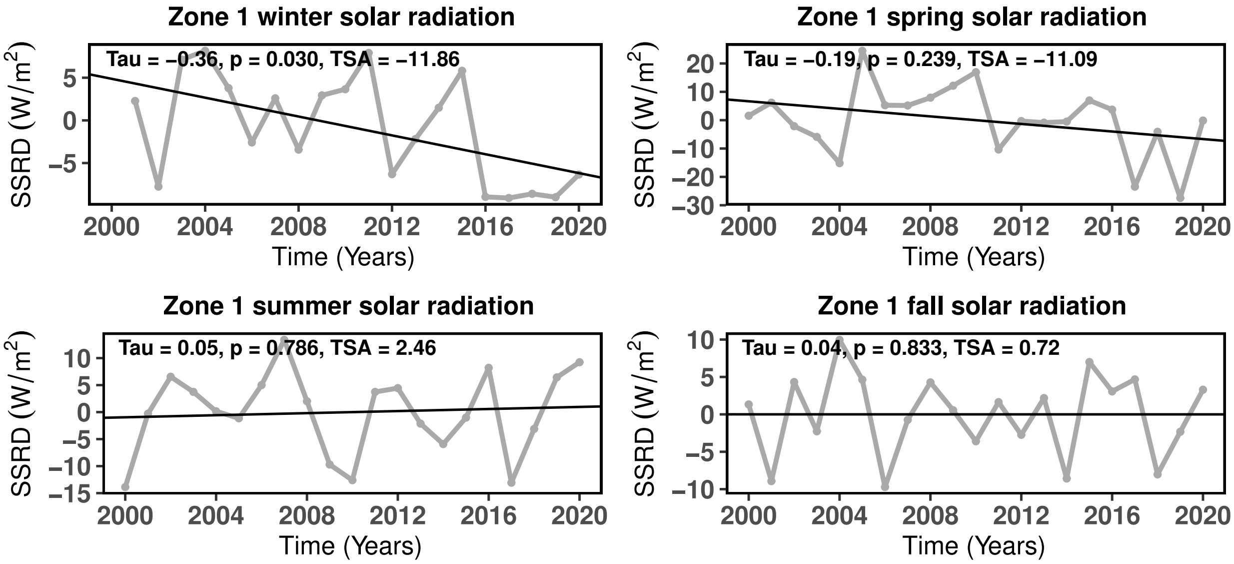
Zone 1 winter solar radiation
Tau = −0.36, p = 0.030, TSA = −11.86
Zone 1 spring solar radiation
Tau = −0.19, p = 0.239, TSA = −11.09
Zone 1 summer solar radiation
Tau = 0.05, p = 0.786, TSA = 2.46
Zone 1 fall solar radiation
Tau = 0.04, p = 0.833, TSA = 0.72
SSRD (W/m²)
Time (Years)

b)

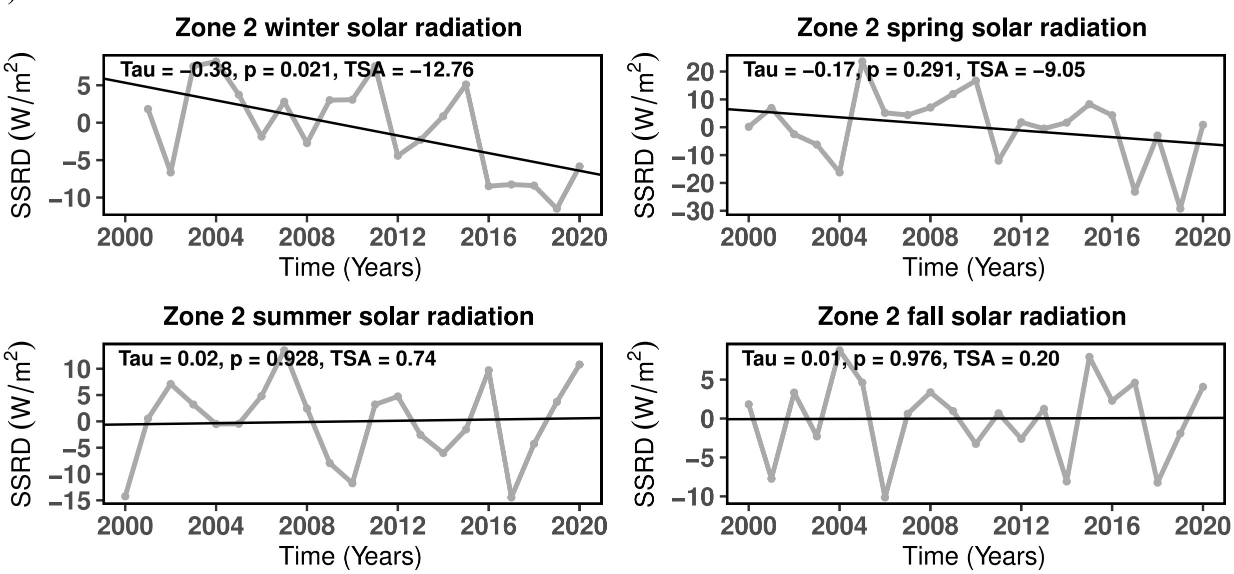
Zone 2 winter solar radiation
Tau = −0.38, p = 0.021, TSA = −12.76
Zone 2 spring solar radiation
Tau = −0.17, p = 0.291, TSA = −9.05
Zone 2 summer solar radiation
Tau = 0.02, p = 0.928, TSA = 0.74
Zone 2 fall solar radiation
Tau = 0.01, p = 0.976, TSA = 0.20
SSRD (W/m²)
Time (Years)

c)

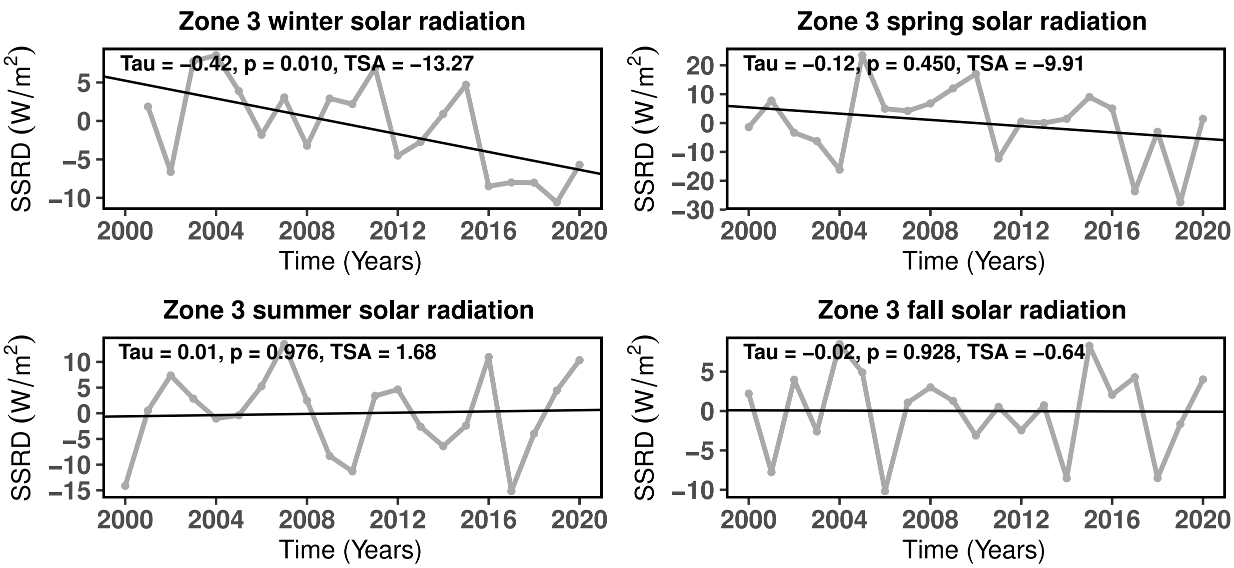
Zone 3 winter solar radiation
Tau = −0.42, p = 0.010, TSA = −13.27
Zone 3 spring solar radiation
Tau = −0.12, p = 0.450, TSA = −9.91
Zone 3 summer solar radiation
Tau = 0.01, p = 0.976, TSA = 1.68
Zone 3 fall solar radiation
Tau = −0.02, p = 0.928, TSA = −0.64
SSRD (W/m2)
Time (Years)

d)

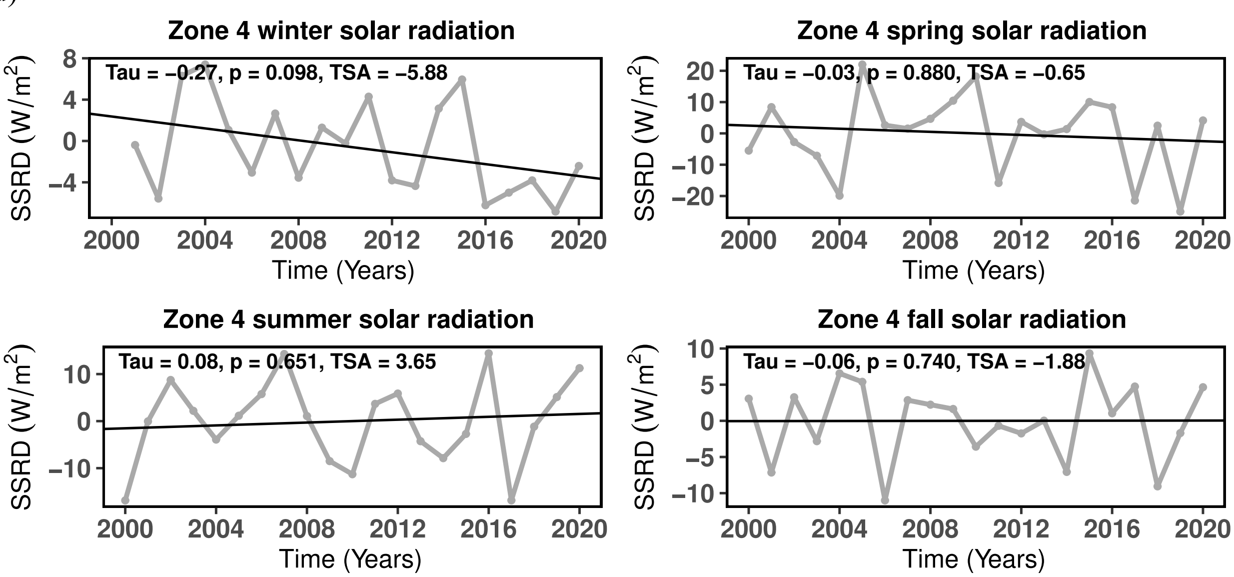
Zone 4 winter solar radiation
Tau = −0.27, p = 0.098, TSA = −5.88
Zone 4 spring solar radiation
Tau = −0.03, p = 0.880, TSA = −0.65
Zone 4 summer solar radiation
Tau = 0.08, p = 0.651, TSA = 3.65
Zone 4 fall solar radiation
Tau = −0.06, p = 0.740, TSA = −1.88
SSRD (W/m2)
Time (Years)

e)

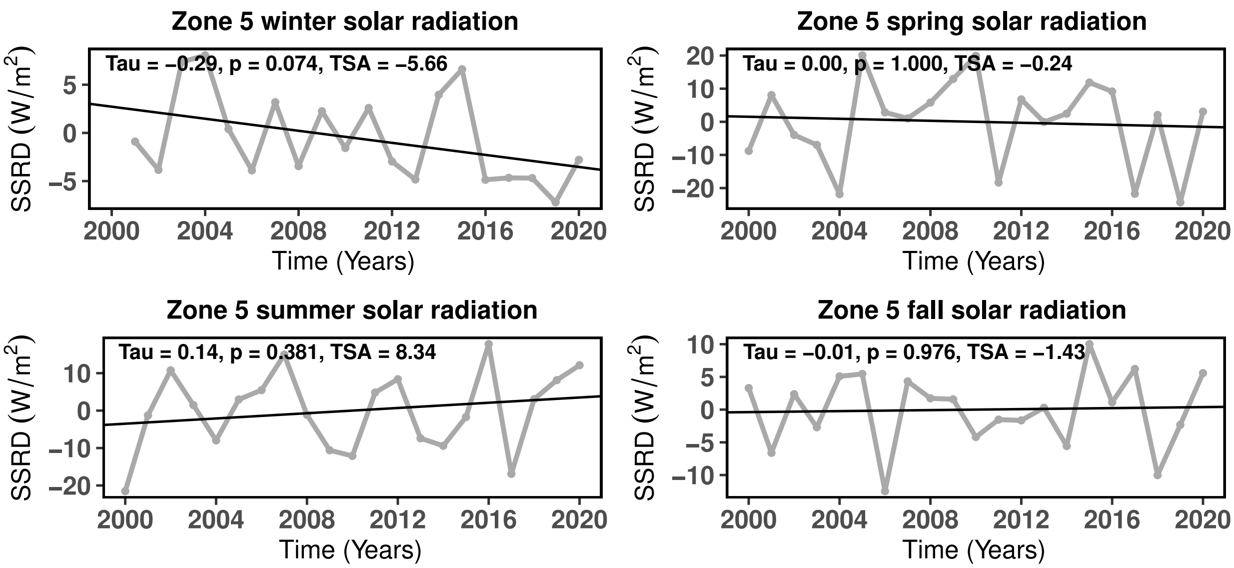

Figure 8. Trends in normalized seasonal solar radiation (Wm^{-2}) at the five climatic zones.

a)

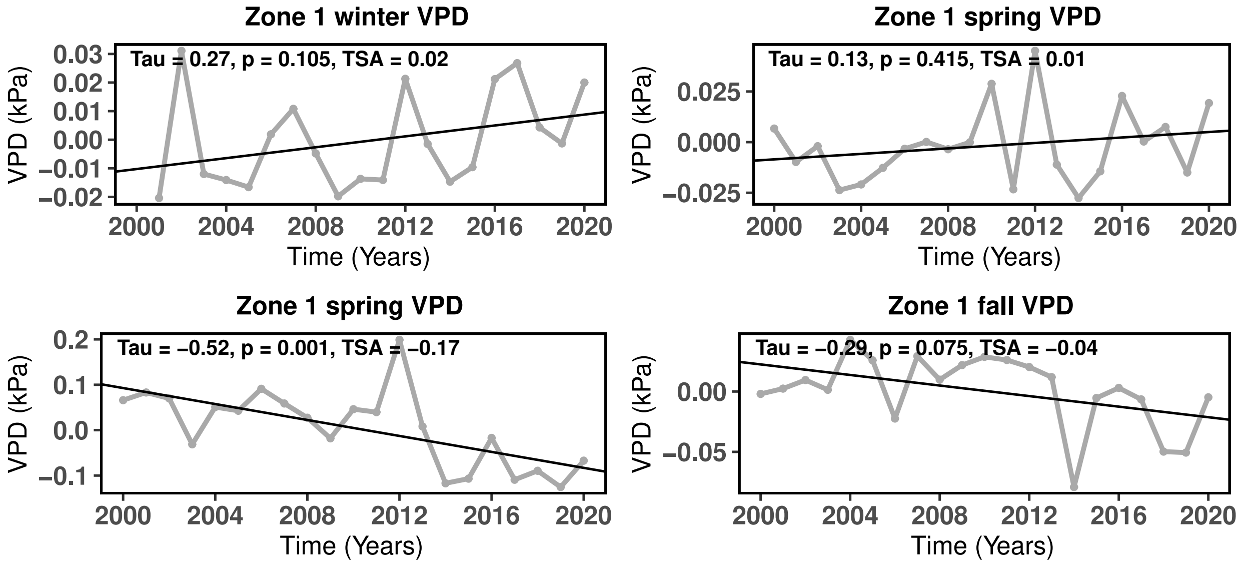
Zone 1 winter VPD
Tau = 0.27, p = 0.105, TSA = 0.02
Zone 1 spring VPD
Tau = 0.13, p = 0.415, TSA = 0.01
Zone 1 spring VPD
Tau = –0.52, p = 0.001, TSA = –0.17
Zone 1 fall VPD
Tau = –0.29, p = 0.075, TSA = –0.04
VPD (kPa)
Time (Years)

b)

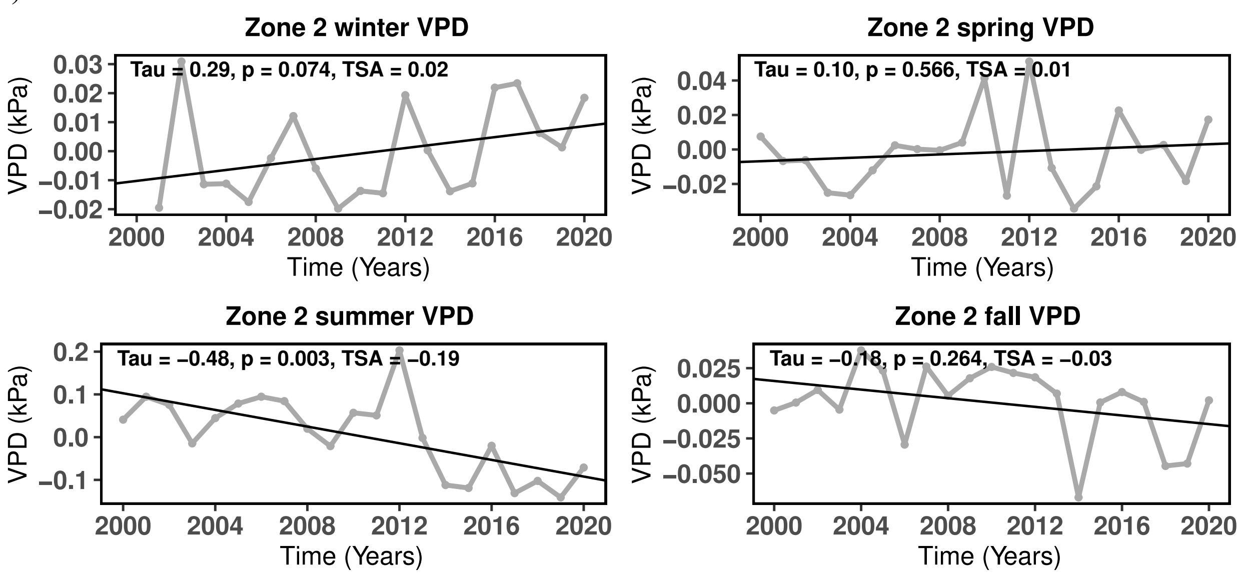
Zone 2 winter VPD
Tau = 0.29, p = 0.074, TSA = 0.02
Zone 2 spring VPD
Tau = 0.10, p = 0.566, TSA = 0.01
Zone 2 summer VPD
Tau = –0.48, p = 0.003, TSA = –0.19
Zone 2 fall VPD
Tau = –0.18, p = 0.264, TSA = –0.03
VPD (kPa)
Time (Years)

c)

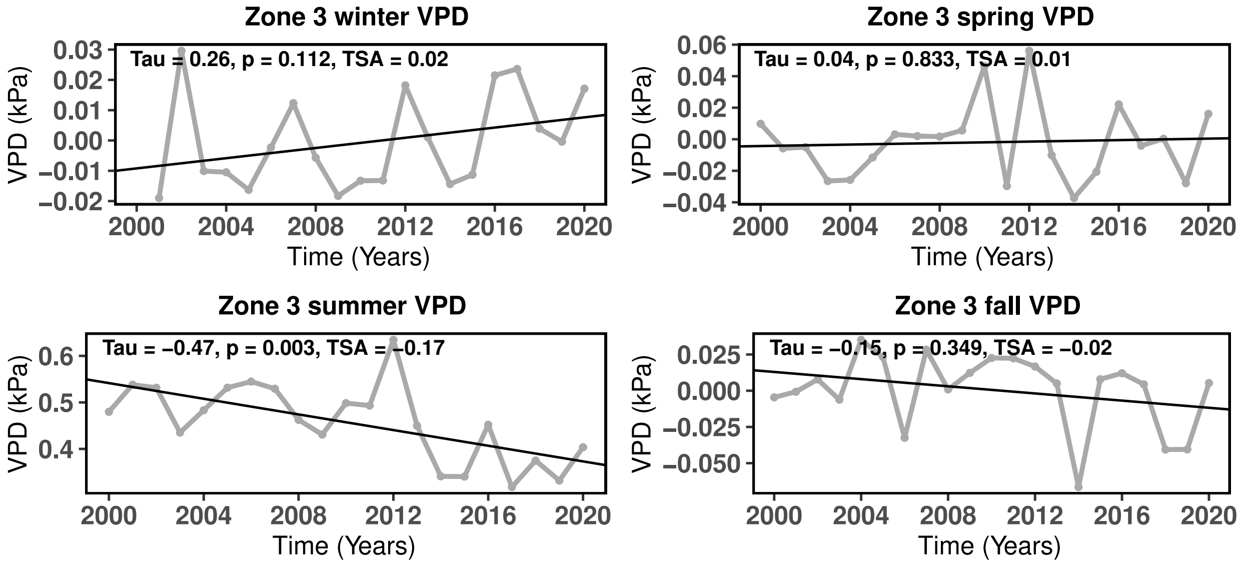

Zone 3 winter VPD
Tau = 0.26, p = 0.112, TSA = 0.02
VPD (kPa)
Time (Years)
Zone 3 spring VPD
Tau = 0.04, p = 0.833, TSA = 0.01
VPD (kPa)
Time (Years)
Zone 3 summer VPD
Tau = –0.47, p = 0.003, TSA = –0.17
VPD (kPa)
Time (Years)
Zone 3 fall VPD
Tau = –0.15, p = 0.349, TSA = –0.02
VPD (kPa)
Time (Years)

d)

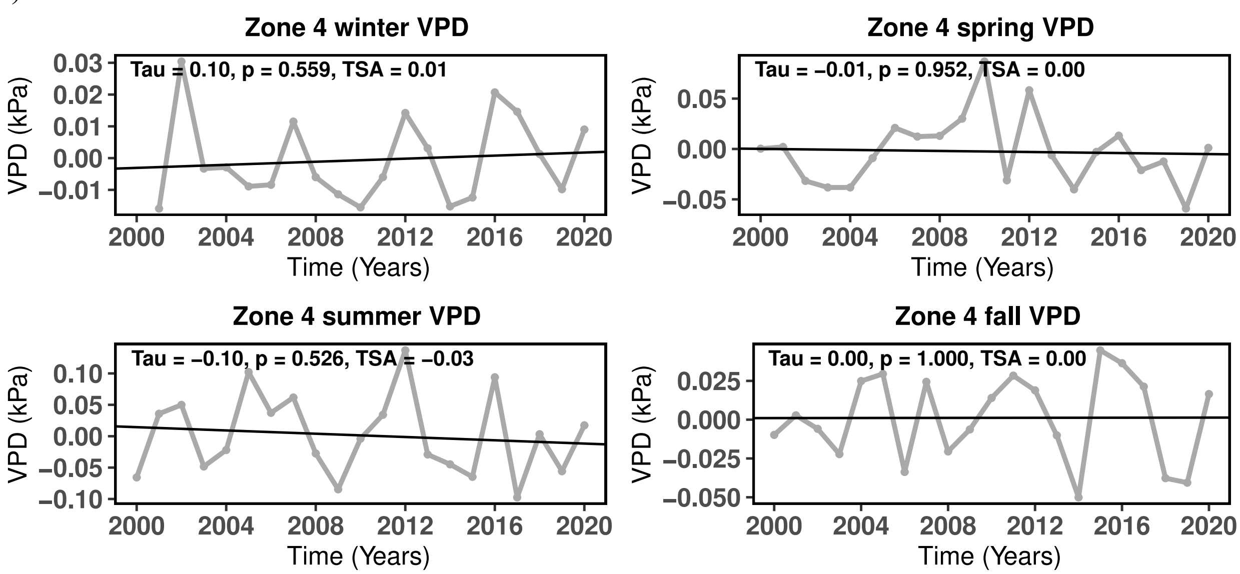

Zone 4 winter VPD
Tau = 0.10, p = 0.559, TSA = 0.01
VPD (kPa)
Time (Years)
Zone 4 spring VPD
Tau = –0.01, p = 0.952, TSA = 0.00
VPD (kPa)
Time (Years)
Zone 4 summer VPD
Tau = –0.10, p = 0.526, TSA = –0.03
VPD (kPa)
Time (Years)
Zone 4 fall VPD
Tau = 0.00, p = 1.000, TSA = 0.00
VPD (kPa)
Time (Years)

e)

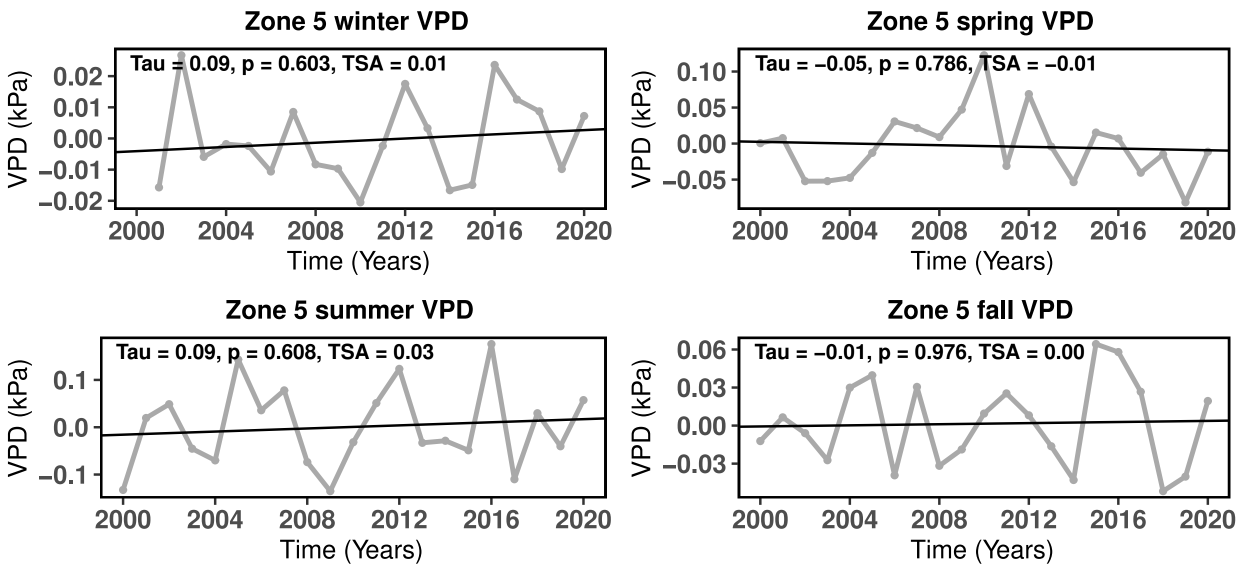

Figure 9. Trends in normalized seasonal vapor pressure deficit (kPa) at the five climatic zones.

a)

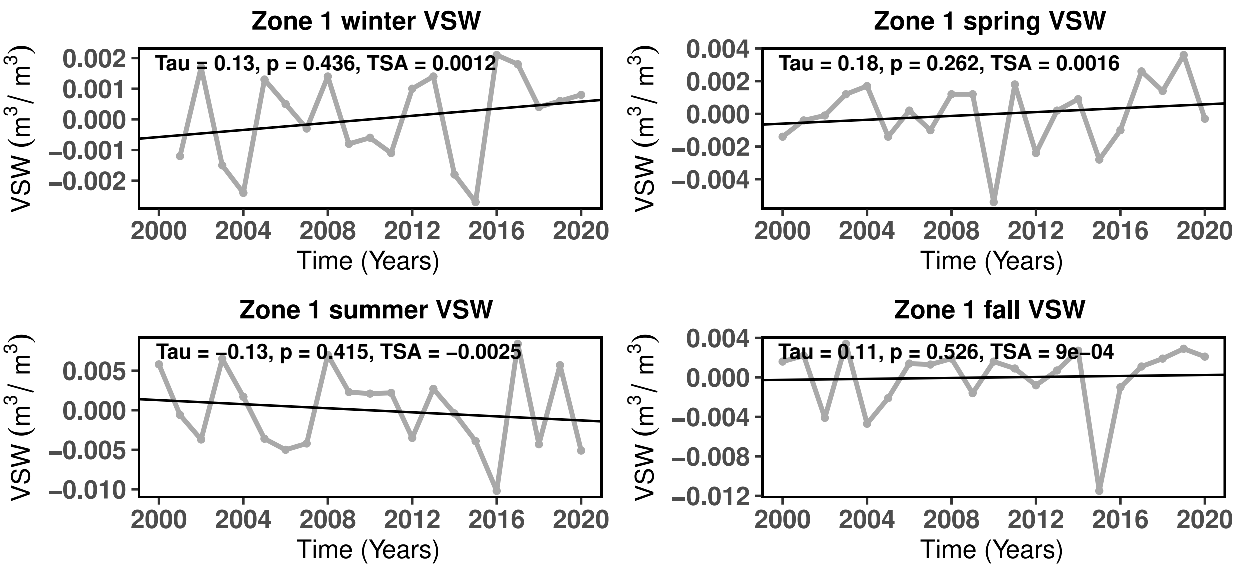
Zone 1 winter VSW
Tau = 0.13, p = 0.436, TSA = 0.0012
VSW (m3/ m3)
0.002
0.001
0.000
−0.001
−0.002
2000
2004
2008
2012
2016
2020
Time (Years)
Zone 1 spring VSW
Tau = 0.18, p = 0.262, TSA = 0.0016
0.004
0.002
0.000
−0.002
−0.004
Zone 1 summer VSW
Tau = −0.13, p = 0.415, TSA = −0.0025
0.005
0.000
−0.005
−0.010
Zone 1 fall VSW
Tau = 0.11, p = 0.526, TSA = 9e−04
0.004
0.000
−0.004
−0.008
−0.012

b)

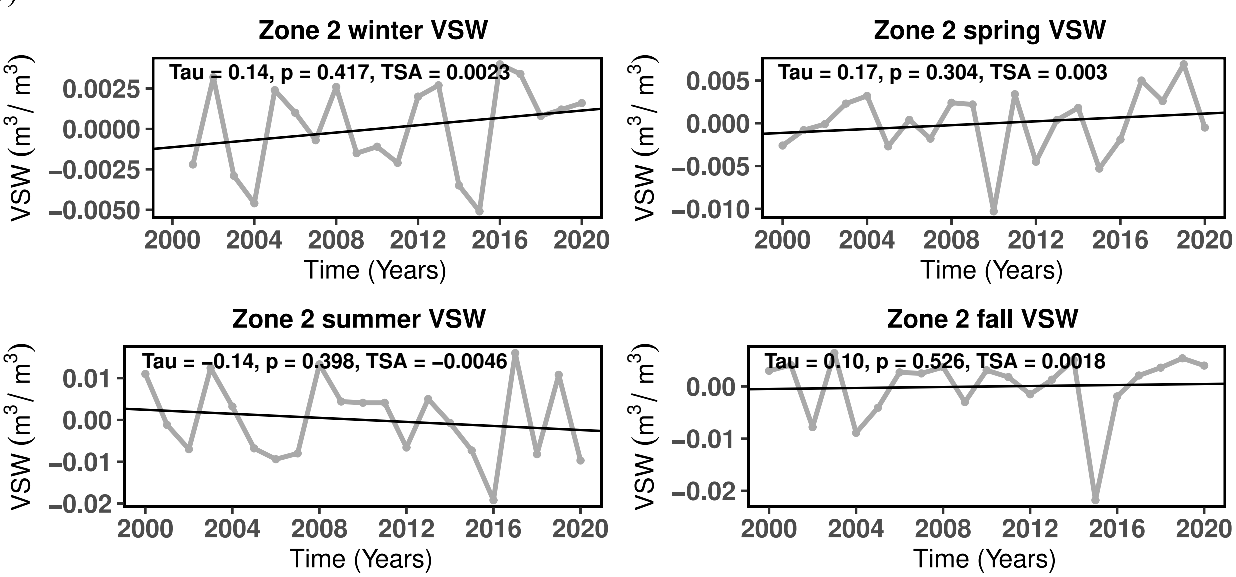
Zone 2 winter VSW
Tau = 0.14, p = 0.417, TSA = 0.0023
VSW (m3/ m3)
0.0025
0.0000
−0.0025
−0.0050
2000
2004
2008
2012
2016
2020
Time (Years)
Zone 2 spring VSW
Tau = 0.17, p = 0.304, TSA = 0.003
0.005
0.000
−0.005
−0.010
Zone 2 summer VSW
Tau = −0.14, p = 0.398, TSA = −0.0046
0.01
0.00
−0.01
−0.02
Zone 2 fall VSW
Tau = 0.10, p = 0.526, TSA = 0.0018
0.00
−0.01
−0.02

c)

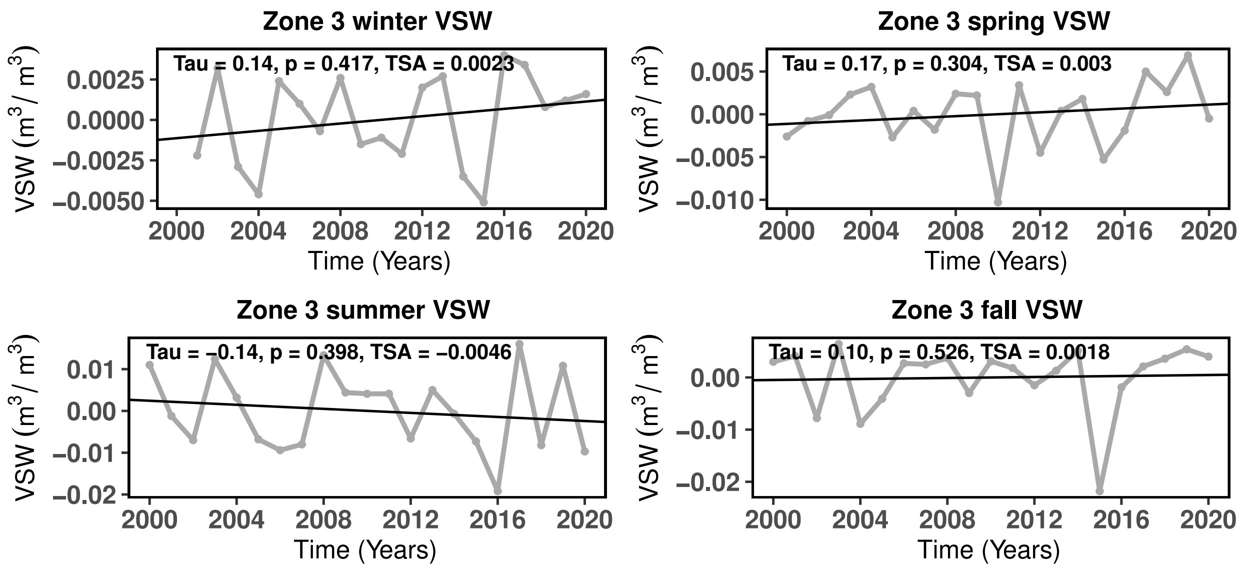
Zone 3 winter VSW
Tau = 0.14, p = 0.417, TSA = 0.0023
Zone 3 spring VSW
Tau = 0.17, p = 0.304, TSA = 0.003
Zone 3 summer VSW
Tau = –0.14, p = 0.398, TSA = –0.0046
Zone 3 fall VSW
Tau = 0.10, p = 0.526, TSA = 0.0018
VSW (m3/ m3)
Time (Years)

d)

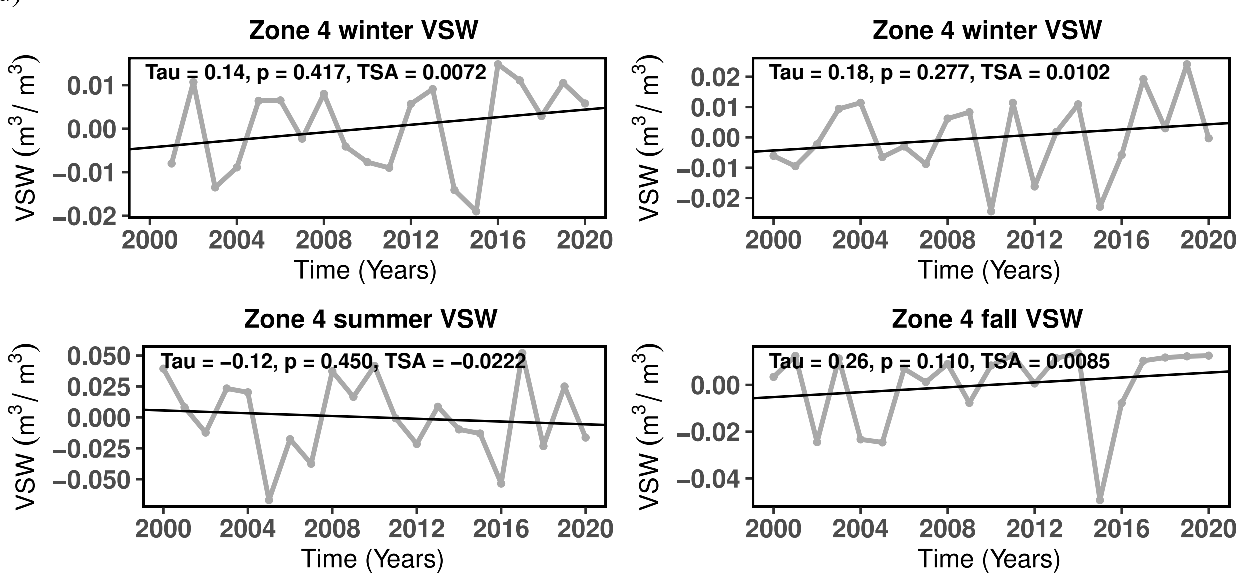
Zone 4 winter VSW
Tau = 0.14, p = 0.417, TSA = 0.0072
Zone 4 winter VSW
Tau = 0.18, p = 0.277, TSA = 0.0102
Zone 4 summer VSW
Tau = –0.12, p = 0.450, TSA = –0.0222
Zone 4 fall VSW
Tau = 0.26, p = 0.110, TSA = 0.0085
VSW (m3/ m3)
Time (Years)

e)

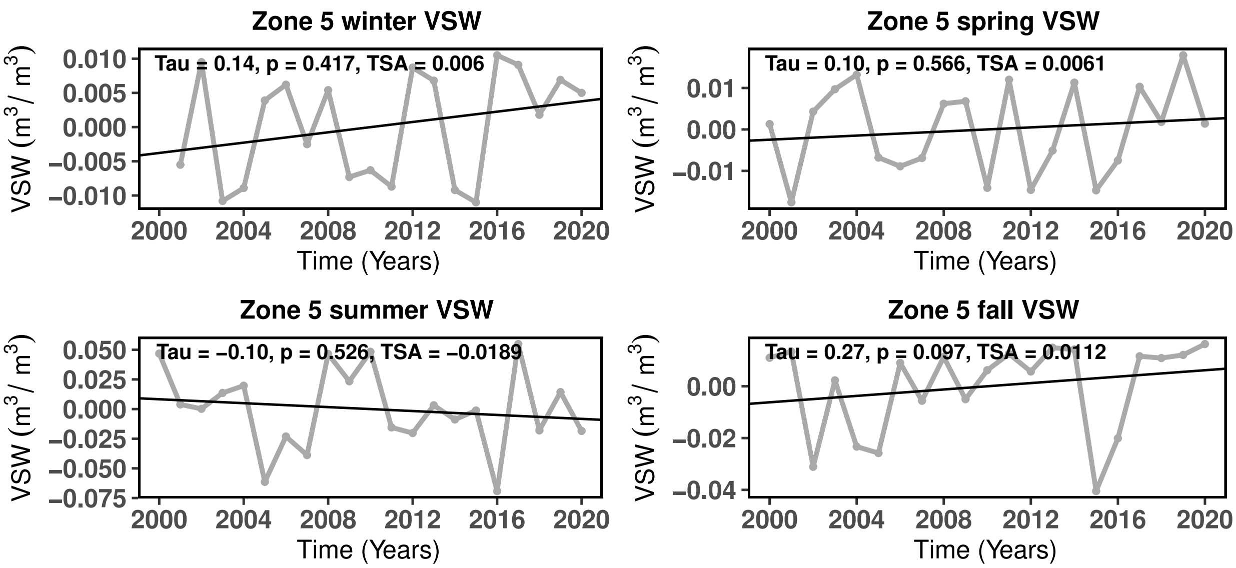

Figure 10. Trends in normalized seasonal volumetric soil water (m^3/m^3) at the five climatic zones.

4.2.2 GPP trends

There were no statistically significant trends in GPP over the past 20 years at any site, during any season, for either model (Figure 11). The null hypotheses were therefore accepted since the MK test didn't meet the statistical significance conditions ($p < 0.05$). Although the slopes were not statistically significant in most cases, the sign of the trend lines for the two models was the same. In terms of interannual variability, positive and negative deviations in both models generally coincided. Occasionally, a positive deviation in one model corresponded to a negative deviation in another model, or a large deviation in one model corresponded to a negligible deviation in the other.

a)

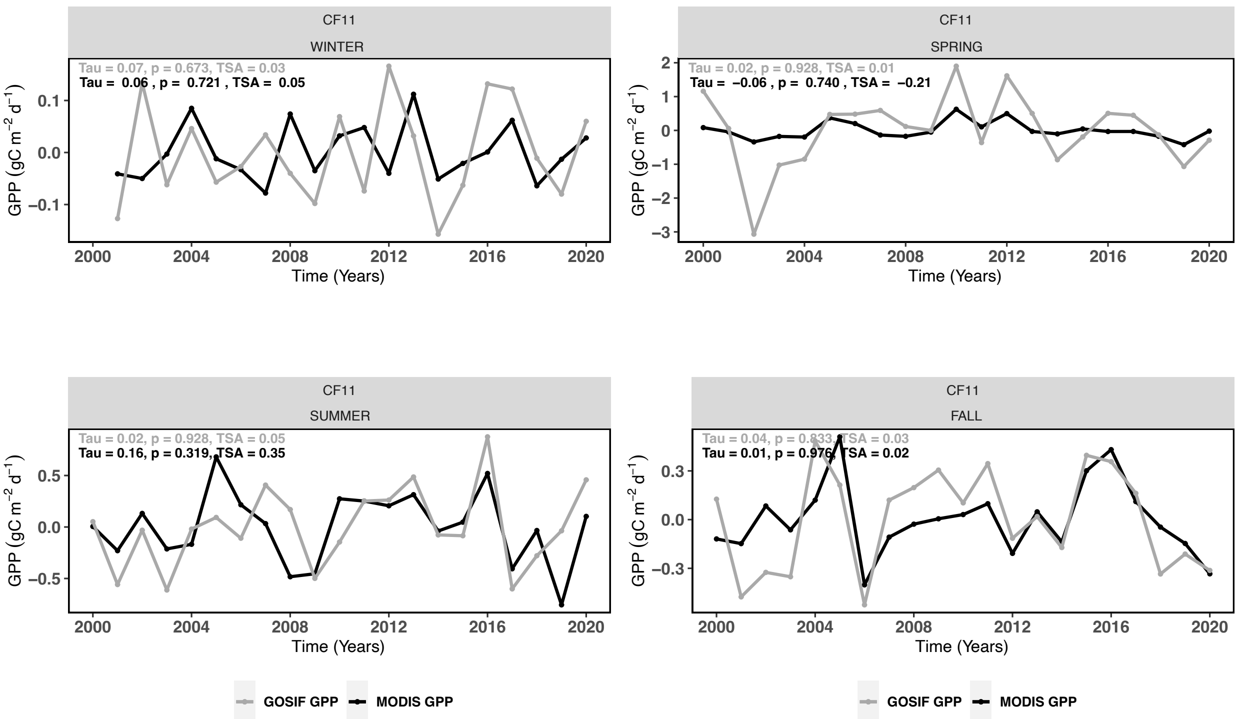

CF11
WINTER
Tau = 0.07, p = 0.673, TSA = 0.03
Tau = 0.06 , p = 0.721 , TSA = 0.05
GPP (gC m^{-2} d^{-1})
Time (Years)
CF11
SPRING
Tau = 0.02, p = 0.928, TSA = 0.01
Tau = −0.06 , p = 0.740 , TSA = −0.21
CF11
SUMMER
Tau = 0.02, p = 0.928, TSA = 0.05
Tau = 0.16, p = 0.319, TSA = 0.35
CF11
FALL
Tau = 0.04, p = 0.833, TSA = 0.03
Tau = 0.01, p = 0.976, TSA = 0.02
GOSIF GPP
MODIS GPP

b)

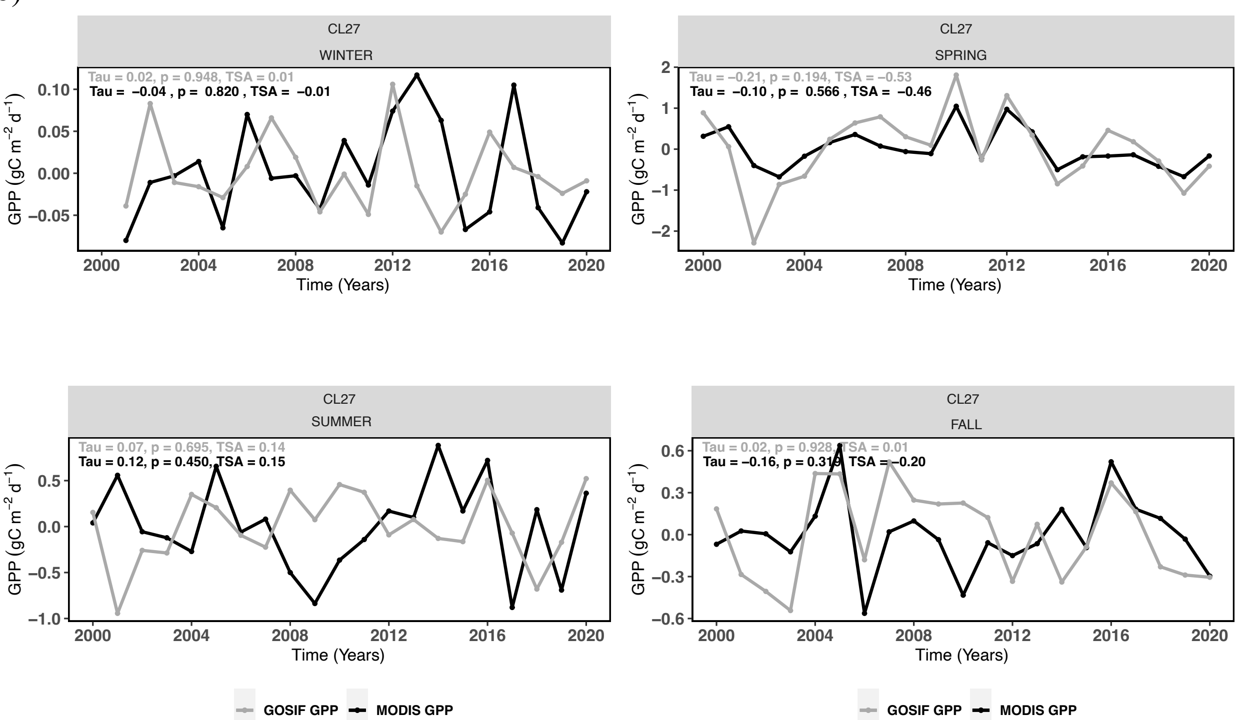

CL27
WINTER
Tau = 0.02, p = 0.948, TSA = 0.01
Tau = −0.04 , p = 0.820 , TSA = −0.01
GPP (gC m^{-2} d^{-1})
Time (Years)
CL27
SPRING
Tau = −0.21, p = 0.194, TSA = −0.53
Tau = −0.10 , p = 0.566 , TSA = −0.46
CL27
SUMMER
Tau = 0.07, p = 0.695, TSA = 0.14
Tau = 0.12, p = 0.450, TSA = 0.15
CL27
FALL
Tau = 0.02, p = 0.928, TSA = 0.01
Tau = −0.16, p = 0.319, TSA = −0.20
GOSIF GPP
MODIS GPP

c)

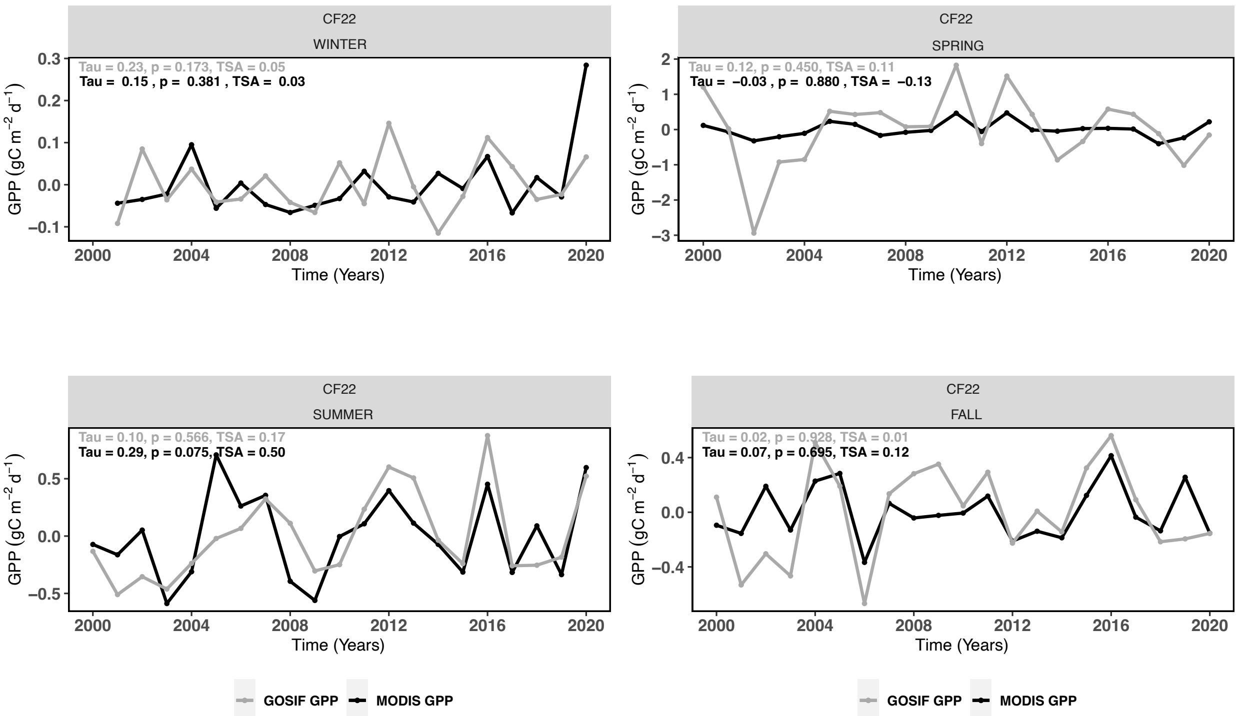
CF22
WINTER
Tau = 0.23, p = 0.173, TSA = 0.05
Tau = 0.15 , p = 0.381 , TSA = 0.03
CF22
SPRING
Tau = 0.12, p = 0.450, TSA = 0.11
Tau = −0.03 , p = 0.880 , TSA = −0.13
CF22
SUMMER
Tau = 0.10, p = 0.566, TSA = 0.17
Tau = 0.29, p = 0.075, TSA = 0.50
CF22
FALL
Tau = 0.02, p = 0.928, TSA = 0.01
Tau = 0.07, p = 0.695, TSA = 0.12
GPP (gC m−2 d−1)
Time (Years)
GOSIF GPP
MODIS GPP

d)

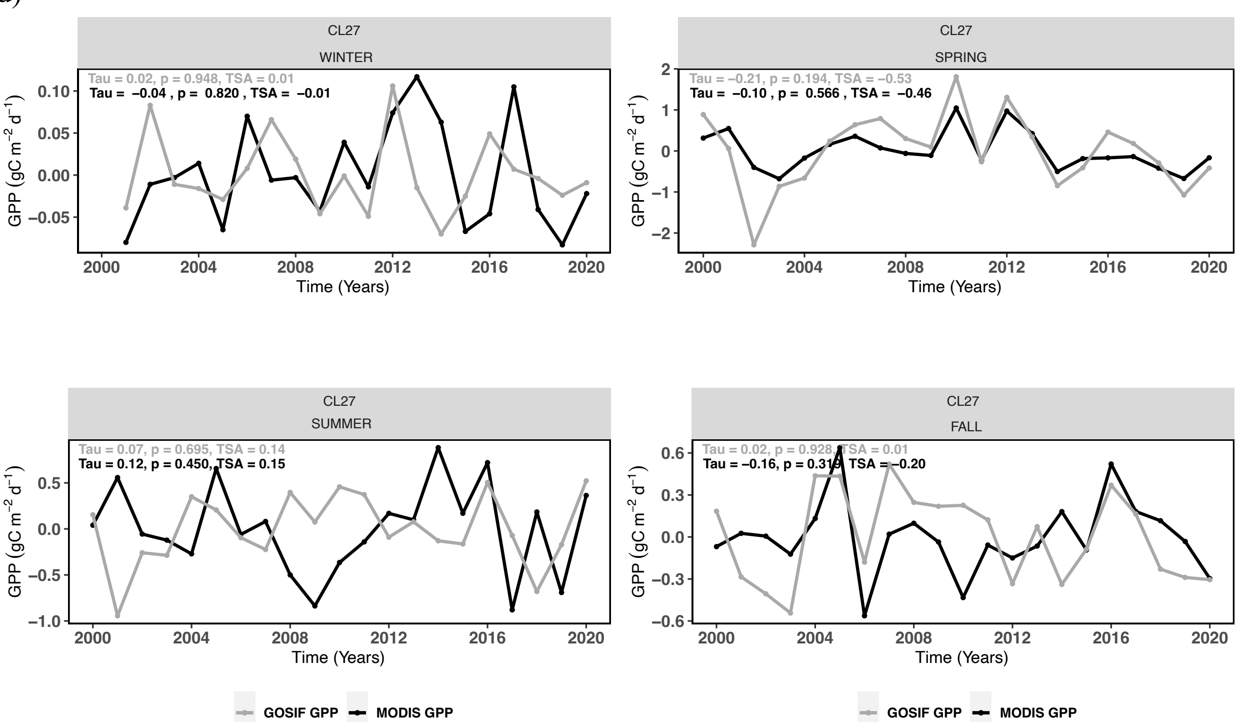
CL27
WINTER
Tau = 0.02, p = 0.948, TSA = 0.01
Tau = −0.04 , p = 0.820 , TSA = −0.01
CL27
SPRING
Tau = −0.21, p = 0.194, TSA = −0.53
Tau = −0.10 , p = 0.566 , TSA = −0.46
CL27
SUMMER
Tau = 0.07, p = 0.695, TSA = 0.14
Tau = 0.12, p = 0.450, TSA = 0.15
CL27
FALL
Tau = 0.02, p = 0.928, TSA = 0.01
Tau = −0.16, p = 0.319, TSA = −0.20
GPP (gC m−2 d−1)
Time (Years)
GOSIF GPP
MODIS GPP

e)

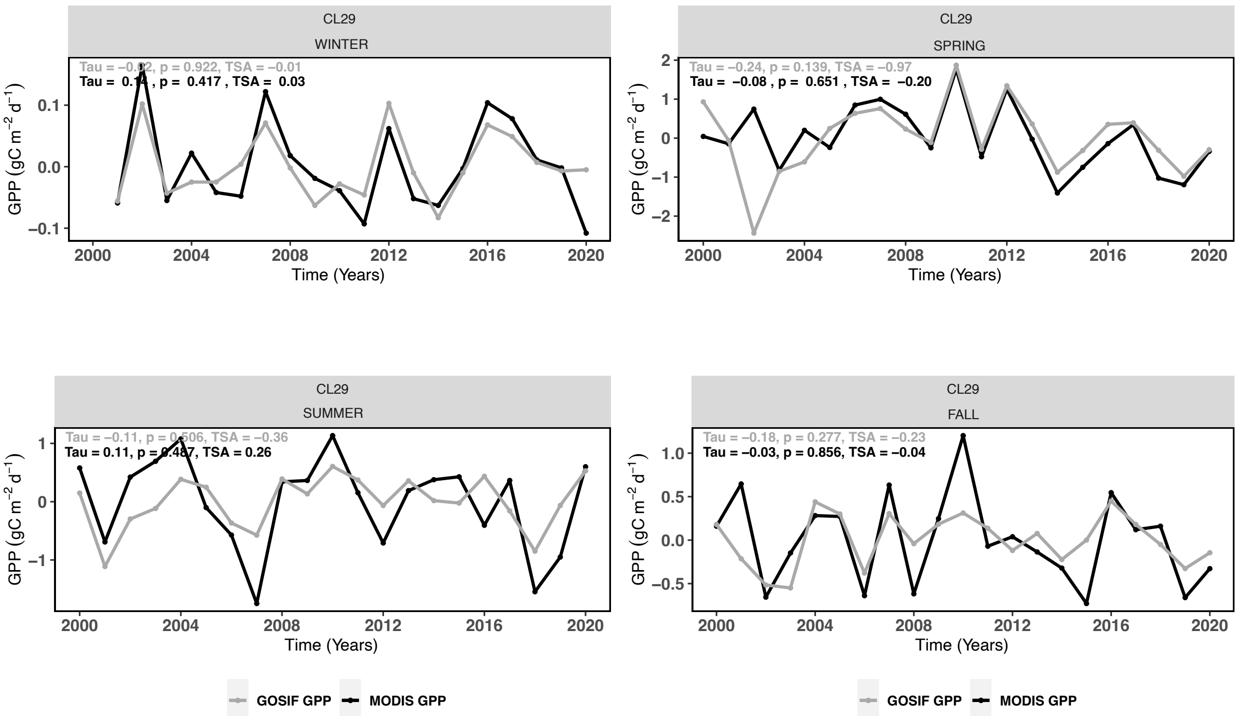

CL29
WINTER
CL29
SPRING
Tau = −0.24, p = 0.139, TSA = −0.97
Tau = −0.08 , p = 0.651 , TSA = −0.20
CL29
SUMMER
CL29
FALL
Tau = −0.18, p = 0.277, TSA = −0.23
Tau = −0.03, p = 0.856, TSA = −0.04
GPP (gC m−2 d−1)
Time (Years)
GOSIF GPP
MODIS GPP

f)

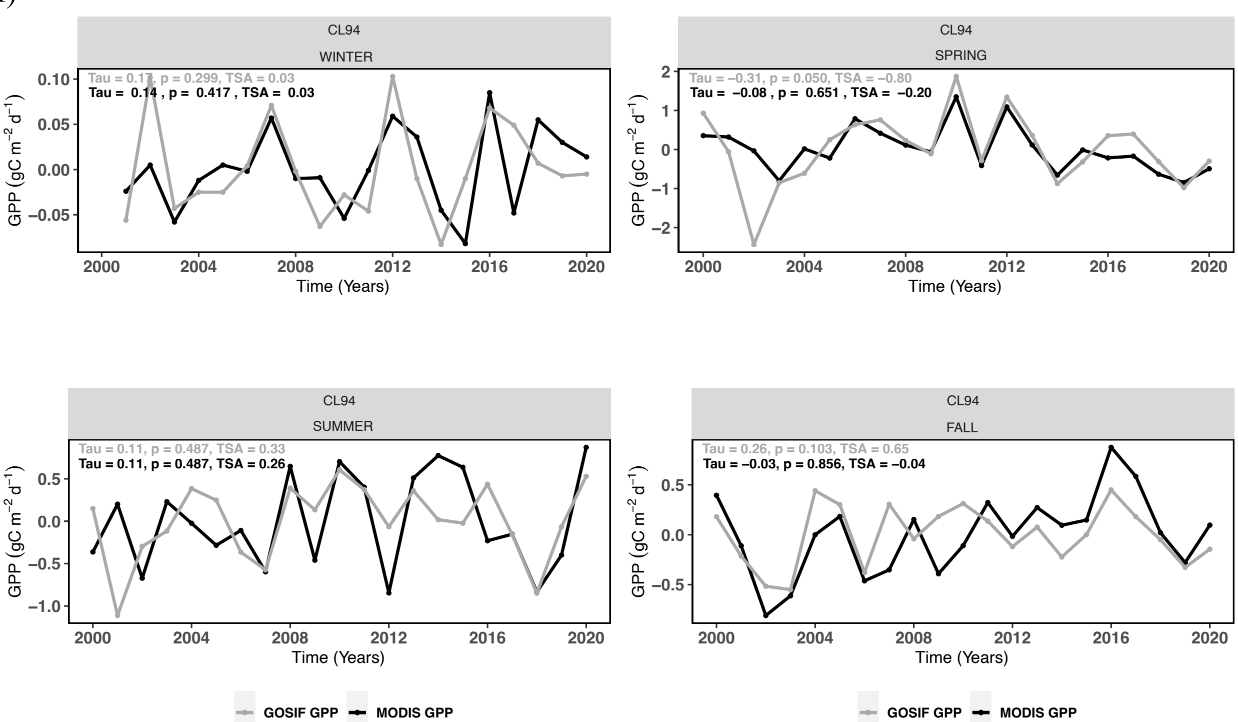

CL94
WINTER
CL94
SPRING
Tau = −0.31, p = 0.050, TSA = −0.80
Tau = −0.08 , p = 0.651 , TSA = −0.20
CL94
SUMMER
Tau = 0.11, p = 0.487, TSA = 0.33
Tau = 0.11, p = 0.487, TSA = 0.26
CL94
FALL
Tau = 0.26, p = 0.103, TSA = 0.65
Tau = −0.03, p = 0.856, TSA = −0.04
GPP (gC m−2 d−1)
Time (Years)
GOSIF GPP
MODIS GPP

g)

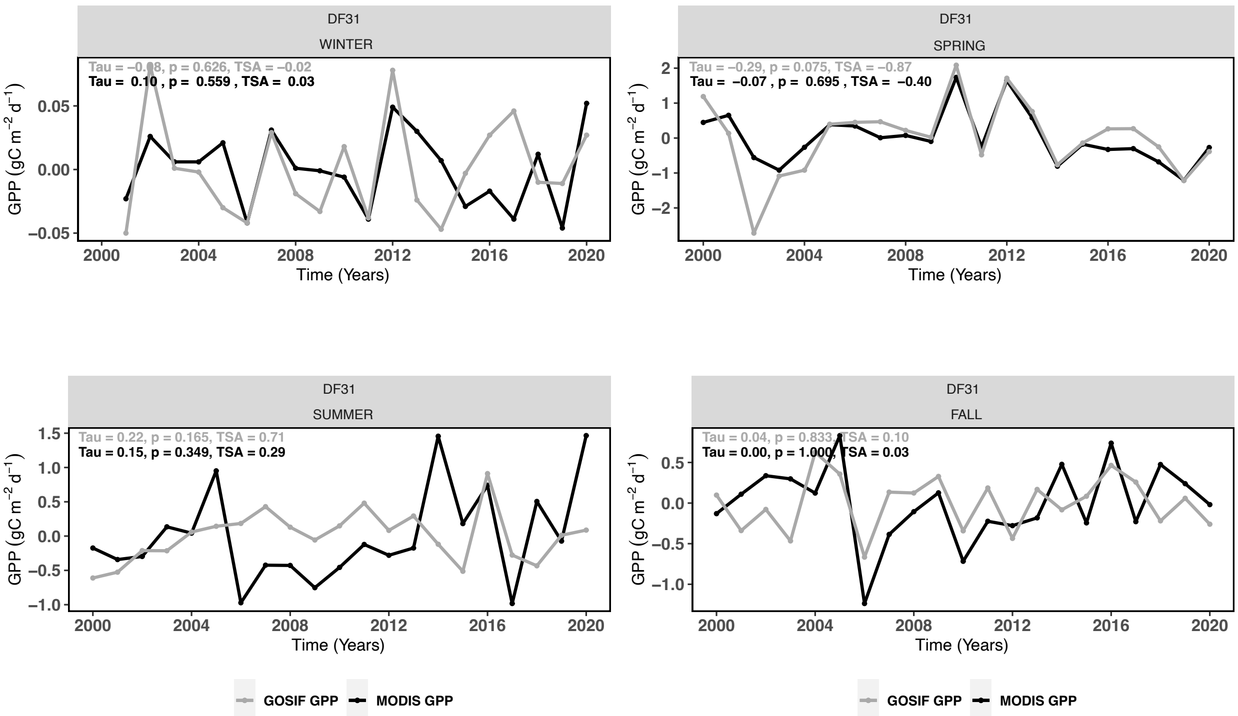
DF31
WINTER
Tau = 0.10 , p = 0.559 , TSA = 0.03
DF31
SPRING
Tau = −0.29, p = 0.075, TSA = −0.87
Tau = −0.07 , p = 0.695 , TSA = −0.40
DF31
SUMMER
Tau = 0.22, p = 0.165, TSA = 0.71
Tau = 0.15, p = 0.349, TSA = 0.29
DF31
FALL
Tau = 0.04, p = 0.833, TSA = 0.10
Tau = 0.00, p = 1.000, TSA = 0.03
GPP (gC m^{-2} d^{-1})
Time (Years)
GOSIF GPP
MODIS GPP

h)

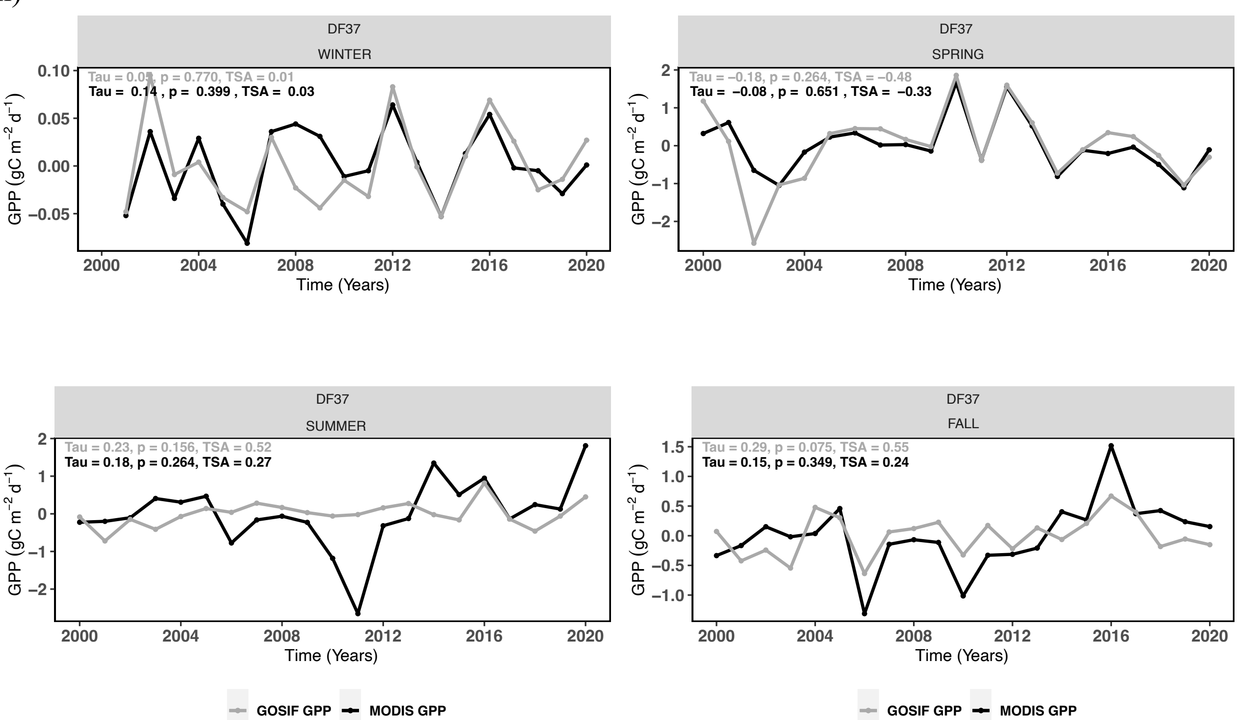
DF37
WINTER
Tau = 0.14 , p = 0.399 , TSA = 0.03
DF37
SPRING
Tau = −0.18, p = 0.264, TSA = −0.48
Tau = −0.08 , p = 0.651 , TSA = −0.33
DF37
SUMMER
Tau = 0.23, p = 0.156, TSA = 0.52
Tau = 0.18, p = 0.264, TSA = 0.27
DF37
FALL
Tau = 0.29, p = 0.075, TSA = 0.55
Tau = 0.15, p = 0.349, TSA = 0.24
GPP (gC m^{-2} d^{-1})
Time (Years)
GOSIF GPP
MODIS GPP

i)

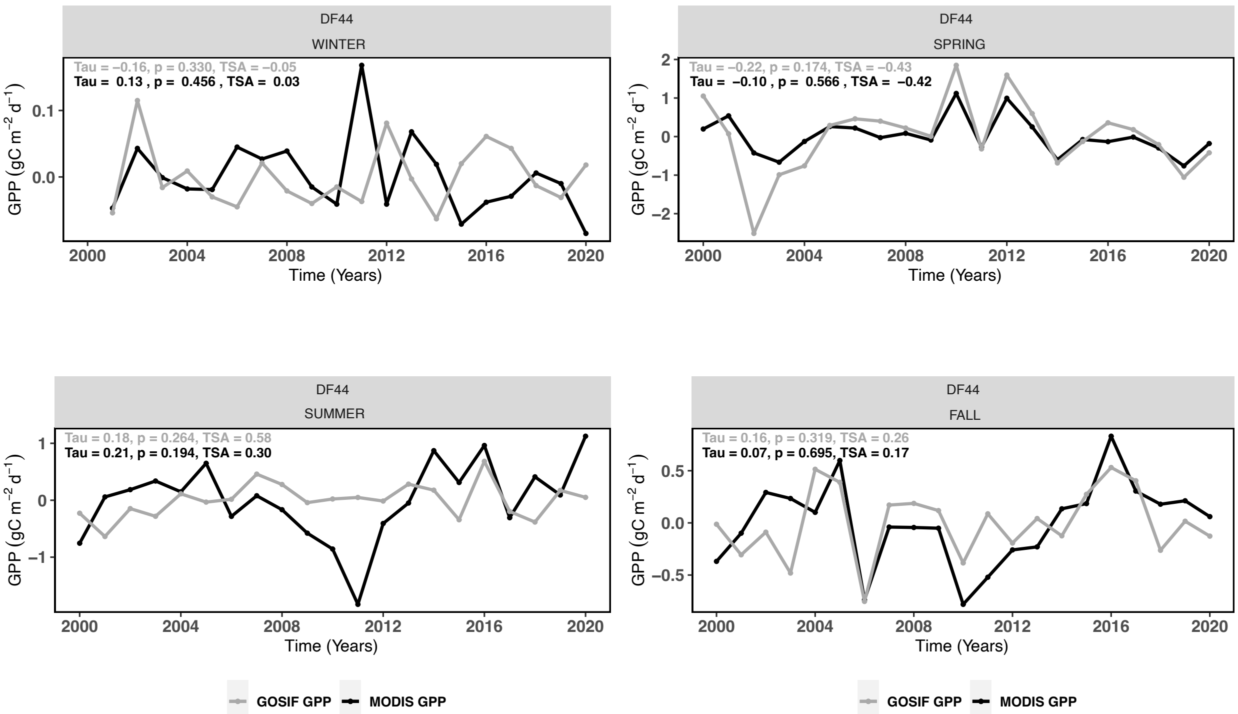

Figure 11. Trends in normalized seasonal GPP for all study sites for both GPP_{GOSIF} and GPP_{MODIS}.

4.3 Response of GPP to climatic variables

Overall, GPP is most responsive to the interannual variability in environmental stressors during the spring (Tables 10 and 11). The strongest improvements in GPP coincide with years of warmer spring temperatures, higher vapor pressure deficits, and higher sunlight receipts, respectively (Tables 10 and 11). Higher moisture levels during the spring, as reflected by either elevated soil moisture or elevated precipitation, universally reduce primary productivity for all cover types (Tables 10 and 11).

Winters exhibit the weakest overall GPP response to environmental variability. Neither forest type responds to any of the winter stressors. Crops improve their productivity in response to warmer winter temperatures and higher vapor pressure deficits but respond negatively to elevated sunlight levels. Crops appear unaffected by winter precipitation (snowfall) variability but benefit marginally from moister soil conditions at this time of year (Tables 10 and 11).

The fall and summer seasons are intermediate in terms of GPP response overall and are seasons where the two forest types clearly differentiate from each other in terms of their response to environmental stressors. The coniferous forest sites carry over their responses from the spring, responding positively to increases in sunlight, temperature, and vapor pressure deficit, and responding negatively to elevated soil moisture levels (Tables 10 and 11). The deciduous forests, however, no longer show a response to VPD, and the response to temperature has reversed during the summer then disappearing altogether by fall. In the fall, GPP in the deciduous forests remains responsive to only elevated sunlight levels. Notably, the strong response of spring crop growth to the interannual variability in the stressors has disappeared entirely by summer. During the fall, warmer temperatures and increased VPD return as beneficial to crop growth, but sunlight and moisture conditions remain uninfluential. Precipitation stands out as being the least influential on GPP of all the environmental stressors, while temperature plays the most dominant role (Tables 10 and 11).

Table 10. Seasonal correlation coefficients, *R* showing the response of GPP_{GOSIF} to various environmental variables for each of the cover types. Shaded values are statistically significant ($p < 0.05$).

		PREC	SSRD	TEMP	VPD	VSW
WINTER	CF	-0.07	0.03	0.08	0.06	-0.03
	CL	0.15	-0.30	0.50	0.52	0.35
	DF	-0.07	-0.04	0.18	0.23	0.07
SPRING	CF	-0.64	0.54	0.64	0.55	-0.66
	CL	-0.48	0.36	0.80	0.70	-0.54
	DF	-0.57	0.50	0.83	0.74	-0.53
SUMMER	CF	-0.14	0.26	0.53	0.41	-0.66
	CL	0.08	-0.17	-0.01	-0.03	0.11
	DF	-0.24	0.24	-0.28	-0.23	-0.34
FALL	CF	-0.48	0.61	0.62	0.37	-0.48
	CL	-0.10	0.13	0.40	0.36	0.08
	DF	-0.20	0.30	0.22	0.00	-0.21

Table 11. Seasonal correlation coefficients, *R* showing the response of GPP_{MODIS} to various environmental variables for each of the cover types. Shaded values are statistically significant ($p < 0.05$).

		PREC	SSRD	TEMP	VPD	VSW
WINTER	CF	-0.01	-0.47	0.83	0.80	0.48
	CL	0.04	-0.46	0.82	0.83	0.59
	DF	-0.16	-0.38	0.74	0.85	0.37
SPRING	CF	-0.25	0.23	0.38	0.35	-0.29
	CL	-0.40	0.40	0.73	0.70	-0.50
	DF	-0.40	0.43	0.72	0.71	-0.47
SUMMER	CF	-0.12	0.50	0.25	0.22	-0.45
	CL	-0.20	-0.09	0.03	-0.02	0.10
	DF	-0.17	0.46	0.19	0.20	-0.25
FALL	CF	-0.66	0.71	0.61	0.51	-0.45
	CL	-0.53	0.46	0.61	0.58	-0.19
	DF	-0.57	0.72	0.58	0.46	-0.39

GPP_{MODIS} correlations show many of the same patterns in GPP response to interannual variability as GPP_{GOSIF}, with a few notable exceptions. Spring is the season when forest and crop growth are most responsive in terms of both sign and magnitude (Table 11). Also, by summer, the responsiveness of crop GPP on environmental factors has disappeared with the reemergence in the importance of temperature and vapor pressure deficit in the fall (Table 11). Overall, temperature variability is the most influential on growth, and precipitation variability is the least influential. Also, except for winter, increases in soil moisture negatively influence GPP (Table 11).

The GPP_{MODIS} model nevertheless departs from its GPP_{GOSIF} counterpart in a few notable cases. For coniferous forests, the benefits of both warmer temperatures and higher vapor pressure deficits that persisted into the summer and fall in GPP_{GOSIF}, temporarily disappear in summer GPP_{MODIS} but then return as important determinants of coniferous growth in the fall (Tables 10 and 11). Furthermore, GPP_{MODIS} shows elevated temperatures and vapor pressure deficits benefitting coniferous forest growth during the winter whereas GPP_{GOSIF} shows no wintertime response (Table 11).

Deciduous forest response also varies differently in GPP_{MODIS} compared to GPP_{GOSIF} (Tables 10 and 11). Upon transitioning from the spring to the summer, deciduous forests are shown to respond negatively to elevated air temperatures in GPP_{GOSIF}, but this influence disappears for GPP_{MODIS} (Tables 10 and 11). As the fall approaches, deciduous forests resume their responses to air temperature variability in a manner like that of coniferous forests (Tables 10 and 11). But then GPP_{MODIS} shows sustained or even enhanced improvements in deciduous forest growth in response to both elevated temperatures and VPD in the winter (Table 11), even though these forests are almost certainly defoliated at this time of year. Also notable is that

GPP_{MODIS} shows large positive correlations between GPP and both temperature and VPD for coniferous forests and crops in winter (Table 11).

4.4 Model comparison

Overall – on a 20-year annual average basis, the GPP means for both models were not significantly different as revealed by the *t* test results for the comparison between the two models t (0.63) = 2.94, $p > 0.53$ (Table 12). There was, however, one significantly larger variation within the summer between the coniferous forests for the two models (Table 14).

Table 12. *t* test results between mean values of GPP_{GOSIF} and GPP_{MODIS} values. *i* represents the degrees of freedom

***t*-value**	***p*-value**	***i***	**GPP_{GOSIF}**	**GPP_{MODIS}**
0.63	0.53	1481.7	4.11	3.99

From the scatter plot in Figure 12, It was evident that the relationship between the model estimates varied greatly by season and land cover type generally. The summer season, which is the most productive, appears in three different clusters, with the deciduous forest being the highest followed by cropland and then deciduous forests. The spring and fall appear around similar zones (have similar productivities) however, the spring has a wider spread than the fall. The fall and spring do not appear in distinct clusters within land cover types like the deciduous forests. The winter is also distinctly located at the bottom left corner of the graph where productivities are least in two distinct clusters. The deciduous forest and croplands form an indistinguishable cluster while the coniferous forests form a distinct cluster of higher productivity because they can still photosynthesize during the winter. Figure 13 shows the range of values for both models indicating a higher level of differentiation of productivity among land cover types in GPP_{GOSIF} than in GPP_{MODIS}.

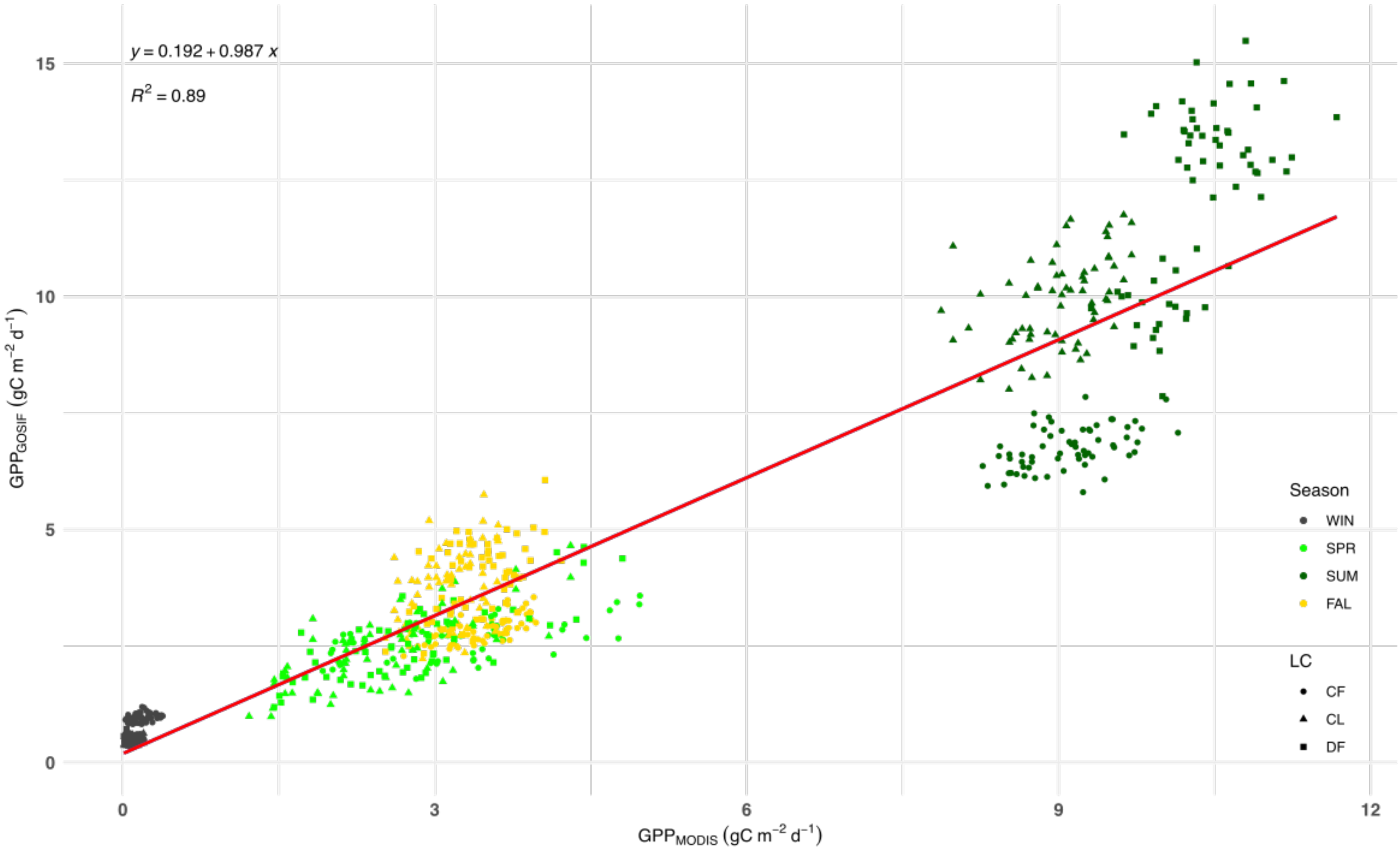

Figure 12. Scatter plot between the two models, showing averaged GPP by season and land cover type.

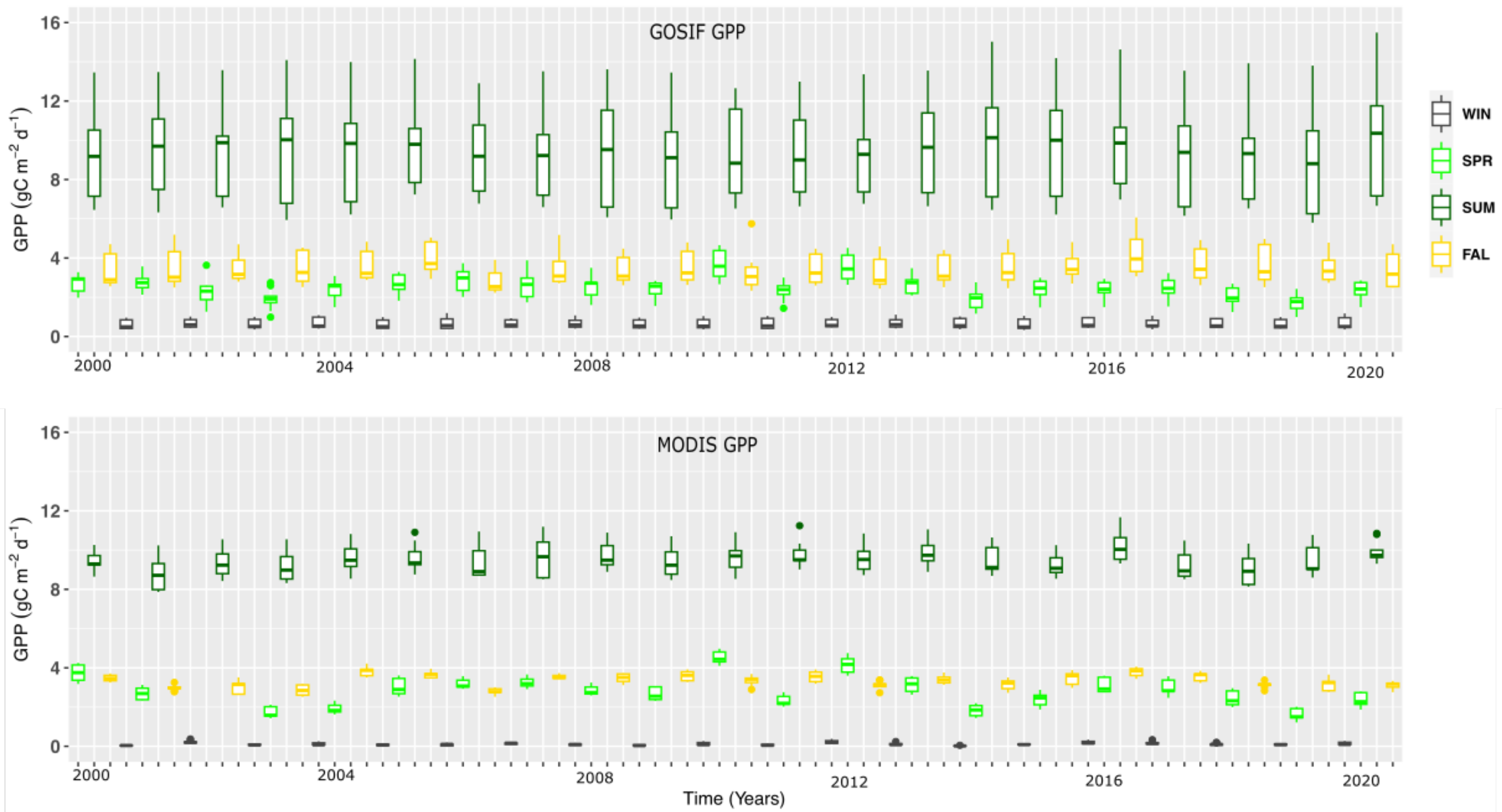

Figure 13. GPP_{MODIS} and GPP_{GOSIF} box plots for all sites are arranged seasonally for all land cover types.

The ANOVA results showed F (3,6) = $p < 0.001$ when both models were compared with each other by season and land cover type (Table 13). I, therefore, accepted the alternate hypothesis and proceeded with a two-way Tukey HSD test to assess which of those particular two-way relationships were significant. Seasonally, there was only one significant difference ($p < 0.01$) that appeared between the means produced from the two different models within a particular season and land cover type, which was for CF in the summer (Table 14).

Table 13. Summary information for ANOVA results of the two GPP models against the three land cover types and four seasons. The degrees of freedom are represented by *i*. SS and MS refer to sum square and mean square respectively.

	i	**SS**	**MS**	***F***	***p***	
LC	2	8.6	4.3	12.752	3.60E-05	***
Season	3	827	275.67	818.15	2.00E-16	***
Model	1	0.3	0.33	0.982	3.30E-01	
LC: Season	6	27.3	4.49	13.334	8.00E-09	***
LC: Model	2	6.1	3.05	9.041	4.70E-04	***
Season: Model	3	1.6	0.52	1.54	2.20E-01	
LC: Season: Model	6	9.9	1.65	4.907	5.50E-04	***
Residuals	48	16.2	0.34			

Table 14. Tukey HSD two-way comparison results of land cover (LC), season, and model. M refers to GPP_{MODIS}, and G refers to GPP_{GOSIF}.

Comparison	**diff**	**lwr**	**upr**	***p***	
CF: WIN:M-CF: WIN: G	-0.8	-2.6	1	0.990	
CL: WIN:M-CL: WIN: G	-0.4	-2.2	1.5	1.000	
DF: WIN:M-DF: WIN: G	-0.4	-2.3	1.4	1.000	
CF: SPR:M-CF: SPR: G	0.6	-1.3	2.4	1.000	
CF: SPR:M-CL: SPR: G	0.8	-1.0	2.6	0.988	
DF: SPR:M-DF: SPR: G	0.2	-1.6	2.0	1.000	
CF: SUM:M-CF: SUM: G	2.3	0.5	4.2	0.002	**
CL: SUM:M-CL: SUM: G	-0.9	-2.8	0.9	0.945	
DF: SUM:M-DF: SUM: G	-1.8	-3.6	0.0	0.056	
CF: FAL:M-CF: FAL: G	0.6	-1.2	2.4	1.000	
CL: FAL:M-CL: FAL: G	-0.6	-2.4	1.2	1.000	
DF: FAL:M-DF: FAL: G	-0.5	-2.4	1.3	1.000	

GPP_{GOSIF} distinguishes itself in the winter GPP values for coniferous forests, as it never drops to zero, while GPP_{MODIS} had very low values, near-zero (Figures 12 and 13). Also, except for CF in the spring, winter, and fall, GPP_{GOSIF} consistently measured higher GPP values than GPP_{MODIS} (Figure 5). The 20-year average of GPP_{GOSIF} demonstrates a greater variability across land cover types and across sites within a land cover type, which is demonstrated in the range of GPP values (Figures 5 and 12).

The two-way Tukey HSD test to assess whether there were differences between both models across seasons (Table 15) and land cover (Table 16) returned no significant differences. The absence of a difference indicates that there is a high level of similarity between the models.

Table 15. Two-way Tukey HSD comparison results of the seasons and models. M and G refer to GPP_{MODIS} and GPP_{GOSIF}, respectively.

Comparison	**diff**	**lwr**	**upr**	***p***
WIN:M-WIN: G	-0.5	-1.4	0.3	0.539
SPR:M-SPR: G	0.3	-0.6	1.2	0.955
SUM:M-SUM: G	-0.1	-1.0	0.7	1.000
FAL:M-FAL: G	-0.2	-1.1	0.7	0.997

Table 16. Two-way Tukey HSD comparison results of land cover and models. M and G refer to GPP_{MODIS} and GPP_{GOSIF}, respectively.

Comparison	**diff**	**lwr**	**upr**	***p***
CF:M-CF: G	0.7	0.0	1.4	0.064
CL:M-CL: G	-0.4	-1.1	0.3	0.432
DF:M-DF: G	-0.6	-1.3	0.1	0.092

The ANOVA results below showed no significant difference between the twenty-year annual means; therefore, no two-way Tukey HSD was performed to assess two-way relationships (Table 17).

Table 17. Summary information for ANOVA results of the two GPP models against the three land cover types and four seasons. The degrees of freedom is represented by *i.* SS and MS refer to sum square and mean square respectively. There were not enough residuals to establish a difference of means.

	i	**SS**	**MS**	***F***	***p***
LC	2	0.281	0.66	24.4	
Model	1	0.0504	140.78	5209.29	
LC: Model	2	0.4614	0.51	19.03	

5 Discussion

How do my GPP estimates compare with others in the literature?

Annual GPP CO_2 uptake estimates for the Peninsula as a whole correspond to 1501.2 $gCm^{-2}yr^{-1}$ and 1457.3 $gCm^{-2}yr^{-1}$ GPP_{GOSIF} and GPP_{MODIS}, respectively. The GPP values in the Bruce Peninsula are marginally larger than most of the other reported ecosystems, likely owing to the fact that the forests are quite young and in a stage of vigorous growth. The forests are estimated to be about 115 years old since the vegetation began to regrow after a massive fire burnt the majority of the Bruce Peninsula (Liipere, 2014). Turner et al., 2003 estimated GPP to be 1639 $gCm^{-2}yr^{-1}$ (flux tower)/ 1501 $gCm^{-2}yr^{-1}$ $gCm^{-2}yr^{-1}$ (MODIS) for a northern hardwood forest and 812 $gCm^{-2}yr^{-1}$ (flux tower) and 1065 $gCm^{-2}yr^{-1}$(MODIS) for a boreal forest in the North East of the United States of America. (Xiao et al. (2004) also estimated the productivity of the Harvard Forest (Hardwood: White Pine and Hemlock) to be 1397 $gCm^{-2}yr^{-1}$. Ise et al. (2010) estimated GPP to be 1297.2 $gCm^{-2}yr^{-1}$ in a cool temperate deciduous broadleaf forest in Takaya, Japan, using MODIS.

5.1 The relative importance of vegetation cover types

The deciduous forests had the strongest uptake of CO_2 for both models annually in the Bruce Peninsula. Depending on the model used, cropland and coniferous forests may differ in importance. This finding has implications for ecosystem management in evaluating how changes to land cover types may impact CO_2 sequestration.

Currently, in the Bruce Peninsula, the dominant land cover type is forest, and it represents 69% of the total land area. Agricultural land cover is the next most dominant land cover type with 16 %. Of the 69 % of the Bruce peninsula's land cover classified as forest, about 20% of all the forests are deciduous, and 80% are coniferous. DF, CF, and CL produce about 13.8% 55.2%, and 16.0% of the land area, respectively, when considered in terms of the total land area in the Bruce Peninsula.

When incorporating the current distribution of vegetative cover, CO_2 uptake by coniferous forests is about three times as large as the other land cover types annually. However, the Bruce Peninsula has a greater potential to sequester more CO_2 when either cropland or coniferous forest is converted to deciduous forest due to its superior ability to sequester CO_2 per square meter, despite its small areal extent, and this is true for both models. When land cover change involves the conversion of coniferous forest to cropland, the impact on CO_2 sequestration is less clear as the impact has opposite signs depending on the model.

Although none of the GOSIF pixels were comprised 100% by a single land cover type, I expected the GPP from both models to differ in the same way between the three land cover classifications. However, that was not the case. The only significant difference between models in 20-year average vegetation growth occurred between the deciduous and coniferous forests in the summertime, and there were no statistically significant differences in GPP between any other land cover types, either seasonally or annually, for either model.

5.2 Observed patterns of climatic trends

As the significant trends in TEMP, SSRD, and VPD weaken or disappear in climate zones further south in the Bruce Peninsula, it appears that Lake Huron and Georgian Bay significantly impact how the weather changes. The locational proximity of the zones notwithstanding, the observed shift from significant to non-significant p-values ($p > 0.05$) in the trends serves as evidence of their distinctiveness.

According to Bello (2022), research conducted using the North American Regional Reanalysis (NARR) model has shown a significant increase in cloudiness throughout the majority of Lake Huron and Georgian Bay during the winter season during the last decade. This agrees with my sunlight results which indicate a decreasing trend in insolation during the winter. Sunlight from the top of the atmosphere remains almost constant. However, the cloud cover makes the amount of sunlight on the Earth's surface variable, and that is what mostly determines sunlight levels. The increases in cloud cover can be explained by increases in evaporation in the winter months due to reduced ice cover. Increased cloud cover enhances downward longwave radiation at the lake surface, further enhancing ice- and snowmelt (Bello, 2022).

The significant decreasing temperature trend in the summer may be attributed to the increasing strength of the onshore winds from Lake Huron and Georgian Bay and may be responsible for moderating the effect of global temperature increases in this localized area. Balogun et al., (2022) also found that the increase in offshore winds has slowed down the increase in temperature (1979-2018) in the Hudson Bay Lowland area in summer as compared to the global temperature rise. They found out that the onshore winds from Hudson Bay are becoming more frequent and stronger due to the sea-breeze effect (due to the differential warming between the Hudson Bay lowlands and the sea – the Hudson Bay), therefore, offsetting the warming influence expected over land not adjacent to water.

5.3 The absence of GPP trends

The land cover within the two forest types would have changed little over the past two decades due to the regulated activities associated with national parks and nature conservancies. Therefore, it was expected that twenty years of forest growth in a forest less than approximately

80 years old would have increased forest biomass and leaf area index and, therefore, increased forest GPP. The absence of a significant trend in annual GPP from either model suggests one of two possibilities: i) that the interannual variability in GPP is large relative to any trends over a twenty-year time series afforded by the data and, therefore, the *noise* in the time series prevents statistical significance at $p < 0.05$ or ii) there may actually have been an environmentally induced decline in GPP per unit leaf area offsetting the expected increase in leaf area.

My expectation was that agricultural landscapes might provide a means of differentiating these latter two complementary influences due to the annual harvest of above-ground biomass in croplands. Perhaps any trends in climate-induced impacts on crop productivity should exhibit significance, in this case. Cropland GPP trends were also not significant. The absence of significant GPP trends in all three landscapes is, however, consistent with an absence of significant annual climate trends. There are some significant environmental trends in the winter, but these would have no potential impact on photosynthesis from leafless vegetation, and although the conifers do photosynthesize in winter, the magnitude of these fluxes is very small – near zero.

Contrary to my findings, Xu et al. (2019) discovered positive significant annual and seasonal trends (1997-2014) in all forest types analyzed, particularly the evergreen needle leaf forest in the Chinese province of Zhejiang. However, any trends in this 20-year time series are likely masked due to the excessive noise in the data- which can be attributed to year-to-year variability. So, the likely cause of the absence of trends is the large inter-annual variability, combined with the fact that most environmental trends are absent or weak or occur in seasons with very little photosynthesis. Additionally, in the case of cropland, a trend's result may be greatly impacted by the type, size, and timing of the crops produced and harvested. While this technique is likely valid for the forest ecosystem where land cover changes are minimal, it might be less effective in identifying the responses to climate change in agricultural systems where land cover changes from year to year could be abrupt.

5.4 Patterns of GPP response to environmental variables

Despite there being no significant long-term trends in GPP or environmental variables for this study, there was considerable interannual variability in both GPP and climate. It was, therefore, instructive to examine how the two modeled seasonal values of GPP respond to commonly available climate variables and assess their relative influence on the year-to-year changes in forest and cropland growth. This helped identify which variables will serve as better or poorer predictors of future productivity variability.

Even though the results indicate that there is no discernable seasonally varying pattern of a particular environmental factor that limits or increases GPP, spring and fall are the seasons that have the highest and most significant R values. Chen et al., (2021) on the contrary found that R between GPP and precipitation was constant throughout the growing season (March to November) however, variation in GPP was due to the varying seasonal influence of temperature and radiation in the Northern Hemisphere. The spring is when most plant life starts growing, and new leaves start appearing. The high correlations may not only reflect the fact that the photochemical reactions or biometeorological reactions of photosynthesis respond to environmental changes but the emergence and expansion of leaves are also almost certainly correlated as well. So, a warm sunny spring may correspond to a high GPP spring partly because there was lots of foliage that year appearing sooner to take advantage of the sunlight and warmer temperatures. Also, fall R values may be large for the same reasons. It could be that a particular fall is highly correlated with temperature because the leaves persisted later into the fall as opposed to another year when the leaves fell sooner because the temperatures were colder, for example.

Ordinarily, the relationship between GPP and VPD is negative however, both models show a strong positive correlation with VPD. The strong positive correlation indicates that perhaps plants are limited by excess humidity and will have a higher GPP from a drier atmosphere in the future. However, when considered on a broad scale, the results indicate a connection between solar radiation, precipitation, vapor pressure deficit, and volumetric soil water in the sense that when the sky becomes cloudier (insolation reduces), it typically rains more (precipitation increases), soil moisture rises (volumetric soil water), and evaporation decreases, causing the air to become less arid (vapor pressure deficit decreases).

The outcomes demonstrated that GPP_{MODIS} was more responsive (higher *R* values and with more occurrences) to environmental factors than GPP_{GOSIF}. Generally, GPP_{MODIS} recorded a significant *R* whenever only one of the two models did. This was contrary to my initial expectations because SIF-based GPP measurement is known to give rapid and ongoing insight into the physiological processes occurring in plants because chlorophyll fluorescence is a direct by-product of photosynthesis. The GPP_{MODIS} product is the result of a model that includes the environmental variables and automatically biases GPP to environmental responses. For instance, it uses climatic variables like VPD as scalars in modeling GPP to mimic the opening and closing of stomates, especially in the winter. The correlation between GPP_{MODIS} appears to have unrealistically high *R* values in the winter for temperature and vapor pressure deficit particularly which is evident in winter. While evergreens are certainly foliated in winter and the same may be true for some pasturelands, it is not immediately clear why the standardized effects ($R > 0.80$)

VPD and temperature should be the strongest relative to any of the other responses listed. Therefore, the higher GPP_{MODIS} responses found in the results are likely an artifact of the computations used to produce this data, especially in the winter.

Summer is the season with the highest GPP for the two models; however, it is the period that shows the least response to the environmental variables used. The fact that the summer has poor *R* values indicates that after the massive GPP response to environmental variables in the spring, the growth conditions exceed the threshold requirements for optimum growth. Therefore any additional supply of any environmental variables does not improve the GPP (Huang et al., 2019). GPP response to temperature indicated that spring and fall show the highest response in both models. Above-average temperatures are beneficial for productivity in these seasons, leading to an improvement in GPP. This finding suggests that the GPP in the Bruce Peninsula ecosystem is likely to improve, resulting from persistently elevated temperatures during the fall and spring seasons in the future.

5.5 Model similarity and performance

Within the northern Bruce Peninsula, there were no known eddy covariance measurement flux tower data sets against which I could compare modeled data over the 20-year period. So, the central thrust of this research was to identify trends and patterns in GPP across different landscapes, assess the responses of the models to climate stressors, and examine the internal consistency of the GPP estimates between the different models. This study does not purport to measure truth; instead, it compares the performance of both models against one another. Therefore, the purpose of the research was not to declare one model superior to the other but rather to identify the trade-offs involved in selecting one model over the other.

The results revealed that the slope of the best-fit line between the two models was almost unity (m = 0.987). The models are therefore almost identical on most occasions however the summer is the greatest distinguishing season between the land cover types where the models differ significantly in their estimation of coniferous forest productivity. The observation that GPP_{GOSIF} typically records greater GPP values, which was notably prevalent during the winter and summer, aligns with the findings of Huang et al., (2019), who also discovered that GPP_{GOSIF} overestimates summer productivity. In addition, GPP_{MODIS} consistently underestimated GPP in evergreen coniferous forests. GPP_{GOSIF} distinguishes itself in the winter GPP values for coniferous forests, as it never drops close to zero, and this agrees with what we know about evergreens – which photosynthesize all year round, including the winter time. This indicates that GPP_{GOSIF} recognizes and distinguishes between distinct land cover types better than $GPP_{MODIS,}$ which classifies sites into plant functional types and views everything in a given pixel as one vegetation type. Qiu et al (2020) stated that GPP_{MODIS} likely has a low LUE parameter for crops particularly, which causes it to consistently underestimate its productivity. The GPP_{MODIS} underestimation is particularly true for conifers and croplands. Generally, GPP_{MODIS} has a better correlation with the five environmental variables used here than GPP_{GOSIF}. This explains the moderating effect of VPD mimicking physiological processes in the winter – the opening and closing of the stomata of plants – for GPP_{MODIS}. The VPD factor may however may be excessively weighted in the in GPP_{MODIS} to provide such high correlations. GPP_{GOSIF}, however, shows very little response to VPD throughout the results. The range of GPP_{GOSIF} values is also larger, indicating a higher interannual variability than for GPP_{GOSIF} than for GPP_{MODIS} and indicates a higher distinguishing. Although the two models only provide estimates and there are no actual ground measurements from the sites, it appears that GPP_{GOSIF} is more representative of the expected responses to climatic variables. The winter is the season when this is especially true when there are no leaves and there are unfavorable environmental conditions.

6 Conclusions

The purpose of this thesis was to objectively assess how climatic changes and stresses affected the vegetation communities in the Bruce Peninsula region. The findings showed that there were no trends in GPP in the Bruce Peninsula in either of the models over the 20 years of the study period. There were only a few seasonal climate trends present in the three northernmost sites in the Peninsula, where the massive nearby water sources had the greatest influence. The seasons that showed the highest responses to environmental influences were the fall and spring, with the GPP_{MODIS} having a much greater frequency and magnitude of significant responses than GPP_{GOSIF}. The spring is the period of leaf emergence in deciduous vegetation, also new needles emerge in the spring in evergreens. Any factor that spurs earlier leaf emergence in a particular year would benefit CO_2 uptake. The fall is the period of leaf senescence in deciduous vegetation and maximal senescence in evergreens, particularly Eastern White Cedar. Any factor that delays leaf fall in a particular year would benefit CO_2 uptake.

In terms of the objectives outlined in the introduction, this study has demonstrated that:

i) A significant difference only exists between CF and the other land cover types in the summer for GPP_{GOSIF} and summer and spring between DF and the other land cover types in the summer and between CL and CF in the spring for GPP_{MODIS}.

ii) There were no trends in GPP for any of the two models, but there were significant decreasing trends in temperature and vapor pressure deficit in the summer and solar radiation in the winter.

iii) The most responsive periods for GPP response to environmental variables are in the spring and fall, and GPP_{MODIS} had higher frequencies of significant ($p < 0.05$) R values, although it had unrealistically high correlations ($R > 8.0$) in the winter.

iv) On a twenty-year annual scale, there was no significant difference between the two models, but on a seasonal basis, only the summer for CF differed significantly.

Analysis of future climate change scenarios was not undertaken in this thesis. Despite the observation that changes to the climate on the Bruce Peninsula over the past 20 years have been quite subdued due to the moderating influence of Lake Huron and Georgian Bay, caution should be exercised in inferring that the carbon dynamics are immune to climate change. The stresses on GPP generated by year-to-year variability in climate have been shown to be significant, particularly in the spring and fall. As stresses become more frequent or persistent, not only could trends emerge in GPP but changes in the composition of the forest community may follow in response to, for example, tree mortality which can strongly impact biomass accumulation. The net exchange of CO_2 between the Bruce Peninsula ecosystem and the overlying atmosphere also depends on respiration (equation 1) which is co-dependent on root respiration and soil decomposition. These too are dependent on environmental stressors and are all factors which deserve urgent consideration. Therefore, given how crucial GPP is for understanding climate change and its effects, it is crucial that we keep working to discover new technologies and methods for measuring it effectively.

7 References

Amiro, B. D., Barr, A. G., Barr, J. G., Black, T. A., Bracho, R., Brown, M., Chen, J., Clark, K. L., Davis, K. J., Desai, A. R., Dore, S., Engel, V., Fuentes, J. D., Goldstein, A. H., Goulden, M. L., Kolb, T. E., Lavigne, M. B., Law, B. E., Margolis, H. A., … Xiao, J. (2010). Ecosystem carbon dioxide fluxes after disturbance in forests of North America. *Journal of Geophysical Research*, *115*, G00K02. https://doi.org/10.1029/2010JG001390

Baguley, T. (2009). Standardized or simple effect size: What should be reported? *British Journal of Psychology*, *100*(3), 603–617. https://doi.org/10.1348/000712608X377117

Baldocchi, D. D. (2003). Assessing the eddy covariance technique for evaluating carbon dioxide exchange rates of ecosystems: Past, present and future: carbon balance and eddy covariance. *Global Change Biology*, *9*(4), 479–492. https://doi.org/10.1046/j.1365-2486.2003.00629.x

Balogun, O., Bello, R., & Higuchi, K. (2022). NARR-based analysis of changes in the mesoscale wind and temperature over the Hudson Bay Lowlands and their impact on the surface energy balance: 1979–2018. *Polar Science*, *33*, 100861. https://doi.org/10.1016/j.polar.2022.100861

Balogun, O., Bello, R., & Higuchi, K. (2023). Terrestrial CO_2 exchange diagnosis using a peatland-optimized vegetation photosynthesis and respiration model (VPRM) for the Hudson Bay Lowlands. *Science of The Total Environment*, *875*, 162591. https://doi.org/10.1016/j.scitotenv.2023.162591

Bello, R. (2022, Fall). *Lake Huron & Georgian Bay Climate Change of the past decade 2011-2020*.

Bello, R., & Higuchi, K. (2019). Changing surface radiation and energy budgets of the Hudson Bay Complex using the North American regional reanalysis (NARR) model. *Arctic Science*, *5*(4), 218–239. https://doi.org/10.1139/as-2018-0034

Berger, S., Connors, S. L., Allan, R. P., Berntsen, T., Bock, L., Cerezo-Mota, R., & Cobb, K. (2021). *FAQ Frequently Asked Questions*.

Berry, J., & Frankenberg, C. (2012). *New Methods for Measurements of Photosynthesis from Space*. 72.

Birkel, S. D. (2023). *"Daily 2-meter Air Temperature"* [dataset]. Climate Change Institute, University of Maine, USA. https://ClimateReanalyzer.org

Bonan, G. (2019). *Climate Change and Terrestrial Ecosystem Modeling* (1st ed.). Cambridge University Press. https://doi.org/10.1017/9781107339217

Bonan, G. B. (2016). *Ecological climatology: Concepts and applications* (Third edition). Cambridge University Press.

Bronaugh, D., Schoeneberg, A., & Lee, Z. (2023). *Zhang + Yue-Pilon Trends Package*. https://www.r-project.org

Buck, A., L. (1981). *New Equations for Computing Vapor Pressure and Enhancement Factor*. Journal of Applied Meteorology and Climatology. https://doi.org/10.1175/1520-0450(1981)020<1527:NEFCVP>2.0.CO;2

Chaudhary, N., Miller, P. A., & Smith, B. (2017). Modelling past, present and future peatland carbon accumulation across the pan-Arctic region. *Biogeosciences*, *14*(18), 4023–4044. https://doi.org/10.5194/bg-14-4023-2017

Chen, A., Mao, J., Ricciuto, D., Lu, D., Xiao, J., Li, X., Thornton, P. E., & Knapp, A. K. (2021). Seasonal changes in GPP/SIF ratios and their climatic determinants across the Northern Hemisphere. *Global Change Biology*, *27*(20), 5186–5197. https://doi.org/10.1111/gcb.15775

Ferreira, R. R., Santos E Silva, C. M., Bezerra, B., Mendes, K. R., Mutti, P., Campos, S., Marques, T. V., P. Oliveira, C., Gonçalves, W., Espinoza, N., Difante, G., & Urbano, S. A. (2021). A brief evaluation of the MOD17A2H product over a pasture in northeast Brazil. *Remote Sensing Letters*, *12*(1), 50–57. https://doi.org/10.1080/2150704X.2021.1875144

Frankenberg, C., Butz, A., & Toon, G. C. (2011). Disentangling chlorophyll fluorescence from atmospheric scattering effects in O_2 A-band spectra of reflected sun-light: Remote sensing of chlorophyll fluorescence. *Geophysical Research Letters*, *38*(3), n/a-n/a. https://doi.org/10.1029/2010GL045896

Frankenberg, C., O'Dell, C., Berry, J., Guanter, L., Joiner, J., Köhler, P., Pollock, R., & Taylor, T. E. (2014). Prospects for chlorophyll fluorescence remote sensing from the Orbiting Carbon Observatory-2. *Remote Sensing of Environment*, *147*, 1–12. https://doi.org/10.1016/j.rse.2014.02.007

Frankenberg, C., O'Dell, C., Guanter, L., & McDuffie, J. (2012). Remote sensing of near-infrared chlorophyll fluorescence from space in scattering atmospheres: Implications for its retrieval and interferences with atmospheric CO₂ retrievals. *Atmospheric Measurement Techniques*, *5*(8), 2081–2094. https://doi.org/10.5194/amt-5-2081-2012

Friedlingstein, P., Jones, M. W., O'Sullivan, M., Andrew, R. M., Hauck, J., Peters, G. P., Peters, W., Pongratz, J., Sitch, S., Le Quéré, C., Bakker, D. C. E., Canadell, J. G., Ciais, P., Jackson, R. B., Anthoni, P., Barbero, L., Bastos, A., Bastrikov, V., Becker, M., … Zaehle, S. (2019). Global Carbon Budget 2019. *Earth System Science Data*, *11*(4), 1783–1838. https://doi.org/10.5194/essd-11-1783-2019

Gebremichael, M., & Barros, A. (2006). Evaluation of MODIS Gross Primary Productivity (GPP) in tropical monsoon regions. *Remote Sensing of Environment*, *100*(2), 150–166. https://doi.org/10.1016/j.rse.2005.10.009

Glenn, E., Huete, A., Nagler, P., & Nelson, S. (2008). Relationship Between Remotely-sensed Vegetation Indices, Canopy Attributes and Plant Physiological Processes: What Vegetation Indices Can and Cannot Tell Us About the Landscape. *Sensors*, *8*(4), 2136–2160. https://doi.org/10.3390/s8042136

Global Monitoring Laboratory - Carbon Cycle Greenhouse Gases. (n.d.). *Global Monitoring Laboratory—Carbon Cycle Greenhouse Gases*. https://gml.noaa.gov/ccgg/trends/

Guanter, L., Frankenberg, C., Dudhia, A., Lewis, P. E., Gómez-Dans, J., Kuze, A., Suto, H., & Grainger, R. G. (2012). Retrieval and global assessment of terrestrial chlorophyll fluorescence from GOSAT space measurements. *Remote Sensing of Environment*, *121*, 236–251. https://doi.org/10.1016/j.rse.2012.02.006

Guanter, L., Zhang, Y., Jung, M., Joiner, J., Voigt, M., Berry, J. A., Frankenberg, C., Huete, A. R., Zarco-Tejada, P., Lee, J.-E., Moran, M. S., Ponce-Campos, G., Beer, C., Camps-Valls, G., Buchmann, N., Gianelle, D., Klumpp, K., Cescatti, A., Baker, J. M., & Griffis, T. J. (2014). Global and time-resolved monitoring of crop photosynthesis with chlorophyll fluorescence. *Proceedings of the National Academy of Sciences*, *111*(14). https://doi.org/10.1073/pnas.1320008111

Hersbach, H., Bell, B., Berrisford, P., Hirahara, S., Horányi, A., Nicolas, J., Peubey, C., Radu, R., Simmons, A., Soci, C., Abdalla, S., Balsamo, G., Bechtold, P., Biavati, G., Bonavita, M., Chiara, G. D., Dahlgren, P., Dee, D., Dragani, R., … Thépaut, J.-N. (2020). *The ERA5 global reanalysis*. (https://cds.climate.copernicus.eu/#!/home

Hu, L., Andrews, A. E., Thoning, K. W., Sweeney, C., Miller, J. B., Michalak, A. M., Dlugokencky, E., Tans, P. P., Shiga, Y. P., Mountain, M., Nehrkorn, T., Montzka, S. A., McKain, K., Kofler, J., Trudeau, M., Michel, S. E., Biraud, S. C., Fischer, M. L., Worthy, D. E. J., … Van Der Velde, I. R. (2019). Enhanced North American carbon uptake associated with El Niño. *Science Advances*, *5*(6), eaaw0076. https://doi.org/10.1126/sciadv.aaw0076

Huang, Liu, Zhu, Atzberger, & Liu. (2019). The Optimal Threshold and Vegetation Index Time Series for Retrieving Crop Phenology Based on a Modified Dynamic Threshold Method. *Remote Sensing*, *11*(23), 2725. https://doi.org/10.3390/rs11232725

Huang, M., Piao, S., Ciais, P., Peñuelas, J., Wang, X., Keenan, T. F., Peng, S., Berry, J. A., Wang, K., Mao, J., Alkama, R., Cescatti, A., Cuntz, M., De Deurwaerder, H., Gao, M., He, Y., Liu, Y., Luo, Y., Myneni, R. B., … Janssens, I. A. (2019). Air temperature optima of vegetation productivity across global biomes. *Nature Ecology & Evolution*, *3*(5), 772–779. https://doi.org/10.1038/s41559-019-0838-x

IPCC. (2022). Climate Change 2022: Impacts, Adaptation and Vulnerability. Working Group II Contribution to the IPCC Sixth Assessment Report. Cambridge University Press. Cambridge University Press, Cambridge, UK and New York, NY, USA. https://doi.org/10.1017/9781009325844

Ise, T., Litton, C. M., Giardina, C. P., & Ito, A. (2010). Comparison of modeling approaches for carbon partitioning: Impact on estimates of global net primary production and equilibrium biomass of woody vegetation from MODIS GPP. *Journal of Geophysical Research*, *115*(G4), G04025. https://doi.org/10.1029/2010JG001326

Jian, J., Bailey, V., Dorheim, K., Konings, A. G., Hao, D., Shiklomanov, A. N., Snyder, A., Steele, M., Teramoto, M., Vargas, R., & Bond-Lamberty, B. (2022). Historically inconsistent productivity and respiration fluxes in the global terrestrial carbon cycle. *Nature Communications*, *13*(1), 1733. https://doi.org/10.1038/s41467-022-29391-5

Joiner, J., Guanter, L., Lindstrot, R., Voigt, M., Vasilkov, A. P., Middleton, E. M., Huemmrich, K. F., Yoshida, Y., & Frankenberg, C. (2013). Global monitoring of terrestrial chlorophyll fluorescence from moderate-spectral-resolution near-infrared satellite measurements: Methodology, simulations, and application to GOME-2. *Atmospheric Measurement Techniques*, *6*(10), 2803–2823. https://doi.org/10.5194/amt-6-2803-2013

Joiner, J., Yoshida, Y., Vasilkov, A. P., Schaefer, K., Jung, M., Guanter, L., Zhang, Y., Garrity, S., Middleton, E. M., Huemmrich, K. F., Gu, L., & Belelli Marchesini, L. (2014). The seasonal cycle of satellite chlorophyll fluorescence observations and its relationship to vegetation phenology and ecosystem atmosphere carbon exchange. *Remote Sensing of Environment*, *152*, 375–391. https://doi.org/10.1016/j.rse.2014.06.022

Joiner, J., Yoshida, Y., Vasilkov, A. P., Yoshida, Y., Corp, L. A., & Middleton, E. M. (2011). First observations of global and seasonal terrestrial chlorophyll fluorescence from space. *Biogeosciences*, *8*(3), 637–651. https://doi.org/10.5194/bg-8-637-2011

Jung, M., Reichstein, M., Margolis, H. A., Cescatti, A., Richardson, A. D., Arain, M. A., Arneth, A., Bernhofer, C., Bonal, D., Chen, J., Gianelle, D., Gobron, N., Kiely, G., Kutsch, W., Lasslop, G., Law, B. E., Lindroth, A., Merbold, L., Montagnani, L., … Williams, C. (2011). Global patterns of land-atmosphere fluxes of carbon dioxide, latent heat, and sensible heat derived from eddy covariance, satellite, and meteorological observations. *Journal of Geophysical Research*, *116*, G00J07. https://doi.org/10.1029/2010JG001566

Kalaji, H. M., Schansker, G., Brestic, M., Bussotti, F., Calatayud, A., Ferroni, L., Goltsev, V., Guidi, L., Jajoo, A., Li, P., Losciale, P., Mishra, V. K., Misra, A. N., Nebauer, S. G., Pancaldi, S., Penella, C., Pollastrini, M., Suresh, K., Tambussi, E., … Bąba, W. (2017). Frequently asked questions about chlorophyll fluorescence, the sequel. *Photosynthesis Research*, *132*(1), 13–66. https://doi.org/10.1007/s11120-016-0318-y

Kelly, P. E., Cook E.R, & Larson D.W. (1994). A 1397-year tree-ring chronology of Thujaoccidentalis from cliff faces of the Niagara Escarpment, southern Ontario, Canada. *Canadian Journal of Forest Research*, *24*(5), 1049–1057. https://doi.org/10.1139/x94-137

Köhler, P., Guanter, L., & Joiner, J. (2015). A linear method for the retrieval of sun-induced chlorophyll fluorescence from GOME-2 and SCIAMACHY data. *Atmos. Meas. Tech.*

Latifovic, R. (2023). *Land cover Map of Canada 2020.* [dataset]. https://open.canada.ca/data/en/dataset/ee1580ab-a23d-4f86-a09b-79763677eb47

Latifovic, R., Pouliot, D., & Olthof, I. (2017). Circa 2010 Land Cover of Canada: Local Optimization Methodology and Product Development. *Remote Sensing*, *9*(11), 1098. https://doi.org/10.3390/rs9111098

Le Quéré, C., Moriarty, R., Andrew, R. M., Canadell, J. G., Sitch, S., Korsbakken, J. I., Friedlingstein, P., Peters, G. P., Andres, R. J., Boden, T. A., Houghton, R. A., House, J. I., Keeling, R. F., Tans, P., Arneth, A., Bakker, D. C. E., Barbero, L., Bopp, L., Chang, J., … Zeng, N. (2015). Global Carbon Budget 2015. *Earth System Science Data*, *7*(2), 349–396. https://doi.org/10.5194/essd-7-349-2015

Lee, J.-E., Berry, J. A., Van Der Tol, C., Yang, X., Guanter, L., Damm, A., Baker, I., & Frankenberg, C. (2015). Simulations of chlorophyll fluorescence incorporated into the Community Land Model version 4. *Global Change Biology*, *21*(9), 3469–3477. https://doi.org/10.1111/gcb.12948

Lee, J.-E., Frankenberg, C., Van Der Tol, C., Berry, J. A., Guanter, L., Boyce, C. K., Fisher, J. B., Morrow, E., Worden, J. R., Asefi, S., Badgley, G., & Saatchi, S. (2013). Forest productivity and water stress in Amazonia: Observations from GOSAT chlorophyll fluorescence. *Proceedings of the Royal Society B: Biological Sciences*, *280*(1761), 20130171. https://doi.org/10.1098/rspb.2013.0171

Lees, K. J., Quaife, T., Artz, R. R. E., Khomik, M., & Clark, J. M. (2018). Potential for using remote sensing to estimate carbon fluxes across northern peatlands – A review. *Science of The Total Environment*, *615*, 857–874. https://doi.org/10.1016/j.scitotenv.2017.09.103

Li, X., Xiao, J., & He, B. (2018). Chlorophyll fluorescence observed by OCO-2 is strongly related to gross primary productivity estimated from flux towers in temperate forests. *Remote Sensing of Environment*, *204*, 659–671. https://doi.org/10.1016/j.rse.2017.09.034

Li & Xiao. (2019). Mapping Photosynthesis Solely from Solar-Induced Chlorophyll Fluorescence: A Global, Fine-Resolution Dataset of Gross Primary Production Derived from OCO-2. *Remote Sensing*, *11*(21), 2563. https://doi.org/10.3390/rs11212563

Liao, Z., Zhou, B., Zhu, J., Jia, H., & Fei, X. (2023). A critical review of methods, principles and progress for estimating the gross primary productivity of terrestrial ecosystems. *Frontiers in Environmental Science*, *11*, 1093095. https://doi.org/10.3389/fenvs.2023.1093095

Liipere, S. (2014). BPBA Conservation & Stewardship Plan Bruce Peninsula. Bruce Peninsula Biosphere Association, Lion's Head, Ontario.

Long, S. P. (2003). Gas exchange measurements, what can they tell us about the underlying limitations to photosynthesis? Procedures and sources of error. *Journal of Experimental Botany*, *54*(392), 2393–2401. https://doi.org/10.1093/jxb/erg262

Luus, K. A., Commane, R., Parazoo, N. C., Benmergui, J., Euskirchen, E. S., Frankenberg, C., Joiner, J., Lindaas, J., Miller, C. E., Oechel, W. C., Zona, D., Wofsy, S., & Lin, J. C. (2017). Tundra photosynthesis captured by satellite-observed solar-induced chlorophyll fluorescence. *Geophysical Research Letters*, *44*(3), 1564–1573. https://doi.org/10.1002/2016GL070842

Maxwell, K., & Johnson, G. N. (2000). Chlorophyll fluorescence—a practical guide. *Journal of Experimental Botany*, *51*(345), 659–668. https://doi.org/10.1093/jexbot/51.345.659

McLeod, A. I. (2011). *Kendall Rank Correlation and Mann-Kendall Trend Test*. http://www.stats.uwo.ca/faculty/aim. R Package Kendall. https://CRAN.R-project.org/package=Kendall.

Medlyn, B. E. (1998). Physiological basis of the light use efficiency model. *Tree Physiology*, *18*(3), 167–176. https://doi.org/10.1093/treephys/18.3.167

Melton, J. R., Arora, V. K., Wisernig-Cojoc, E., Seiler, C., Fortier, M., Chan, E., & Teckentrup, L. (2020). CLASSIC v1.0: The open-source community successor to the Canadian Land Surface Scheme (CLASS) and the Canadian Terrestrial Ecosystem Model (CTEM) – Part 1: Model framework and site-level performance. *Geoscientific Model Development*, *13*(6), 2825–2850. https://doi.org/10.5194/gmd-13-2825-2020

Meroni, M., Rossini, M., Guanter, L., Alonso, L., Rascher, U., Colombo, R., & Moreno, J. (2009). Remote sensing of solar-induced chlorophyll fluorescence: Review of methods and applications. *Remote Sensing of Environment*, *113*(10), 2037–2051. https://doi.org/10.1016/j.rse.2009.05.003

Mohammed, G. H., Colombo, R., Middleton, E. M., Rascher, U., van der Tol, C., Nedbal, L., Goulas, Y., Pérez-Priego, O., Damm, A., Meroni, M., Joiner, J., Cogliati, S., Verhoef, W., Malenovský, Z., Gastellu-Etchegorry, J.-P., Miller, J. R., Guanter, L., Moreno, J., Moya, I., … Zarco-Tejada, P. J. (2019). Remote sensing of solar-induced chlorophyll fluorescence (SIF) in vegetation: 50 years of progress. *Remote Sensing of Environment*, *231*, 111177. https://doi.org/10.1016/j.rse.2019.04.030

Monteith, J. L. (1972). Solar Radiation and Productivity in Tropical Ecosystems. *The Journal of Applied Ecology*, *9*(3), 747. https://doi.org/10.2307/2401901

Nuarsa, I., As-syakur, Abd., Gunadi, I., & Sukewijaya, I. (2018). Changes in Gross Primary Production (GPP) over the Past Two Decades Due to Land Use Conversion in a Tourism

City. *ISPRS International Journal of Geo-Information*, *7*(2), 57. https://doi.org/10.3390/ijgi7020057

ORNL DAAC. (2018). *MODIS and VIIRS Land Products Global Subsetting and Visualization Tool. ORNL DAAC, Oak Ridge, Tennessee, USA.* https://doi.org/10.3334/ORNLDAAC/1379

Park, H., Im, J., & Kim, M. (2019). Improvement of satellite-based estimation of gross primary production through optimization of meteorological parameters and high resolution land cover information at regional scale over East Asia. *Agricultural and Forest Meteorology*, *271*, 180–192. https://doi.org/10.1016/j.agrformet.2019.02.040

Parker, S. (2017). *Let's Talk about Climate Change: Great Lakes Region*. https://doi.org/10.13140/RG.2.2.28612.17289

Pei, Y., Dong, J., Zhang, Y., Yuan, W., Doughty, R., Yang, J., Zhou, D., Zhang, L., & Xiao, X. (2022). Evolution of light use efficiency models: Improvement, uncertainties, and implications. *Agricultural and Forest Meteorology*, *317*, 108905. https://doi.org/10.1016/j.agrformet.2022.108905

Perez-Priego, O., Guan, J., Rossini, M., Fava, F., Wutzler, T., Moreno, G., Carvalhais, N., Carrara, A., Kolle, O., Julitta, T., Schrumpf, M., Reichstein, M., & Migliavacca, M. (2015). Sun-induced chlorophyll fluorescence and photochemical reflectance index improve remote-sensing gross primary production estimates under varying nutrient availability in a typical Mediterranean savanna ecosystem. *Biogeosciences*, *12*(21), 6351–6367. https://doi.org/10.5194/bg-12-6351-2015

Porcar-Castell, A., Tyystjärvi, E., Atherton, J., van der Tol, C., Flexas, J., Pfündel, E. E., Moreno, J., Frankenberg, C., & Berry, J. A. (2014). Linking chlorophyll a fluorescence to photosynthesis for remote sensing applications: Mechanisms and challenges. *Journal of Experimental Botany*, *65*(15), 4065–4095. https://doi.org/10.1093/jxb/eru191

Potter, C. S., Randerson, J. T., Field, C. B., Matson, P. A., Vitousek, P. M., Mooney, H. A., & Klooster, S. A. (1993). Terrestrial ecosystem production: A process model based on global satellite and surface data. *Global Biogeochemical Cycles*, *7*(4), 811–841. https://doi.org/10.1029/93GB02725

Qiu, R., Han, G., Ma, X., Xu, H., Shi, T., & Zhang, M. (2020). A Comparison of OCO-2 SIF, MODIS GPP, and GOSIF Data from Gross Primary Production (GPP) Estimation and

Seasonal Cycles in North America. *Remote Sensing*, *12*(2), 258. https://doi.org/10.3390/rs12020258

R Core Team (2023). R: A language and environment for statistical computing. R Foundation for Statistical Computing, Vienna, Austria. https://www.R-project.org/.

Raupach, M. R., Canadell, J. G., & Quere, C. L. (2008). Anthropogenic and biophysical contributions to increasing atmospheric CO_2 growth rate and airborne fraction. *Biogeosciences*, 5(6), 1601–1613. https://doi.org/10.5194/bg-5-1601-2008

Running, S. W., Nemani, R. R., Heinsch, F. A., Zhao, M., Reeves, M., & Hashimoto, H. (2004). A Continuous Satellite-Derived Measure of Global Terrestrial Primary Production. *BioScience*, *54*(6), 547. https://doi.org/10.1641/0006-3568(2004)054[0547:ACSMOG]2.0.CO;2

Running, S. W., & Zhao, M. (2021a). Daily GPP and Annual NPP (MOD17A2H/A3H) and Year-end Gap- Filled (MOD17A2HGF/A3HGF) Products NASA Earth Observing System MODIS Land Algorithm *(For Collection 6.1)*. 38.

Running, S. W., & Zhao, M. (2021b). *MYD17A2HGF MODIS/Aqua Gross Primary Productivity Gap-Filled 8-Day L4 Global 500 m SIN Grid V061.* [dataset]. https://doi.org/10.5067/MODIS/MYD17A2HGF.061

Santiago, H. (2020). *RobustLinearReg* [dataset]. https://CRAN.R-project.org/package=RobustLinearReg

Sasai, T., Okamoto, K., Hiyama, T., & Yamaguchi, Y. (2007). Comparing terrestrial carbon fluxes from the scale of a flux tower to the global scale. *Ecological Modelling*, *208*(2–4), 135–144. https://doi.org/10.1016/j.ecolmodel.2007.05.014

Schimel, D., Pavlick, R., Fisher, J. B., Asner, G. P., Saatchi, S., Townsend, P., Miller, C., Frankenberg, C., Hibbard, K., & Cox, P. (2015). Observing terrestrial ecosystems and the carbon cycle from space. *Global Change Biology*, *21*(5), 1762–1776. https://doi.org/10.1111/gcb.12822

Schlund, M., Eyring, V., Camps-Valls, G., Friedlingstein, P., Gentine, P., & Reichstein, M. (2020). Constraining Uncertainty in Projected Gross Primary Production With Machine Learning. *Journal of Geophysical Research: Biogeosciences*, *125*(11). https://doi.org/10.1029/2019JG005619

St-Hilaire, F., Wu, J., Roulet, N. T., Frolking, S., Lafleur, P. M., Humphreys, E. R., & Arora, V. (2010). McGill wetland model: Evaluation of a peatland carbon simulator developed for global assessments. *Biogeosciences*, *7*(11), 3517–3530. https://doi.org/10.5194/bg-7-3517-2010

Tol, C., Berry, J. A., Campbell, P. K. E., & Rascher, U. (2014). Models of fluorescence and photosynthesis for interpreting measurements of solar-induced chlorophyll fluorescence. *Journal of Geophysical Research: Biogeosciences*, *119*(12), 2312–2327. https://doi.org/10.1002/2014JG002713

Turner, D. P., Ritts, W. D., Cohen, W. B., Gower, S. T., Zhao, M., Running, S. W., Wofsy, S. C., Urbanski, S., Dunn, A. L., & Munger, J. W. (2003). Scaling Gross Primary Production (GPP) over boreal and deciduous forest landscapes in support of MODIS GPP product validation. *Remote Sensing of Environment*, *88*(3), 256–270. https://doi.org/10.1016/j.rse.2003.06.005

Verma, M., Schimel, D., Evans, B., Frankenberg, C., Beringer, J., Drewry, D. T., Magney, T., Marang, I., Hutley, L., Moore, C., & Eldering, A. (2017). Effect of environmental conditions on the relationship between solar-induced fluorescence and gross primary productivity at an OzFlux grassland site. *Journal of Geophysical Research: Biogeosciences*, *122*(3), 716–733. https://doi.org/10.1002/2016JG003580

Walther, S., Voigt, M., Thum, T., Gonsamo, A., Zhang, Y., Köhler, P., Jung, M., Varlagin, A., & Guanter, L. (2016). Satellite chlorophyll fluorescence measurements reveal large-scale decoupling of photosynthesis and greenness dynamics in boreal evergreen forests. *Global Change Biology*, *22*(9), 2979–2996. https://doi.org/10.1111/gcb.13200

Wang, L., Zhu, H., Lin, A., Zou, L., Qin, W., & Du, Q. (2017). Evaluation of the Latest MODIS GPP Products across Multiple Biomes Using Global Eddy Covariance Flux Data. *Remote Sensing*, *9*(5), 418. https://doi.org/10.3390/rs9050418

Xiao, J., Chevallier, F., Gomez, C., Guanter, L., Hicke, J. A., Huete, A. R., Ichii, K., Ni, W., Pang, Y., Rahman, A. F., Sun, G., Yuan, W., Zhang, L., & Zhang, X. (2019). Remote sensing of the terrestrial carbon cycle: A review of advances over 50 years. *Remote Sensing of Environment*, *233*, 111383. https://doi.org/10.1016/j.rse.2019.111383

Xiao, J., & Moody, A. (2004). Photosynthetic activity of US biomes: Responses to the spatial variability and seasonality of precipitation and temperature: Biome responses to gradients in seasonal climate. *Global Change Biology*, *10*(4), 437–451. https://doi.org/10.1111/j.1365-2486.2004.00745.x

Xiao, X. (2004). Modeling gross primary production of temperate deciduous broadleaf forest using satellite images and climate data. *Remote Sensing of Environment*, *91*(2), 256–270. https://doi.org/10.1016/j.rse.2004.03.010

Xu, X., Du, H., Fan, W., Hu, J., Mao, F., & Dong, H. (2019). Long-term trend in vegetation gross primary production, phenology and their relationships inferred from the FLUXNET data. *Journal of Environmental Management*, *246*, 605–616. https://doi.org/10.1016/j.jenvman.2019.06.023

Yang, F., Ichii, K., White, M. A., Hashimoto, H., Michaelis, A. R., Votava, P., Zhu, A.-X., Huete, A., Running, S. W., & Nemani, R. R. (2007). Developing a continental-scale measure of gross primary production by combining MODIS and AmeriFlux data through Support Vector Machine approach. *Remote Sensing of Environment*, *110*(1), 109–122. https://doi.org/10.1016/j.rse.2007.02.016

Yang, H., Yang, X., Zhang, Y., Heskel, M. A., Lu, X., Munger, J. W., Sun, S., & Tang, J. (2017). Chlorophyll fluorescence tracks seasonal variations of photosynthesis from leaf to canopy in a temperate forest. *Global Change Biology*, *23*(7), 2874–2886. https://doi.org/10.1111/gcb.13590

Yang, X., Tang, J., Mustard, J. F., Lee, J.-E., Rossini, M., Joiner, J., Munger, J. W., Kornfeld, A., & Richardson, A. D. (2015). Solar-induced chlorophyll fluorescence that correlates with canopy photosynthesis on diurnal and seasonal scales in a temperate deciduous forest: Fluorescence and photosynthesis. *Geophysical Research Letters*, *42*(8), 2977–2987. https://doi.org/10.1002/2015GL063201

Yuan, W., Liu, S., Zhou, G., Zhou, G., Tieszen, L. L., Baldocchi, D., Bernhofer, C., Gholz, H., Goldstein, A. H., Goulden, M. L., Hollinger, D. Y., Hu, Y., Law, B. E., Stoy, P. C., Vesala, T., & Wofsy, S. C. (2007). Deriving a light use efficiency model from eddy covariance flux data for predicting daily gross primary production across biomes. *Agricultural and Forest Meteorology*, *143*(3–4), 189–207. https://doi.org/10.1016/j.agrformet.2006.12.001

Zhang, Y., Guanter, L., Berry, J. A., Van Der Tol, C., Yang, X., Tang, J., & Zhang, F. (2016). Model-based analysis of the relationship between sun-induced chlorophyll fluorescence and gross primary production for remote sensing applications. *Remote Sensing of Environment*, *187*, 145–155. https://doi.org/10.1016/j.rse.2016.10.016

Zhang, Z., Xu, W., Qin, Q., & Long, Z. (2021). Downscaling Solar-Induced Chlorophyll Fluorescence Based on Convolutional Neural Network Method to Monitor Agricultural Drought. *IEEE Transactions on Geoscience and Remote Sensing*, *59*(2), 1012–1028. https://doi.org/10.1109/TGRS.2020.2999371